Constraints on CP Violating Yukawa Couplings in Standard Model Effective Field Theory

Dissertation
zur Erlangung des akademischen Grades
Dr. rer. nat. im Fach Physik

vorgelegt von

Dimitrios Alexander Skodras

geboren in Aschaffenburg

Lehrstuhl für Theoretische Physik III
Fakultät Physik
Technische Universität Dortmund
2025

1. Gutachter :	Prof. Dr. Joachim Brod
2. Gutachter :	Prof. Dr. Heinrich Päs
Vorsitzender der Prüfungskommission :	Prof. Dr. Heinz Hövel
Mitglied der Prüfungskommission :	Prof. Dr. Julia K. Vogel

Datum des Einreichens der Arbeit :	22. Januar, 2025
Datum der mündlichen Prüfung :	28. Februar, 2025

Kurzfassung

In dieser Dissertation werden die Beschränkungen für CP-verletzende Yukawa-Kopplungen im Rahmen des Standardmodells als effektive Feldtheorie (SMEFT) untersucht. Im Standardmodell der Teilchenphysik (SM) existieren solche Kopplungen nicht, sind aber durch die Baryon-Asymmetrie des Universums (BAU) motiviert. Höherdimensionale Operatoren des SMEFT induzieren Abweichungen von den SM-Yukawa-Wechselwirkungen, deren Beiträge in führender Ordnung zu den fundamentalen elektrischen Dipolmomenten (EDM) der SM-Fermionen und den effektiven Wechselwirkungen mit dem Higgs-Boson wir hier präsentieren durch die Berechnung von Wilson-Koeffizienten (WC). Mit dem Programm `GAMBIT` wird eine umfassende globale Analyse durchgeführt, bei der die Nullergebnisse der EDM-Experimente mit den Daten des Large Hadron Collider (LHC) kombiniert werden, um die CP-verletzenden Phasen der Yukawa-Kopplungen sowohl leichter als auch schwerer Fermionen zu bestimmen. Bis zu sechs WCs werden gleichzeitig gescannt. Für die Berechnung der Kollisionsobservablen verwenden wir `HiggsSignals` und `HiggsBounds`, die mit `GAMBIT` verknüpft sind, während wir für die Berechnung der Log-Likelihoods für die EDMs einen selbst geschriebenen Code verwenden. Aufgrund der unterschiedlichen Abhängigkeiten der Observablen zu den WCs werden nicht-triviale Korrelationen zwischen dem EDM und den LHC-Beschränkungen gefunden.

Abstract

This thesis explores the constraints on CP-violating Yukawa couplings within the framework of Standard Model Effective Field Theory (SMEFT). In the Standard Model of particle physics (SM) such couplings do not exist but are motivated by the baryon asymmetry of the universe (BAU). Higher-dimensional operators of SMEFT induce deviations of the SM Yukawa interactions. We present their leading-order contributions to the fundamental electric dipole moments (EDM) of the SM fermions and the effective interactions with the Higgs boson through the derivation of Wilson coefficients (WC). A comprehensive global analysis is performed with the tool `GAMBIT`, combining EDM experimental limits with data from the Large Hadron Collider (LHC) to extract constraints on the CP-violating phases of both light and heavy fermion Yukawa couplings. Up to six WCs are scanned simultaneously. For the calculation of collider observables, we use `HiggsSignals` and `HiggsBounds` interfaced with `GAMBIT` while we use self-written code for the calculation of log-likelihoods for the EDMs. Due to the differing dependencies of the observables on the WCs non-trivial correlations between the EDM and the LHC constraints are found.

Contents

Chapter 1

Introduction

Most cultures, past and present, have sought to understand the origins of the existence and the fundamental nature of everything around them. In Greek mythology, the word *cosmos* means "harmony" or "order", which reflects structure and balance. The Latin term *universum* conveys the unity and totality of all existence in a single, ordered entity. Similarly, the German term *Weltall* translates to a world, encompassing all existence. In Mandarin (*Yuzhou*) and Japanese (*Uchu*), the same characters represent the vast expanse of space and time. The Sanskrit term *Brahmanda* calls the cosmos an egg, symbolising the creation of the universe from a primordial seed. Each of these terms highlights a different perspective on the structure we humans attempt to derive coherence of natural phenomena and meaning for ourselves. Despite the different cultural approaches to answering questions, humanity has been very successful in unravelling the mysteries of our universe. It is remarkable that a species shaped primarily by survival has evolved the capacity to describe phenomena far removed from our everyday spatial and temporal experiences. To the author, this is the most astonishing aspect of the cosmos: that it is knowable, governed by principles and logic that allow us to predict and comprehend events beyond our immediate perceptions. Not everything is chaotic, even if at times it may seem so in our individual lives.

Over the past few centuries, the field of (particle) physics has evolved into a highly formalised and predictive framework. Central to this progression is the construction of the Standard Model of particle physics (SM), which is built on the foundational principles of quantum mechanics and special relativity. These provided the theoretical groundwork to describe the fundamental particles and develop coherent formulations for their interactions. This effort culminated in the groundbreaking discovery of the Higgs boson [1] with the completion of the particle content of the SM. One example of its predictive powers is the anomalous magnetic moment of the electron, where the theoretical prediction [2] and the experimentally measured value [3] align to around 13 significant digits. However, despite its achievements, the SM remains incomplete. Several significant gaps are left. The observed masses of neutrinos are inconsistent with massless neutrinos in the SM [4, 5]. Gravity, as described by general relativity, is entirely absent from it. In addition, other mysteries present challenges, likely rooted in physics beyond the SM. Dark matter and dark energy, which together account for the majority of the mass-energy content of the universe, are not a part of it [6]. Some challenges are more theoretical, like the unification of the electroweak with the strong interaction in a Grand Unified Theory, as well as with quantum gravity in frameworks like string theory or M-theory.

One phenomenon the SM fails to explain is baryogenesis, the observed asymmetry between matter and antimatter in the universe [7]. The underlying assumption is that the initial state of the universe was highly symmetric, including an equal treatment of matter and antimatter. This CP-symmetry (Charge and Parity symmetry) would imply that they were initially created in equal amounts. But if this symmetry had persisted, structures like galaxies would not have formed due to frequent particle-antiparticle annihilation. To resolve this inconsistency, baryogenesis is invoked, a process that introduces a mechanism to generate the excess of matter of antimatter during the early stages of the universe. Several theoretical frameworks are developed to explain it. Three prominent approaches are leptogenesis, GUT-baryogenesis and electroweak baryogenesis [8, 9]. Leptogenesis relies on the existence of very massive sterile neutrinos, which are predicted by seesaw models [10]. GUT baryogenesis predicts heavy bosonic particles that decay asymmetrically into baryons and leptons and thus introduce the baryon asymmetry [8]. Electroweak baryogenesis (EWBG) assumes that a significant amount of CP-symmetry violation arises from new Yukawa interactions involving the Higgs boson [11, 12]. During the electroweak phase transition, as the universe cooled, bubbles of the asymmetric vacuum connected to the Higgs field formed within the symmetric phase. Near their walls the symmetry-violating effects occur. Sphaleron processes, which violate the conservation of baryon number, converted the CP asymmetry into a net baryon asymmetry. This asymmetry effectively froze after the phase transition was completed and remains until today.

Electroweak baryogenesis implies contributions to certain measurable observables such as the electric dipole moments (EDMs) of fundamental fermions and the production and decay processes of the Higgs boson at colliders. Both the null measurements of EDMs [13] and the collider data, see e.g., [14], put constraints on the parameter space of the CP-violating interactions. One simple and frequently employed framework to probe this parameter space is the so-called κ-framework [14]. In this approach, the SM Yukawa couplings are rescaled by an overall factor and a complex phase, introducing CP-violating interactions. The κ-framework is particularly effective for the exploration of CP-violation associated with the heavier SM fermions. However, when applied to the lighter fermions, such as the electron, some contributions lead to unphysical results. A more consistent approach is the SM Effective Field Theory (SMEFT) [15]. It extends the SM by incorporating higher-dimensional effective operators encoding effects of new physics at higher energy scales. The inclusion of these operators is necessary to create physical results, which, however, are divergent with the high new physics scale. The purpose of these studies is to provide quantified bounds on the CP-violating interactions so that models beyond the SM entailing CP-violating processes can be more easily constrained.

This thesis is organised as follows. In Chapter 2, the theoretical background is established, covering quantum field theoretical concepts, CP-violation, and a review of the components of the SM relevant to this thesis. Regularisation and renormalisation techniques are introduced in the context of quantum chromodynamics (QCD) and the methodology of effective field theories (EFTs) is explored, including matching conditions and the renormalisation group running of effective couplings, *i.e.*, Wilson coefficients (WCs). Chapter 3 focuses on the setup of the two EFTs and the constraining observables. Global analysis as a method for scanning large parameter spaces for multiple observables and inferring predictions is presented. In Chapter 4, the κ-framework is applied to compute WCs of the EDM and chromo-EDM (CEDM) operators for light quarks. A technical description of the methodology for calculating integrals of associated two-loop Feynman diagrams. This chapter is based on our publication [120]. Chapter 5 extends the analysis by performing a global analysis of multiple Yukawa operators at once within SMEFT. This includes explicit calculations of the WCs for the (C)EDMs and the Weinberg operator, alongside their renormalisation group evolution down to the hadronic scale. Constraints on WCs of up to three fermions simultaneously are provided. This chapter is based on our publication [137]. Finally, in Chapter 6, we conclude this thesis.

Chapter 2

Theoretical Background

2.1 Scattering and Quantum Field Theory

As theoretical models attempt to explain physical phenomena, we begin our discussion by introducing the mathematical framework that describes the physically measurable effects. More details can be found in [16–20].

Scattering Theory

The measurable quantities relevant for this thesis are probabilities for the transition of one quantum mechanical state to another. These states represent vectors in a Hilbert space. To compute the probabilities, we define the S-matrix as the transition amplitude from the initial 'in' state Ψ_α^+ into the final 'out' state Ψ_β^- as

$$S_{\beta\alpha} = \left\langle \Psi_\beta^- \middle| \Psi_\alpha^+ \right\rangle \tag{2.1}$$

with α, β a collection of labels like four-momentum, spin z-component, etc. The operation $\langle \cdot | \cdot \rangle$ denotes the inner product of the Hilbert space. Taking the absolute square of the S-matrix is then a measure of the likelihood for the transition to occur. We introduce the time-dependent Hamilton operator $H(t)$ being split into a free part H_0 and an interaction part H_{int}. The former describes the non-interacting propagation of free eigenstates Φ_α with an energy E_α while the full operator has eigenstates $\Psi_\alpha^\pm$ with the same eigenvalue. These eigenstates can be expressed by the free states through the Lippmann-Schwinger equations. Another definition of the S-matrix with the free fields reads as $S_{\beta\alpha} = \left\langle \Phi_\beta \middle| S \middle| \Phi_\alpha \right\rangle$ with the unitary S-operator transferring a state over time and can be expressed by a time evolution operator

$$U(t_1, t_2) = \mathcal{T} \exp \left(-\mathrm{i} \int_{t_1}^{t_2} \mathrm{d}t H_{\text{int}}(t) \right) \tag{2.2}$$

as $S = U(-\infty, +\infty)$. $\mathcal{T}$ orders the operators by their actions with time. We use natural units where the reduced Planck constant and the speed of light are $\hbar = c = 1$. To obtain the probability for the transition $P(\alpha \to \beta)$ we consider a finite macroscopic volume V and a finite time T in which the whole system resides. Further, we define the final-state interval $\mathrm{d}\beta$ so that the total number of states therein is $\mathrm{d}\mathcal{N}_\beta \sim V^{N_\beta}\,\mathrm{d}\beta$. The conservation of momentum and energy in the S-matrix is ensured by two δ-distributions, which, when squared, deliver a factor of the volume and the interaction time. We find for large V and T

$$\mathrm{d}P(\alpha \to \beta) \sim V^{1-N_\alpha} T |M_{\beta\alpha}|^2 \delta^4(p_\beta - p_\alpha)\,\mathrm{d}\beta, \tag{2.3}$$

with $M_{\beta\alpha}$ as the non-trivial part of the S-matrix, *i.e.*, $S_{\alpha\beta} = \delta(\beta - \alpha) - 2\pi\mathrm{i}\delta^4(p_\beta - p_\alpha)M_{\beta\alpha}$. The differential transition rate is the probability of transition during the interaction time T as

$$\mathrm{d}\Gamma(\alpha \to \beta) \sim V^{1-N_\alpha}\, |M_{\beta\alpha}|^2\, \delta^4(p_\beta - p_\alpha)\,\mathrm{d}\beta. \tag{2.4}$$

On the left-hand side is a measurable quantity, and on the right-hand side is the matrix element $M_{\beta\alpha}$ which we compute with quantum field theory (QFT) describing the interactions among particles.

Quantum Field Representations

To enforce the invariance of the S-operator under transformations Λ of the proper Lorentz group $SO^+(1,3)$ we make the ansatz that the Hamilton operator in Eq. (2.2) is a spatial integral over a Hamilton density $\mathcal{H}(\mathbf{x}, t)$ which itself transforms as a scalar under Lorentz transformations. The elements of the Lie algebra to the Lorentz group can be expressed by a basis change through elements of the direct sum of two Lie algebras of $SU(2)$, *i.e.*, $\mathfrak{so}(1,3) \cong \mathfrak{su}(2) \oplus \mathfrak{su}(2)$. With the representations of $\mathfrak{su}(2)$ (labelled by $j = 0, 1/2, 1, \ldots$ and dimension $2j+1$) we can denote representations of the Lorentz algebra as $D(\Lambda) = (j_1, j_2)$ and dimension $(2j_1+1)(2j_2+1)$. More on group and representation theory, see Sec. 2.2. Particles with integer spin are called bosons; ones with half-integer spin are fermions. The time ordering also is Lorentz invariant if the evaluations of $\mathcal{H}(x)$ and $\mathcal{H}(x')$ at spacetime points x and x' commute, *i.e.*, they cannot causally interfere with each other. To have such a Lorentz invariant $\mathcal{H}$ also fulfilling the causality condition, we build it out of the field operators. Examples relevant for us are [21]

$$\phi(x) = \int \frac{\mathrm{d}^3p}{(2\pi)^{3/2}} \frac{1}{(2E)^{1/2}} \left(a(\mathbf{p})\mathrm{e}^{-\mathrm{i}px} + a^{c\dagger}(\mathbf{p})\mathrm{e}^{\mathrm{i}px} \right), \tag{2.5}$$

$$\psi_l(x) = \sum_\sigma \int \frac{\mathrm{d}^3p}{(2\pi)^{3/2}} \frac{1}{(2E)^{1/2}} \left(u_l(\mathbf{p},\sigma)a(\mathbf{p},\sigma)\mathrm{e}^{-\mathrm{i}px} + v_l(\mathbf{p},\sigma)a^{c\dagger}(\mathbf{p},\sigma)\mathrm{e}^{\mathrm{i}px} \right), \tag{2.6}$$

$$A^\mu(x) = \sum_\sigma \int \frac{\mathrm{d}^3p}{(2\pi)^{3/2}} \frac{1}{(2E)^{1/2}} \left(\epsilon^\mu(\mathbf{p},\sigma)a(\mathbf{p},\sigma)\mathrm{e}^{-\mathrm{i}px} + \epsilon^{\mu*}(\mathbf{p},\sigma)a^{c\dagger}(\mathbf{p},\sigma)\mathrm{e}^{\mathrm{i}px} \right) \tag{2.7}$$

The field $\phi(x)$ transforms as the scalar representation of the Lorentz group $D(\Lambda) = (0,0)$, the operator $a(\mathbf{p})$ is an annihilation operator that annihilates a particle with momentum $\mathbf{p} = \sqrt{E^2 - m^2}$ upon acting on a state, while $a^{c\dagger}(\mathbf{p})$ creates one with opposite quantum numbers († represents the Hermitian conjugation). The massive field $A^\mu(x)$ transforms as a Lorentz vector $D(\Lambda) = (1/2, 1/2)$ where the Greek indices $\mu = 0,1,2,3$ label the four spacetime dimensions. The label σ denotes the spin z-component, which runs in integer steps from $-j$ to j (the spin quantum number) and three polarisation vectors e^μ (* denotes complex conjugation). The massless version differs in that the longitudinal polarisation vector $\epsilon^\mu(\mathbf{p}, 0)$ is absent as it would diverge, and it only transforms as a Lorentz vector up to a gauge transformation [22]. It rather transforms as a 2-tensor that is represented by a direct sum $D(\Lambda) = (1,0) \oplus (0,1)$ and expressed as $F^{\mu\nu} = \partial^\mu A^\nu - \partial^\nu A^\mu$ with the partial derivative $\partial^\mu = \partial/\partial x_\mu$. In cases where the group governing the gauge transformation is non-abelian, the 2-tensor obtains an additional term, an example of which is presented in section 2.2. Lastly, $\psi_l(x)$ transforms as a massive spin-$1/2$ particle as a direct sum of two Weyl-spinor representations. $D(\Lambda) = (1/2, 0) \oplus (0, 1/2)$, the 4-dimensional Dirac spinor representation. This is further examined by an infinitesimal Lorentz transformation $\Lambda^\mu{}_\nu = \delta^\mu{}_\nu + \omega^\mu{}_\nu$ with the symmetric Kronecker delta $\delta^\mu{}_\nu$ and $\omega^\mu{}_\nu$ a real, antisymmetric parameter. Its representation is $D(\Lambda) = 1 + \mathrm{i}\omega_{\mu\nu}\sigma^{\mu\nu}$ where the summation over repeated indices is used [1]. The object $\sigma^{\mu\nu}$ is defined by the elements of the Clifford algebra $CL_{1,3}(\mathbb{C})$. Their irreducible representations are 4×4 matrices γ, fulfilling the anticommutation relation

$$\{\gamma^\mu, \gamma^\nu\} = \gamma^\mu\gamma^\nu + \gamma^\nu\gamma^\mu = 2\eta^{\mu\nu}, \tag{2.8}$$

with the Minkowski metric represented in our convention as $\eta = \mathrm{diag}(1, -1, -1, -1)$. This can also be derived by using the Weyl-spinor representations, where the generators of the Lorentz group, rotations and boosts, are expressed by the two-dimensional representations of the $SU(2)$ generators, the Pauli matrices. Apart from the Lorentz vector, the other elements of the Clifford algebra are the trivial Lorentz scalar 1, the pseudoscalar $\gamma_5 = \frac{\mathrm{i}}{4!}\epsilon^{\mu\nu\rho\sigma}\gamma_\mu\gamma_\nu\gamma_\rho\gamma_\sigma$ with the totally antisymmetric tensor ϵ, in our convention $\epsilon_{0123} = -\epsilon^{0123} = 1$, as well as the axial vector $\gamma^\mu\gamma_5$ and the aforementioned tensor $\sigma^{\mu\nu} = \frac{\mathrm{i}}{2}[\gamma^\mu, \gamma^\nu] = \frac{\mathrm{i}}{2}(\gamma^\mu\gamma^\nu - \gamma^\nu\gamma^\mu)$. Lastly, u and v are spinors being elements of the $Spin(1,3)$ representations with a spinor-index l. The plane wave expressions given above are solutions to the following equations of motion in the non-interacting theory [22],

$$(\partial^\mu\partial_\mu - m^2)\phi(x) = 0, \tag{2.9}$$

[1] That is only if the respective index appears exactly twice. Phoenician indices are not summed over.

$$(\mathrm{i}\partial\!\!\!/ - m)\psi(x) = 0, \tag{2.10}$$

$$(\partial_\rho \partial^\rho \eta_{\mu\nu} - \partial_\mu \partial_\nu + m^2 \eta_{\mu\nu}) A^\mu(x) = 0, \tag{2.11}$$

with $\partial\!\!\!/ := \gamma^\mu \partial_\mu$.

Path Integral

We mentioned that the Hamiltonian is built out of field operators where the operator structure resides in their creation and annihilation operators. The initial and final states for our process are the respective amount of these operators acting on the particle-free ground state $|\Omega\rangle$ at asymptotic times t, thus

$$\begin{aligned} &\langle p_1, ..., p_n | S | p'_1, ..., p'_m \rangle \sim \\ &\qquad \lim_{t \to +\infty} \langle \Omega | \mathcal{T} a(\mathbf{p}_n, t) \dots a(\mathbf{p}_1, t) a^\dagger(\mathbf{p}'_1, -t) \dots a^\dagger(\mathbf{p}'_m, -t) | \Omega \rangle. \end{aligned} \tag{2.12}$$

Using the fact that annihilation operators acting on the ground state yield zero and the algebraic relation

$$\mathrm{i} \int \mathrm{d}^4 x_k \, \mathrm{e}^{\mathrm{i} p_k x_k} \mathcal{K}_k \phi(x_k) \sim a(\mathbf{p}_k, \infty) - a(\mathbf{p}_k, -\infty), \tag{2.13}$$

with the Klein-Gordon operator $\mathcal{K}_k = (\partial/\partial x_k^\mu)^2 + m^2$ gives us the reduction formula by Lehmann-Symanzik-Zimmermann (LSZ) [23]

$$\begin{aligned} &\langle p_1, ..., p_k | S | p'_1, ..., p'_n \rangle = \\ &\qquad \prod_{i=1}^{k} \prod_{j=1}^{n} \left[\mathrm{i} \int \mathrm{d}^4 x_i \mathrm{e}^{-\mathrm{i} p'_i x'_i} \mathcal{K}_i \right] \left[\mathrm{i} \int \mathrm{d}^4 x_j \mathrm{e}^{\mathrm{i} p_j x_j} \mathcal{K}_j \right] \\ &\qquad \times \langle \Omega | \mathcal{T} \phi(x_1) \dots \phi(x'_n) | \Omega \rangle. \end{aligned} \tag{2.14}$$

We define the Green functions in coordinate and momentum space as

$$G(x_1, ..., x'_n) = \langle \Omega | \mathcal{T} \phi(x_1) \dots \phi(x'_n) | \Omega \rangle, \tag{2.15}$$

$$\tilde{G}(p_1, ..., p'_n) = \int \mathrm{d}^4 x_1 \dots \mathrm{d}^4 x'_n G(x_1, ..., x'_n) \mathrm{e}^{\mathrm{i}(p_j x_j - p'_i x'_i)}. \tag{2.16}$$

The LSZ formula holds for any local field $\phi(x)$ also with non-vanishing spin. However, for massless particles, it does not [22]. In the massless case, it takes infinitesimally small energies to create any number of particles, which then gives a probability of zero to find a state with a specific amount of them.

Now, we want to calculate Green functions. One approach is the functional path integral framework in which all possible paths with the initial and final states as boundary conditions are summed up and weighted with the action $\mathcal{S}$ [24]. The path gets divided into small time steps where the transitions are operated by the time evolution operator (2.2) and the momenta get integrated over. For theories which are at most quadratic in the momenta and the interacting part thereof not at all, the Hamiltonian can then be related to the Lagrangian L by a Legendre transformation. Taking the continuous limit gives us the path integral [25]

$$G(x_1, ..., x_n') = \frac{\int \mathcal{D}\phi(x)\ \phi(x_1)...\phi(x_n')\mathrm{e}^{\mathrm{i}\mathcal{S}[\phi,\partial_\mu\phi]}}{\int \mathcal{D}\phi(x)\mathrm{e}^{\mathrm{i}\mathcal{S}[\phi,\partial_\mu\phi]}}. \tag{2.17}$$

Here, $\mathcal{S}[\phi, \partial_\mu\phi] = \int\ \mathrm{d}t L[\phi, \partial_\mu\phi] = \int\ \mathrm{d}^4x\mathcal{L}[\phi, \partial_\mu\phi]$ with $\mathcal{L}$ the Lagrangian density. The denominator is a normalisation factor, so that $\langle\Omega|\Omega\rangle = 1$. Contributions from any unattached paths, *i.e.*, vacuum bubbles, cancel in this fraction [22]. One again splits up the Lagrangian in a free part $\mathcal{L}_0$ which is directly solvable in the path integral and an interacting part $\mathcal{L}_1$ for which that is not the case. We assume that the interaction is a small perturbation of the free theory with some coupling constant g small enough to yield an asymptotic series and therefore expand in

$$\mathrm{e}^{\mathrm{i}\mathcal{S}[\phi,\partial_\mu\phi]} = \sum_{k=0}^{\infty} \frac{\mathrm{i}^k}{k!} \left(\int\ \mathrm{d}^4x\mathcal{L}_1[g, \phi]\right)^k \mathrm{e}^{\mathrm{i}\int\ \mathrm{d}^4x\mathcal{L}_0[\phi,\partial_\mu\phi]}. \tag{2.18}$$

An equivalent description for the path integral is the use of the generating functional $Z[J]$ with some auxiliary source function J creating excitations of the field that corresponds to sources and sinks of particles,

$$\begin{aligned} Z[J] &= \int \mathcal{D}\phi \exp\left(\mathrm{i}\int\ \mathrm{d}^4x\mathcal{L}_1 + \mathcal{L}_0 + J(x)\phi(x)\right) \\ &= \int \mathcal{D}\phi \exp\left(\mathrm{i}\int\ \mathrm{d}^4x\mathcal{L}_1 - \frac{1}{2}\phi(x)\mathcal{K}\phi(x) + J(x)\phi(x)\right) \end{aligned} \tag{2.19}$$

$$= \mathrm{e}^{\mathrm{i}\int\ \mathrm{d}^4x\mathcal{L}_1(\delta/\mathrm{i}\delta J(x))}\mathrm{e}^{\frac{\mathrm{i}}{2}\int\ \mathrm{d}y\ \mathrm{d}zJ(y)\mathcal{K}^{-1}(z-y)J(z)}. \tag{2.20}$$

The functional derivative with respect to J, $(\delta/\delta J)$, reproduces Eq. (2.17) as

$$G(x_1, ..., x_n') = (-\mathrm{i})^n \frac{1}{Z[0]}\ \frac{\delta^n Z[J]}{\delta J(x_1)...\delta J(x_n)}\bigg|_{J=0}. \tag{2.21}$$

After expanding $Z[J]$ in couplings g and in the source functions, we can organise the remaining terms in Feynman diagrams up to a desired order in g and neglect higher order contributions if the Taylor series is asymptotic. The object $\mathcal{K}^{-1}(z-y)$ is the propagator for a field from z to y.

For Lorentz scalars, it reads

$$G(x,y) = \mathcal{K}^{-1}(x-y) = \int \frac{\mathrm{d}^4 p}{(2\pi)^4} \frac{\mathrm{e}^{-\mathrm{i}p(x-y)}}{p^2 - m^2 + \mathrm{i}\epsilon} \tag{2.22}$$

with an infinitesimal ϵ which emerges from the time ordering in the two-point Green function. For massless vector fields, $\mathcal{K}$ has no inverse. This is a reflection of the redundant degrees of freedom which have to be gauged and will be further examined when gauge symmetries are discussed in section 2.2.

2.2 Standard Model and CP violation

The Standard Model of elementary particle physics is a combination of a multitude of quantum fields that have a set of transformation rules resulting from the invariance of the Lagrangian with respect to several symmetry groups. Invariance means that two equivalent observers find the same probabilities for an outcome of an experiment. We begin with itemising the here relevant symmetries, the discrete spacetime symmetries and the gauge symmetries associated with Quantum Chromodynamics (QCD) and electroweak (EW) theory. See [17, 26] for details.

Discrete Spacetime Symmetries

A Group G is a set of elements with group operations $(\cdot)$ that assigns one element to any ordered pair of elements. If the set contains a finite amount of elements, G is finite; otherwise it is infinite [27–29]. Its elements are mapped by a representation D onto a set of linear operators in the respective space they act on, such as a Hilbert space. An infinite group is discrete if there is a neighborhood for each element which only contains that element. It is called topological if the group operations are continuous in that there are neighbourhoods of two group elements $g, h \in G$ which are subsets of any neighbourhood of the element $g \cdot h$. Consider an element $g \in G$ that is represented by an operator U on a Hilbert space. If U leaves the inner product of two quantum mechanical states unchanged, we call it a symmetry transformation, and if this holds for all elements in G, we call it a symmetry group. The operator U is then either unitary and linear or antiunitary and antilinear.

Now, we cover instances of discrete symmetry transformations. The full (inhomogeneous) Lorentz group $O(1,3)$ contains two elements that cannot be continuously reached from the identity element, as they have a negative determinant. These are called parity P and time-reversal T. Parity flips the sign of the spatial coordinates of the vector it acts on, whereas time-reversal flips the sign of the time coordinate. Their respective representations in Minkowski space may take the form $D(P) =: \mathcal{P} = \mathrm{diag}(1, -1, -1, -1)$ and $D(T) =: \mathcal{T} = -\mathcal{P}$. We obtain the following parity transformations for the different quantum fields [1]

$$P\phi(x)P^\dagger = \eta_P\phi(\mathcal{P}x) \qquad T\phi(x)T^\dagger = \eta_T\phi(-\mathcal{P}x) \tag{2.23}$$
$$PA^\mu(x)P^\dagger = -\zeta_P\mathcal{P}^\mu{}_\nu A^\nu(\mathcal{P}x) \qquad TA^\mu(x)T^\dagger = \zeta_T\mathcal{P}^\mu{}_\nu A^\nu(-\mathcal{P}x) \tag{2.24}$$
$$P\psi(x)P^\dagger = \xi_P\gamma^0\psi(\mathcal{P}x) \qquad T\psi(x)T^\dagger = \xi_T\gamma_1\gamma_3\psi(-\mathcal{P}x) \tag{2.25}$$

with phase factors $\eta_{P,T}$, $\zeta_{P,T}$, $\xi_{P,T}$ [21]. The negative sign in the parity relation for the vector field results from $\mathcal{P}^\mu{}_\nu\epsilon^\mu(0,\sigma) = -\epsilon^\nu(0,\sigma)$. The respective combinations of γ matrices in the fermionic field follow from the requirement that the creation (annihilation) operators transform as $Pa^{(c^\dagger)}(\mathbf{p},\sigma)P^\dagger = \xi_P a^{(c^\dagger)}(-\mathbf{p},\sigma)$ and $Ta^{(c^\dagger)}(\mathbf{p},\sigma)T^\dagger = \xi_T(-1)^{1/2-\sigma}a^{(c^\dagger)}(-\mathbf{p},-\sigma)$.

Another discrete symmetry transformation is charge conjugation C, associated with the exchange of particles and antiparticles. It leaves space-time quantities invariant and only flips the signs of discrete quantum numbers such as the electric charge Q. Its transformation properties w.r.t. the particle fields are

$$C\phi(x)C^\dagger = \eta_C\phi^\dagger(x), \tag{2.26}$$
$$CA^\mu(x)C^\dagger = \zeta_C A^{\mu\dagger}(x), \tag{2.27}$$
$$C\psi(x)C^\dagger = -\mathrm{i}\xi_C\left(\overline{\psi}(x)\gamma^0\gamma^2\right)^T, \tag{2.28}$$

with phase factors η_C, ζ_C, ξ_C and $\overline{\psi} = \psi^T\gamma_0$.

In contrast to parity transformation and charge conjugation, time reversal is an antiunitary operation, which implies $T\mathrm{i}H = -\mathrm{i}HT$. Thinking of this transition as inverting the rotation of a system, the odd nature of the angular momentum operator becomes apparent $T^\dagger\mathbf{J}T = -\mathbf{J}$. Acting on a one-particle state $\Psi_{p,\sigma}$ with rotational symmetry, we have $T\Psi_{p,\sigma} = \zeta_T(\sigma)\Psi_{\mathcal{P}p,-\sigma}$. We apply T to the equation for the raising and lowering angular momentum operator ($J_\pm = J_1 \pm \mathrm{i}J_2$)[16]

$$TJ_\pm\Psi_{p,\sigma} = T\sqrt{(j\mp\sigma)(j\pm\sigma+1)}\Psi_{p,\sigma\pm1} \tag{2.29}$$
$$-J_\mp\zeta_T(\sigma)\Psi_{\mathcal{P}p,-\sigma} = \sqrt{(j\mp\sigma)(j\pm\sigma+1)}\zeta_T(\sigma\pm1)\Psi_{\mathcal{P}p,-\sigma\mp1} \tag{2.30}$$
$$-\zeta_T(\sigma) = \zeta(\sigma\pm1) \tag{2.31}$$

to which one solution is

$$T\Psi_{p,\sigma} = \zeta_T(\sigma)\Psi_{\mathcal{P}p,-\sigma} = (-1)^{j+\sigma}\Psi_{\mathcal{P}p,-\sigma}. \tag{2.32}$$

[1] In some textbooks [30] these transformations are performed by mapping a contravariant spacetime vector onto a covariant one. Only the metric can do that, even though the respective representations of P and T are proportional to the Minkowski metric.

The inclusion of the total angular momentum quantum number j ensures that the phase factor ζ_T does not become imaginary when fermions are considered [16]. In general, a phase ζ only depending on the particle species could be included, but as the one-particle states $\Psi_{p,\sigma}$ can be redefined by a change of phase, this ζ bears no physical relevance. While T is antilinear and therefore not an observable, T^2 is observable and acts as

$$T^2\Psi_{p,\sigma} = T(-1)^{j+\sigma}\Psi_{\mathcal{P}p,-\sigma} = (-1)^{j+\sigma}(-1)^{j-\sigma}\Psi_{p,\sigma} = (-1)^{2j}\Psi_{p,\sigma} \tag{2.33}$$

yielding for both massive and massless non-interacting particles an eigenvalue of $+1$ for bosons and -1 for (an odd number of) fermions. There is an implication in the fermionic case when we consider a time-reversal-symmetric Hamiltonian H with an eigenstate ψ_1 with energy E. Another state $T\psi_1 = \psi_2$ would also be an eigenstate since $H\psi_2 = HT\psi_1 = TH\psi_1 = TE\psi_1 = E\psi_2$ [21]. Supposing that these two states are the same, *i.e.*, $T\psi_1 = \zeta\psi_1 = \psi_2$ (complex ζ with $|\zeta|^2 = 1$) we find $T^2\psi_1 = T\zeta\psi_1 = \zeta^* T\psi_1 = |\zeta|^2\psi_1 = +\psi_1$ in contradiction with the premise that $T^2\psi_1 = -\psi_1$. So, ψ_1 builds a two-fold degenerated energy eigenstate with ψ_2 (Kramers degeneracy [31]) while being orthogonal to each other

$$\langle\psi_2|\psi_1\rangle = \langle T\psi_1|T\psi_2\rangle = \langle\psi_2|T^2\psi_1\rangle = -\langle\psi_2|\psi_1\rangle. \tag{2.34}$$

The first equality stems from the antiunitarity of T. In a rotationally invariant environment, this degeneracy is straightforward, as a total angular momentum j that is half-integer results in $2j+1$ degenerate states. The remarkable implication is that this degeneracy persists even when the rotational invariance is broken by external influences, such as electrostatic fields, provided these fields respect time-reversal symmetry [16, 29, 30]. Importantly, if a particle possessed an electric dipole moment, this degeneracy among its spin states would be entirely lifted in a static electric field. Such dipole moments are therefore prohibited by the requirement of T-invariance. Conversely, the detection of such dipole moments would signal T-violation and hence CP-violation.

We can further build combinations of the aforementioned operations. Most notable is the combination of C and P, say CP, as it is one key ingredient to a successful baryogenesis discussed in section 3.2.3. As mentioned in the title of this thesis, violation of a combination of charge conjugation and parity transformations (CP) on Yukawa interactions will be of interest. Such an interaction

$$\mathcal{H}_{\text{int}} = \overline{\psi}_1(a + b\gamma_5)\psi_2\phi_3 + \text{h.c.} \qquad a, b \in \mathbb{C} \tag{2.35}$$

transforms under CP as

$$(CP)\mathcal{H}_{\text{int}}(CP)^{\dagger} = \kappa_{CP}\overline{\psi}_2(a - b\gamma_5)\psi_1\phi_3^{\dagger} + \text{h.c.} \tag{2.36}$$

with κ_{CP} a product of complex phases. This interaction term can only be invariant under CP if either a and b are both purely real, imaginary, or arbitrary but identical, or one of them vanishes. In these cases, a κ_{CP} can be chosen appropriately. Incidentally, C is conserved if either $a \in \mathbb{R}$ and $b \in \mathbb{I}$ or vice versa, or one is zero. Parity is only conserved if either a or b is not present. If neither is the case, this interaction violates the CP-symmetry. In Sec. 4.1 the interaction we consider is identified with $a \in \mathbb{R}$, $b \in \mathbb{I}$ and thus violates CP and P but respects C-symmetry.

Gauge Symmetries

Topological groups have continuous operations. If these operations are also smooth in that they are infinitely many times differentiable w.r.t. a finite set of real parameters $\alpha = \{\alpha_k\}$, we call the group a Lie group. The identity element is $e = g(\alpha)\big|_{\alpha=0}$ from which we can go infinitesimal steps $\mathrm{d}\alpha$ to reach group elements in its neighbourhood represented by a Taylor expansion [17, 26]

$$D(d\alpha) = 1 + \mathrm{i}\ \mathrm{d}\alpha_a T_a + \cdots \tag{2.37}$$

with the Ts being called generators of the group and the assumption that they are independent hermitian operators to form unitary representations. Due to the smoothness of the group operations, the expansion as in Eq. (2.37) can be exercised as a combination of many generators yielding the central commutator algebra they form, namely

$$[T_a, T_b] = \mathrm{i} f_{abc} T_c. \tag{2.38}$$

This operation is called a Lie bracket, which, together with a vector space V, is named a Lie algebra $\mathfrak{g}$. [1] It can be conceived as the tangent space to the identity element on the manifold of the corresponding Lie group G. Central to the Lie algebra are the structure constants f_{abc} which are real in case the group has at least one unitary group representation but otherwise independent of representations [26, 27]. If they are all zero, the Lie group is abelian, *i.e.*, all Lie algebra elements commute with each other. Our discussion will revolve mostly around the special unitary group $SU(N)$, the group of unitary $N \times N$ (N a positive integer) dimensional matrices with determinant $\det U = 1$. Its Lie algebra $\mathfrak{su}(N)$ contains $N^2 - 1$ elements for

[1] common representations of the bases for $N \in \{2, 3\}$ are the Pauli- and Gell-Mann matrices t_a. Our representation is related by $T_a = 1/2 t_a$.

which

$$T_a T_b = \frac{1}{2N}\delta_{ab} I_N + \frac{1}{2}(\mathrm{i} f_{abc} + d_{abc}) T_c \tag{2.39}$$

and constants d_{abc} symmetric in all indices. Both are calculated by

$$d_{abc} = 2\mathrm{Tr}\left(\{T_a, T_b\} T_c\right), \tag{2.40}$$

$$f_{abc} = 2\mathrm{i}\mathrm{Tr}\left([T_a, T_b] T_c\right). \tag{2.41}$$

with the normalisation of the generators in the fundamental representation

$$\mathrm{Tr}(T_a T_b) = \frac{1}{2}\delta_{ab}. \tag{2.42}$$

Consider the product $C_2 := T_a T_a$, called the quadratic Casimir operator that commutes with all $\mathfrak{su}(N)$-elements

$$[T_a T_a, T_b] = T_a [T_a, T_b] + [T_a, T_b] T_a = \mathrm{i} f_{abc}(T_a T_c + T_c T_a) = 0 \tag{2.43}$$

and by Schur's lemma [32] it must be proportional to the identity element with a scalar C_F

$$C_F I_N = T_a T_a. \tag{2.44}$$

Tracing both sides and using Eq. (2.42) with $\delta_{aa} = N^2 - 1$ yields

$$C_F = \frac{N^2 - 1}{2N}, \tag{2.45}$$

again for the fundamental representation. Having established the concept of gauge symmetries and Lie groups, we can now move on to the covariant derivative, an essential tool in gauge theory. The covariant derivative allows us to extend the notion of differentiation to spaces with gauge symmetries, ensuring that the derivative of a field transforms covariantly under local gauge transformations. In gauge theories, the fields and their derivatives must transform consistently under local gauge transformations. Let's consider a field $\psi(x)\psi(x)$ that transforms under a local gauge transformation $U(x) \in G$, as

$$\psi(x) \to \psi(x) = U(x)\psi(x). \tag{2.46}$$

A standard derivative $\partial_\mu \psi(x)$ does not transform covariantly under this transformation. Instead, we introduce the covariant derivative gauge transformation of the field. The covariant derivative is defined as

$$D_\mu\psi(x) = (\partial_\mu + \mathrm{i}A^a_\mu(x)T^a)\psi(x), \tag{2.47}$$

where $A_\mu(x)$ is the gauge field, which itself transforms under the gauge group as [21]

$$A_\mu(x) \to A'_\mu(x) = U(x)A_\mu(x)U^\dagger(x) - \mathrm{i}(\partial_\mu U(x))U^\dagger(x). \tag{2.48}$$

In order to see the effect of the covariant derivative, let's apply it to a field $\psi(x)$. First, consider the transformation of the field under a small gauge transformation parameterised by $\alpha(x)$

$$U(x) = \exp\left(\mathrm{i}\alpha^a(x)T^a\right). \tag{2.49}$$

When we consider a field ϕ which transforms non-trivially under $SU(N)$, *i.e.*,

$$\phi(x) \to \mathrm{e}^{\mathrm{i}\alpha_a(x)T_a}\phi(x) =: U(x)\phi(x), \tag{2.50}$$

the comparison of its values at two spacetime points x and y is not invariant under this transformation as arbitrary phases $\alpha_a(x)$ can be set [26]. However, a connection can be made by introducing a field $W(x,y)$ which transforms as [16]

$$W(x,y) \to U(x)W(x,y)U^\dagger(y) \tag{2.51}$$

with which $W(x,y)\phi(y) - \phi(x)$ is now independent of the phases. Expanding $W(x,y)$ with $y = x + \delta x$ around $\delta x = 0$,

$$W(x, x+\delta x) = I_N - \mathrm{i}gA^\mu_a(x)T_a\delta x_\mu + \mathcal{O}(\delta x^2), \tag{2.52}$$

where the gauge fields are $A^\mu_a(x)$ and $g \in \mathbb{R}$. As the comparison term is independent of the phases we can determine the covariant derivative to be

$$D^\mu\phi(x) = \lim_{\delta x_\mu \to 0} \frac{W(x,x+\delta x)\phi(x+\delta x) - \phi(x)}{\delta x_\mu} = \partial^\mu - \mathrm{i}gA^\mu_a T_a. \tag{2.53}$$

With $D^\mu\phi(x) \to U(x)D^\mu\phi(x)$ we can derive the transformation of the gauge fields as

$$A^\mu_a(x) \to A^\mu_a(x) + \frac{1}{g}\partial_\mu\alpha_a(x) - f_{abc}\alpha_b(x)A^\mu_c + \mathcal{O}(\alpha^2). \tag{2.54}$$

The corresponding 2-tensor,

$$F_{\mu\nu} := \frac{\mathrm{i}}{g}[D_\mu, D_\nu], \tag{2.55}$$

contains an interaction term among the gauge fields in non-abelian gauge theories and, hence, by itself, is not gauge invariant. Calculating the propagator of the massless gauge field A^μ the redundant degrees of freedom have to be gauged, which is done by employing the De Witt-Faddeev-Popov procedure [33]. The measure of the path integral over a gauge field gets multiplied by $1 = \int Dg(x)\delta(f(A_g))\Delta(A_g)$, where $f(A_g) = \partial_\mu A_g^\mu - \sigma_g$ with an arbitrary function σ and $\Delta(A_g) = \det(\delta/\delta g f(A_g))$ is the Fadeev-Popov determinant. Further, A_g is the four-vector transformed with some gauge function $g(x)$ which leaves the action invariant. The insertion of the multiplicative factor then yields a functional integral over the gauge field restricted to physically inequivalent field configurations and a divergent integral over $g(x)$ that cancels out in the Green function. As this procedure does not depend on σ, we integrate over it with a Gaussian weight $\exp\left(-\mathrm{i}\int \mathrm{d}^4x\sigma^2/(2\xi)\right)$ with ξ being a constant gauge parameter. Together with $\delta(f(A_g))$ this yields the gauge fixing term in the Lagrangian

$$\mathcal{L}_{\text{gf}} = -\left(\partial_\mu A^\mu\right)^2/(2\xi) \tag{2.56}$$

Physical results are independent of this parameter. If the gauge transformation results from a non-abelian symmetry group, the Fadeev-Popov determinant is not independent of the gauge field. The determinant is represented as a functional integral over a set of anticommuting fields $c, \bar{c}$ transforming as Lorentz scalars. They are called Faddeev-Popov (anti-)ghosts as their Green's function always vanishes. When adding the gauge fixing term $\mathcal{L}_{\text{gf}}$ to the theory, gauge invariance is explicitly broken. For this choice of gauge fixing, the inclusion of

$$\mathcal{L}_{\text{ghost}} = \bar{c}_a\partial^\mu D_\mu c_a, \tag{2.57}$$

the invariance is restored. For general gauge fixing terms, the Lagrangian still exhibits invariance under BRST transformations being preserved at loop-order. Invariance under this transformation, parameterised by an infinitesimal Grassmann constant that commutes with the (anti-)ghost fields, means the theory remains renormalisable.

Quantum Chromodynamics

The gauge symmetry group of the SM in the unbroken phase is

$$\mathcal{G}_{\text{SM}} = SU(3)_C \times SU(2)_L \times U(1)_Y, \tag{2.58}$$

with $SU(3)_C$ describing Quantum Chromodynamics (QCD) and $SU(2)_L \times U(1)_Y$ describing the electroweak (EW) interaction [17]. The $SU(3)_C$ (C stands for colour) gauge symmetry describes the strong interaction. The corresponding Lie algebra contains 8 elements representing the gauge fields G_μ^a, the gluons [26]. While they transform as octets in the fundamental representation, the quarks q of some flavour f transform as triplets [21]. The covariant derivative (Eq. (2.53)) contains the QCD coupling constant g_s. As $SU(3)_C$ is a non-abelian group, the 2-tensor (Eq. (2.55)) $G_{\mu\nu}$ implies a self-interaction term for gluon fields, and, as discussed in the previous paragraph, a gauge-fixing term and ghost terms are also present in the fundamental QCD Lagrangian, written as [22]

$$\mathcal{L}_{\text{QCD}} = -\frac{1}{4}G^a_{\mu\nu}G^{a,\mu\nu} - \frac{1}{2\xi_G}\left(\partial^\mu G^a_\mu\right)^2 + \overline{q}_f \mathrm{i}\not{D} q_f + \chi^{a*}\partial^\mu D^{ab}_\mu \chi^b. \tag{2.59}$$

One term that upholds the gauge symmetry but is not present in the Lagrangian is the θ-term which captures the possibility of CP violation in the strong interaction [34]

$$\mathcal{L}_\theta = \theta \frac{g_s^2}{32\pi^2} G^a_{\mu\nu}\tilde{G}^{a,\mu\nu}, \tag{2.60}$$

where $\tilde{G}^{a,\mu\nu} := {}^1\!/\!_2 \epsilon^{\mu\nu\rho\sigma} G^a_{\mu\nu}$ is the dual field strength tensor and θ is a dimensionless parameter that quantifies the strength of CP violation. The operator is CP violating because it conserves C ($G^a_\mu \to -G^a_\mu$) but violates P ($G^a_{0i} \to -G^a_{0i}, G^a_{ij} \to G^a_{ij}$). It is not identically zero even though it is a total derivative of the Chern-Simons current

$$G^a_{\mu\nu}\tilde{G}^{a,\mu\nu} = \partial_\mu K^\mu, \tag{2.61}$$

$$K^\mu = \epsilon^{\mu\nu\rho\sigma}\mathrm{Tr}\left(G_\nu \partial_\rho G_\sigma - \frac{2}{3}\mathrm{i}g_s G_\nu G_\rho G_\sigma\right) \tag{2.62}$$

and hence does not contribute to the equations of motion [34]. However, it encodes the topological structure of the gauge field configurations, which include non-trivial vacua labelled by winding numbers n. The θ-term contributes a phase factor $\exp(\mathrm{i}\theta n)$ to the path integral, determining the relative weight of vacuum sectors of different n, meaning that it explicitly distinguishes between these configurations related by CP symmetry [35]. However, particle masses are not yet introduced, and with this absence of masses, the QCD Lagrangian possesses an axial $U(1)_A$ symmetry. The anomaly of which relates the divergence of the axial current to the topological structure of the gauge field

$$\partial_\mu(\bar{q}\gamma^\mu\gamma_5 q) = \frac{g_s^2}{32\pi^2} G^a_{\mu\nu}\tilde{G}^{a,\mu\nu}. \tag{2.63}$$

Chirally rotating the quark fields $q \to \exp(\mathrm{i}\alpha\gamma_5)q$ changes the measure of the path integral proportional to the θ-term and consequently shifts it. In the massless case, the phase can be chosen as $\alpha = -\theta/(2N_f)$ such that θ would become unobservable. This changes, however, in the massive case, where it cannot be eliminated and as such remains a source of CP violation. A physical observable to which it contributes is the neutron electric dipole moment [36], which puts a limit on $|\theta| \leq 10^{-10}$, the unnatural smallness of which is the so-called strong CP problem. One proposed solution to it is the Peccei-Quinn mechanism, which introduces a new pseudoscalar field, the axion, that dynamically drives θ to zero [37].

Electroweak Theory

In contrast to QCD, the electroweak (EW) sector is based on two gauge groups, the $SU(2)_L$, which corresponds to weak isospin, and the $U(1)_Y$, which corresponds to weak hypercharge. The Lie algebra $\mathfrak{su}(2)$ contains 3 elements, corresponding to the three gauge bosons W^a_μ, while the $\mathfrak{u}(1)_Y$ is one-dimensional and represents the gauge boson B_μ [26]. In the SM only the left-handed fermions carry weak isospin coupled with the coupling constant g, while the B-boson couples to the weak hypercharge carried by both chiralities with the coupling constant g' [21]. The full Lagrangian is written as [17]

$$\begin{aligned}\mathcal{L}_{\text{EW}} =& -\frac{1}{4}W^a_{\mu\nu}W^{a,\mu\nu} - \frac{1}{4}B_{\mu\nu}B^{\mu\nu} - \frac{1}{2\xi_W}\left(\partial^\mu W^a_\mu\right)^2 - \frac{1}{2\xi_B}\left(\partial^\mu B_\mu\right)^2 \\ &+ \overline{\psi}_{f,L}\mathrm{i}\not{D}\psi_{f,L} + \overline{\psi}_{f,R}(\mathrm{i}\not{\partial} + g'Y_f\not{B})\psi_{f,R} + \chi^{a*}\partial^\mu D^{ab}_\mu\chi^b,\end{aligned} \tag{2.64}$$

where $\psi_{f,L}$ is a left-handed weak isospin doublet containing the left-handed fermion fields of the SM fermions and $\psi_{f,R}$ is the right-handed weak isospin singlet containing the right-handed fermion field of some flavour f. As before, analogous to the QCD θ-term one for the electroweak sector could be written with the W boson fields, which would lead to CP violation. However, even after the introduction of masses in the next paragraph, it can be rotated away due to the chiral nature of the interactions [38, 39]. As the W bosons only couple to left-handed fermions, simultaneous chiral rotations of left- and right-handed fermions are allowed, eliminating $\theta_{SU(2)}$. This freedom does not exist in QCD, where the gluons couple equally to both left- and right-handed quarks. The chiral rotations necessary to remove the θ-term would introduce complex phases to the quark masses, which itself entails CP-violation.

Spontaneous Symmetry Breaking

The inclusion of mass terms for gauge bosons and fermions would explicitly break gauge invariance [40]. One concept to introduce mass terms without violating gauge invariance is the Higgs mechanism [41] in which a new complex scalar field, the Higgs field, is coupled to the massive gauge bosons and fermions as

$$\begin{aligned}\mathcal{L}_{\text{Higgs}} =& (D_\mu H)^\dagger(D_\mu H) - \left(-\mu^2 H^\dagger H + \lambda(H^\dagger H)^2\right) \\ &- y^u_{ij}\overline{Q}^i_L\tilde{H}U^j_R - y^d_{ij}\overline{Q}^i_L H D^j_r - y^l_{ij}\overline{L}^i_L H E^j_r + \text{h.c.}\,.\end{aligned} \tag{2.65}$$

The covariant derivative is the same as in the electroweak Lagrangian, coupling the weak gauge bosons to the Higgs field H, a weak isospin doublet. The fermions are coupled to the Higgs field via the Yukawa couplings (y_u, y_d, y_e) being three-dimensional matrices in generation space

[17]. Since these Yukawa terms are not hermitian, their conjugate (h.c.) has to be added. There is no term with a right-handed neutrino ν_R here. Although it is experimentally established that neutrinos have non-vanishing masses, the exact process or processes of their emergence is not established yet [42–44]. The last term in the first line is the Higgs potential with scalar parameters μ and λ. In the unbroken phase, the content of the physical fields is compiled in Tab. 2.1. If $\mu^2 > 0$ and $\lambda > 0$, it exhibits a minimum for a non-zero Higgs field configuration at $H^\dagger H = {}^{\mu^2}\!/_{2\lambda} := {}^{v^2}\!/_2$ with the vacuum expectation value $\langle H \rangle = v$ [45]. This spontaneously breaks the original electroweak group symmetry to the subgroup $U(1)$ in the vacuum but does not affect the underlying gauge symmetry [46]. This is the Higgs mechanism. The subgroup is identified as the electromagnetic $U(1)_{\text{em}}$ with the generator $Q := T_3 + {}^Y\!/_2$ where T_3 is the third generator of the $SU(2)_L$ and Y is the weak hypercharge.

Spontaneous breaking of a continuous symmetry leads to the appearance of massless scalar excitations called Goldstone bosons, as stated by the Goldstone theorem [47]. Spontaneous breaking means that $\langle [J^a, H] \rangle \neq 0$ with J^a denoting the broken generators of the symmetry. For each broken generator, a Goldstone boson is predicted. The Higgs field can be parametrised to explicitly include these Goldstone bosons in a standard representation as [21]

$$H(x) = \frac{1}{\sqrt{2}} \begin{pmatrix} \sqrt{2}\, G^+(x) \\ v + h(x) + \mathrm{i}G^0(x), \end{pmatrix} \tag{2.66}$$

with G^+ (G^0) are the charged (neutral) Goldstone bosons and the physical Higgs boson h. Evaluating the interaction terms with the covariant derivative in Eq. (2.65) at vacuum introduces the mass terms for the gauge bosons. Diagonalisation into physical fields yields the Z_μ and the $W^\pm_\mu$ bosons and the photon with masses $M_W = {}^{ev}\!/_{2s_W}$, $M_Z = {}^{M_W}\!/_{c_W}$ and $M_A = 0$ with the

fermions	$\mathcal{G}_{\text{SM}}$	bosons	$\mathcal{G}_{\text{SM}}$
quarks		2-tensors	
Q^i_L	$({}^1\!/_3, 2, 3)$	B	$(0, 1, 1)$
U^i_R	$({}^4\!/_3, 1, 3)$	W^a	$(0, 3, 1)$
D^i_R	$(-{}^2\!/_3, 1, 3)$	G^a	$(0, 1, 8)$
leptons		scalars	
E^i_R	$(-2, 1, 1)$	H	$(1, 2, 1)$
L^i_L	$(-1, 2, 1)$		

Table 2.1: The particle fields of the SM in the unbroken phase with the full gauge symmetry $\mathcal{G}_{\text{SM}} = U(1)_Y \times SU(2)_L \times SU(3)_C$. The numbers in the round brackets denote the representations of the respective field under the symmetry groups. For the $U(1)_Y$ symmetry, the charge is denoted. The upper index i of the fermion fields denotes the generation.

electrical charge e and the sine (cosine) of the Weinberg angle s_W (c_W) that rotates the neutral W^3_μ and B-boson into the physical Z_μ and the photon. The longitudinal polarisations of the massive gauge bosons originate from the Goldstone bosons, modifying their gauge fixing and ghost terms.

Fermion masses emerge through the Yukawa interaction with the Higgs field [46]. To write a mass term for each fermion, the respective Yukawa matrices have to be diagonalised. For the quarks, these are the unitary matrices U_u with V_u (U_d with V_d) for the up-type (down-type) quarks, respectively. However, they cannot be diagonalised independently because the left-handed up-type and down-type quark get transformed together. This mismatch between the diagonalisation of the Yukawa matrices is encoded in the CKM matrix [48]

$$V_{\text{CKM}} = U_u^\dagger U_d. \tag{2.67}$$

With three generations, this is a three-dimensional unitary matrix. Considering the parameters of a unitary $n \times n$ matrix that are physical, i.e., not absorbed by redefining phases of the fermion fields, there are $(n-1)^2$ parameters. For $n = 3$, three parameters denote mixing angles and one a complex phase δ. This complex phase is responsible for the CP violation in the electroweak sector [21].

Accidental Symmetries

In addition to the spacetime and the gauge, the SM exhibits accidental global symmetries that are not explicitly imposed but emerge due to the constraints of gauge invariance and renormalisability. Among these symmetries are the baryon number B conservation, lepton number L conservation, and the combination of $B - L$ [49]. Although they are not fundamental principles of the SM, they are conserved because the renormalisable operators allowed by the SM do not violate it. However, higher-dimensional operators may enable the symmetry violation [50]. In the SM, baryon number is defined as a global $U(1)_B$ symmetry under which (anti-)quarks carry $+1/3$ ($-1/3$) while leptons and gauge bosons are neutral. Similarly, lepton symmetry is defined such that (anti-)leptons carry charge $+1$ (-1). One example of a higher-dimensional operator that violates both B and L but conserves $B - L$ is [50]

$$O_{qqql} = \frac{1}{\Lambda^2}\epsilon^{ijk}\left(\bar{q}_{Li}q_{Lj}\right)\left(\bar{q}_{Lk}l_L,\right) \tag{2.68}$$

with Λ being an energy scale higher than the vacuum expectation value of the Higgs potential. Grand Unified Theories (GUTs) and supersymmetry theories (SUSY) predict such B-violating processes, e.g. [51–54] . Such a violation is essential for explaining the baryon asymmetry of the universe (BAU) which will be discussed further in Sec. 3.2.3.

2.3 Renormalisation

Renormalisation is a procedure in QFTs that addresses the ultraviolet (UV) divergences appearing in perturbative calculations of observables. The divergences arise from loop corrections to Green functions. The main concept of renormalisation is that measurable quantities are not the bare parameters of the Lagrangian but have the effects of quantum loop corrections incorporated. Renormalisation absorbs systematically the divergences by introducing a regularisation scheme that explicitly parametrises and subsequently cancels them. We employ dimensional regularisation (DimReg) [55, 56] because it preserves the symmetries of the QFT, linearity, scaling, and the translation invariance of the integral and the $\overline{\text{MS}}$ [57] renormalisation scheme, which absorbs the infinite terms into renormalisation constants order by order in the quantities. See [58] for details.

Dimensional Regularisation

When calculating corrections to the tree-level amplitudes, loop diagrams imply the integration over internal momenta q. In four-dimensional spacetime, the integral generally does not converge, with degrees of divergence being logarithmic or higher [21]. DimReg changes the spacetime dimension to $d = 4 - 2\epsilon$ with $\epsilon > 0$ effectively reducing the degree of divergence. The integral $\int \,\mathrm{d}^d p f(p)$ is then rendered finite with some function f, defined on an infinite-dimensional vector space. During the evaluation of the integral in d-dimensional spherical coordinates, Euler gamma functions arise [58]

$$\int \mathrm{d}^d p \frac{(p^2)^n}{(p^2+m^2)^m} = \pi^{(d/2)} m^{(d+2n-2m)} \frac{\Gamma(n+d/2)\Gamma(m-n-d/2)}{\Gamma(d/2)\Gamma(m)}, \tag{2.69}$$

with $n, m \in \mathbb{R}$, defined as $\Gamma(z) := \int_0^\infty \,\mathrm{d}t t^{z-1} \mathrm{e}^{-t}$ which converges for $\mathrm{Re}(z) > 0$. Arguments with negative real part are extended through the recurrence relation $\Gamma(z-1) = \Gamma(z)/(z-1)$. However, $\Gamma(-z)$ has single poles for $z \in \mathbb{N}_0$, requiring an expansion near these singularities which can be expressed as

$$\begin{aligned}
\Gamma(-z+\epsilon) =& \Gamma(\epsilon) \prod_{k=1}^{z} (\epsilon - k)^{-1} = \frac{1}{\epsilon} \exp\left(-\gamma\epsilon + \sum_{n=2} \frac{(-1)^n}{n} \zeta(n) \epsilon^n \right) \prod_{k=1}^{z} (\epsilon - k)^{-1} \\
=& \frac{(-1)^z}{z!} \left[\frac{1}{\epsilon} - \gamma + \frac{\epsilon}{12}(6\gamma^2 + \pi^2) + \frac{\epsilon^2}{12}\left(-\gamma\pi^2 - 2\gamma^3 + 4\zeta(3)\right) + \mathcal{O}\left(\epsilon^3\right) \right] \\
& \times \left[1 + \sum_{n=1} \epsilon^n \prod_{k=1}^{n} \left(\sum_{i_k=0}^{z-1-\sum_{j=1}^{k-1} i_j} \frac{1}{z - \sum_{j=1}^{k} i_j} \right) \right]
\end{aligned} \tag{2.70}$$

for $\epsilon \ll 1$. This expansion highlights the emergence of ϵ-poles which are isolated and renormalised later. A significant property of d-dimensional integrals is that scaleless integrals vanish

$\int \mathrm{d}^d q q^a = 0$ as they do not contain an inherent scale to regularise them [58]. Additionally, the metric tensor satisfies $\eta^{\mu\nu}\eta_{\mu\nu} = d$, which extends to Dirac matrices, implying

$$\gamma^\mu \gamma_\mu = \frac{1}{2}\left\{\gamma^\mu, \gamma_\mu\right\} = \eta^\mu_\mu = d. \tag{2.71}$$

The treatment of γ_5 in DimReg presents subtle challenges. The issue arises because the transition of γ_5 from $d \to 4$ is not meromorphic. The common anticommutation relation $\{\gamma^\mu, \gamma_5\} = 0$ conflicts with the extension of trace operations involving γ_5 in d-dimensions. Using the cyclicity property of the trace and Eq. (2.71) we find that

$$(4-d)\mathrm{Tr}(\gamma_5 \gamma_\mu \gamma_\nu \gamma_\rho \gamma_\sigma) = 0, \tag{2.72}$$

which results in the trace being zero for arbitrary dimensions. However, for $d = 4$, we have $\mathrm{Tr}(\gamma_5 \gamma_\mu \gamma_\nu \gamma_\rho \gamma_\sigma) = 4\mathrm{i}\epsilon_{\mu\nu\rho\sigma}$. To resolve this inconsistency, one either refrains from using DimReg when treating traces in fermion loops [59, 60] or from the naive anticommutation relation [56, 61] where we present the latter. This is called the Breitenloher-Maison-'t Hooft-Veltman scheme. The expedient is to split the Dirac matrices into a four-dimensional and a $(d-4)$-dimensional part, *i.e.*,

$$\gamma^\mu = \hat{\gamma}^\mu + \tilde{\gamma}^\mu \tag{2.73}$$

where $\hat{\gamma}^\mu$ spans the four-dimensional subspace and $\tilde{\gamma}^\mu$ the $(d-4)$-dimensional complement. The commutation relations are then

$$\begin{aligned} &\{\hat{\gamma}^\mu, \gamma_5\} = 0, && [\tilde{\gamma}^\mu, \gamma_5] = 0, && \hat{\eta}^\mu_\mu = 4, \\ &\{\hat{\gamma}^\mu, \tilde{\gamma}^\nu\} = 0, && \{\gamma^\mu, \gamma_5\} = 2\gamma_5\tilde{\gamma}^\mu, && \tilde{\eta}^\mu_\mu = d-4. \end{aligned} \tag{2.74}$$

Non-vanishing results may occur for [62]

$$\mathrm{Tr}\left(\gamma_5 \hat{\gamma}^{\mu_1} ... \hat{\gamma}^{\mu_{2m}} \tilde{\gamma}^{\nu_1} ... \tilde{\gamma}^{\nu_{2n}}\right) \tag{2.75}$$

in all d if $m, n \in \mathbb{N}$ and $m \geq 2$. The common trace identities with γ_5 in 4 dimensions can be used, and the projection of the $(d-4)$-dimensional on the metric employed. Contracted with particle momenta $\tilde{p}^2 = {}^1\!/_d(d-4)p^2$ can be used. These traces typically occur in triangle anomaly Feynman diagrams [63].

Renormalisation Group Equations

Consider Eq. (2.59) with all fields and parameters interpreted as "bare" quantities (with subscript 0). These do not reflect the physical values such as coupling constants or masses, as they obtain divergent contributions from e.g., self-energy diagrams. To obtain a renormalised Lagrangian we relate them to their renormalised equivalent by the aforementioned renormalisation constants Z. They are infinite too, so that they cancel the divergences of the bare quantities. Insisting that the quantum action $\int d^d x \mathcal{L}$ remains dimensionless, the mass dimension of the coupling constants becomes non-zero [56]. We compensate for this by introducing a mass scale μ [64] with an appropriate power

$$\begin{aligned} G^A_{0,\mu} &= Z_G^{1/2} G^A_\mu, & q_0 &= Z_q^{1/2} q, & \chi^A_0 &= Z_\chi^{1/2} \chi^A, \\ g_0 &= Z_g \mu^\epsilon g, & \xi_0 &= Z_\xi \xi, & m_0 &= Z_m m. \end{aligned}$$

The renormalised Lagrangian then only contains the renormalised quantities and the renormalisation constants. These constants are determined by the singularities in the Green's functions. In the $\overline{\text{MS}}$ scheme, the renormalised coupling constants and masses depend on the renormalisation scale μ_1. The observables measured in an experiment are dominated by effects potentially at some other scale μ_2. To constrain the renormalised parameters with the measurements, they have to be related to μ_2. Since the bare quantities are μ-independent, we find for the renormalised coupling constant ($\alpha = g^2/(4\pi)$, $Z_\alpha = Z_g^2$) and mass

$$\frac{\mathrm{d}\alpha}{\mathrm{d}\log\mu} = \beta(\epsilon,\alpha) = -2\epsilon\alpha + \beta(\alpha) = -2\epsilon\alpha - \frac{1}{Z_\alpha}\frac{\mathrm{d}Z_\alpha}{\mathrm{d}\log\mu}\alpha \tag{2.76}$$

$$\frac{\mathrm{d}m}{\mathrm{d}\log\mu} = -\gamma(\alpha)m = -\frac{1}{Z_m}\frac{\mathrm{d}Z_m}{\mathrm{d}\log\mu}m. \tag{2.77}$$

We call these differential equations the renormalisation group equations (RGEs) [64]. Further, $\beta(\alpha)$ and $\gamma(\alpha)$ are called the β-function and the anomalous dimension matrix (ADM) [17, 65, 66], respectively, and expand as

$$\beta(\alpha) = -2\sum_{n=2}^{\infty}\beta_{n-2}\left(\frac{\alpha}{4\pi}\right)^n, \tag{2.78}$$

$$\gamma(\alpha) = \sum_{n=1}^{\infty}\gamma^{(n-1)}\left(\frac{\alpha}{4\pi}\right)^n. \tag{2.79}$$

The μ dependence of the renormalisation constants in Eqs. (2.76) and (2.77) is encoded in $\alpha = \alpha(\mu)$ that we use to express them in the expansion

$$Z_k = 1 + \sum_{m=1}^{\infty}\left(\frac{\alpha}{4\pi}\right)^m \sum_{n=0}^{m}\frac{1}{\epsilon^n}Z_k^{(m,n)}. \tag{2.80}$$

Cutting after α^1 denotes leading order (LO) while further terms ($\sim \alpha^l$) then refer to next-to-next-to-...-leading order (N^{l}LO). These constants are used to cancel out the divergences in the

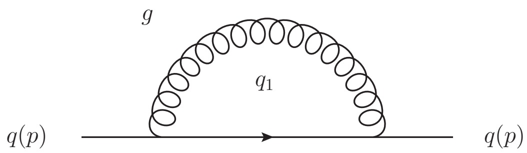

Figure 2.1: One-loop QCD Feynman diagram for the quark self-energy to calculate the mass renormalisation constant Z_m. The quark has an external momentum p and the internal momentum is q_1.

parameters of the bare Lagrangian, organised in the counterterm Lagrangian.

One illustrative example is an exercise from [67] wherein the mass renormalisation constant Z_m and the mass anomalous dimension γ_m are computed in one-loop QCD. We consider now only the third line of the not yet renormalised QCD Lagrangian

$$\mathcal{L}_{\text{QCD}} \subset \bar{q}_0 \left(\mathrm{i}\partial\!\!\!/ - g_{s,0} T^A G^A_{\mu,0} - m_q \right) q_0, \tag{2.81}$$

containing a generic quark field q. It gets renormalised by adding the counterterm Lagrangian [58]

$$\mathcal{L}_{\text{c.t.}} = \bar{q}[\mathrm{i}(Z_q - 1)\partial\!\!\!/ - (Z_q Z_m - 1) m_q] q \tag{2.82}$$

where we left out the renormalisation constants for the gauge field and the coupling constant, as they are not needed here. To obtain γ_m we have to calculate the Feynman diagram depicted in Fig. 2.1 once with the insertion of the mass operator and with the quark propagation operator, respectively. The loop integral with the mass operator insertion is

$$I_m = -\mathrm{i}(g_s \mu^\epsilon)^2 \int \frac{\mathrm{d}^d q_1}{(2\pi)^d} \gamma_\mu T^A \frac{q\!\!\!/_1}{q_1^2} m_q \frac{q\!\!\!/_1}{q_1^2} \gamma_\nu T^B \frac{g^{\mu\nu} \delta^{AB}}{(q_1 - p)^2}. \tag{2.83}$$

We set $m_q \ll q$ as the singularity stems from the high momentum region [58]. The integral is solved with Feynman parameters to

$$I_m = \frac{\alpha_s}{4\pi} 4 C_F m_q \left(\frac{1}{\epsilon} - \log\left(\frac{-p^2}{\mu} \right) + \frac{3}{2} \right) = \frac{\alpha_s}{4\pi} \frac{4 C_F}{\epsilon} m_q + \text{finite}. \tag{2.84}$$

This result is typical for this sort of calculation. The divergence and the logarithm result from the expansion for small ϵ of the Euler Gamma function, Eq. (2.70) and the $\mu^{2\epsilon}$ factor, respectively. Their coefficients are equal. With the divergent part of the integral, we can infer the renormalisation constant $Z_q Z_m$ to be

$$Z_q Z_m = 1 - \frac{\alpha_s}{4\pi} \frac{1}{\epsilon} 4 C_F. \tag{2.85}$$

Now, similarly to before, we calculate the one-loop contribution to the quark propagator with the loop integral

$$I_q = -\mathrm{i}(g_s\mu^\epsilon)^2 \int \frac{\mathrm{d}^d q_1}{(2\pi)^d} \gamma_\mu T^A \frac{\not{p} - \not{q}_1}{(p-q_1)^2} \gamma_\nu T^B \frac{g^{\mu\nu}\delta^{AB}}{q_1^2} \tag{2.86}$$

with the solution

$$I_q = \frac{\alpha_s}{4\pi} C_F \not{p} \left(\frac{1}{\epsilon} - \log\left(\frac{-p^2}{\mu}\right) + 3 \right) = \frac{\alpha_s}{4\pi} \frac{C_F}{\epsilon} \not{p} + \text{finite}. \tag{2.87}$$

Again, the divergent part gets cancelled by the counterterm $\bar{q} Z_q \not{p} q$ with the renormalisation constant

$$Z_q = 1 - \frac{\alpha_s}{4\pi} \frac{1}{\epsilon} C_F. \tag{2.88}$$

We can now use Eqs. (2.85) and (2.88) to obtain

$$Z_m = 1 - \frac{\alpha_s}{4\pi} \frac{1}{\epsilon} 3 C_F + \mathcal{O}(\alpha_s^2). \tag{2.89}$$

To relate Z_m to the ADM, we first transform Eq. (2.77)

$$\gamma_m(\alpha_s) = \frac{1}{Z_m} \frac{\mathrm{d}Z_m}{\mathrm{d}\log\mu} = \frac{1}{Z_m} \frac{\mathrm{d}Z_m}{\mathrm{d}\alpha_s} \frac{\mathrm{d}\alpha_s}{\mathrm{d}\log\mu} = \frac{1}{Z_m} \frac{\mathrm{d}Z_m}{\mathrm{d}\alpha_s} \beta(\epsilon, \alpha_s) \tag{2.90}$$

which we can evaluate to the desired order in α_s with Eqs. (2.76), (2.78) and (2.80). Expanding in ϵ to zeroth order and requiring finiteness of $\gamma(\alpha)$ we obtain the first two terms of the expansion in Eq. (2.79) as

$$\gamma^{(0)} = -2Z^{(1,1)} \tag{2.91}$$

$$\gamma^{(1)} = -4Z^{(2,1)} + 2Z^{(1,1)}Z^{(1,0)} + 2Z^{(1,0)}Z^{(1,1)} + 2\beta_0 Z^{(1,0)}. \tag{2.92}$$

Due to the vanishing of the divergent terms, relations among the renormalisation constants such as

$$2Z^{(2,2)} - Z^{(1,1)}Z^{(1,1)} - \beta_0 Z^{(1,1)} = 0. \tag{2.93}$$

Note that we treat the renormalisation constants as non-commutative, as they can be matrices in the context of operator mixing discussed in Sec. 2.4. To complete the exercise, we take our result for the renormalisation constant Z_m in Eq. (2.89) and utilise the relation in Eq. (2.91) to obtain

$$\gamma_m(\alpha_s) = \frac{\alpha_s}{4\pi} 6C_F + \mathcal{O}(\alpha_s^2). \tag{2.94}$$

The calculation of the mass anomalous dimension illustrates how renormalisation impacts the scale dependence of physical quantities [17]. It shows that the quark mass evolves logarithmically with the renormalisation scale μ. This evolution encapsulates the effect of high-energy quantum fluctuations on low-energy observables, which is particularly significant in effective field theories, where massive degrees of freedom are systematically integrated out.

2.4 Effective Field Theory

In many physical systems, it is unnecessary to include every degree of freedom in the complete theory in order to accurately estimate a matrix element. At energies well below a certain mass scale μ, particles with larger masses are not observable in experiments and can be considered as propagators starting and ending in the same spacetime point. If the symmetries of the full theory allow for couplings between the lower-mass particles and the heavier ones, the effect of the heavy particles can still be observed in the coupling strengths of interactions among the lighter particles. To capture this low-energy effect while keeping the more massive degrees of freedom stationary, a formalism called "effective field theory" (EFT) is used. See [68–70] for more details. The term "full theory" simply implies that the heavy particles are treated as dynamical degrees of freedom, but there may be even heavier particles that are not included in the model. The EFT approach has proven to be a powerful tool for understanding the behaviour of physical systems at low energies.

Matching conditions

An EFT Lagrangian is expressed as an expansion in operators of increasing mass dimension

$$\mathcal{L}_{\text{EFT}} = \mathcal{L}_{\text{ren}} + \sum_{n\geq 5} \sum_{k} \frac{1}{\Lambda^{n-4}} C_k^{(n)}(\mu) O_k^{(n)}(\mu). \tag{2.95}$$

The Wilson coefficients $C(\mu)$ (WCs) [71] are scalar quantities, which contain properties of the heavy particles. They are divided by some appropriate power of a mass scale Λ below which the EFT is valid. This keeps the action $\mathcal{S}$ dimensionless. The scale μ is arbitrary but chosen such that the calculation is simplest, often at the order of momentum transfer in an interaction. The operators $O(\mu)$ are local compositions of particle fields with small masses w.r.t. the mass scale μ and their derivatives constrained by the symmetries of the EFT. A critical step in constructing an EFT is the matching condition, where it is defined to reproduce the amplitude of the full theory at a matching scale μ_0, usually chosen at the scale of the heavy degrees of freedom not present in the EFT, i.e., $\mathcal{A}_{\text{full}} = \mathcal{A}_{\text{eff}}$ with

$$\mathcal{A}_{\text{full}} = \left[\sum_{n=0} \left(\frac{\alpha_s}{4\pi}\right)^n A_i^{(n)}\right] \langle O_i \rangle^{(0)} \tag{2.96}$$

$$\mathcal{A}_{\text{eff}} = C_i(\mu_0) \left[\delta_{ij} + \sum_{n=1} \left(\frac{\alpha_s(\mu_0)}{4\pi}\right)^n r_{ij}^{(n)}\right] \langle O_j \rangle^{(0)}. \tag{2.97}$$

The higher-order matrix elements are expressed in terms of the tree-level matrix element $\langle O_i \rangle^{(0)}$ using the coefficients r being matrices encoding the higher-order corrections. This ensures that the observables are consistent between the two theories. Here we only consider expansion in the strong coupling, but, in principle, the other coupling constants and their mixtures could also be included. The matching process determines the initial conditions of the WCs in the EFT, order by order as

$$C_i(\mu_0) = \sum_{n=0} \left(\frac{\alpha_s(\mu_0)}{4\pi}\right)^n \sum_{k=0}^{n} (-1)^k A_j^{(n-k)} \sum_{a_1+a_2+\cdots+a_k=n-k} \prod_{m=1}^{k} r_{ij}^{(a_m)}. \tag{2.98}$$

The calculation of the amplitudes $A_i^{(n)}$ and the renormalisation coefficients $r_{ij}^{(n)}$ ($r^{(0)} = 1$) involves evaluating Feynman diagrams at the respective order in perturbation theory. For example, $A^{(1)}$ is determined by calculating one-loop diagrams in the full theory involving a gluon exchange between quarks, as in Fig. 2.1. This result is then projected onto the EFT by equating it with the Feynman rules of the effective operators at tree-level. They are derived with the path integral formalism (Eq. (2.21)) by conducting the functional derivatives w.r.t. the sources of all fields therein. The renormalisation coefficients describe the mixing of effective operators under renormalisation at fixed-order perturbation theory. They differ conceptually from the anomalous dimension γ, as they are the expansion coefficients of the renormalisation constants Z_{ij} but are related, similar to Eq. (2.91).

In Sec. 4.1 we calculate 3-point Feynman diagrams at 2-loop order in the electroweak interactions. To match the results with the EFT below its scale, they have to be projected completely onto the effective operators, for which an appropriate operator basis is required. Complete bases consisting of SM fields in the unbroken phase (SMEFT) have been constructed for mass dimensions up to $n = 9$ [72].

RG improved perturbation theory

As in the last section, the renormalisation group equations (RGE) for the WCs are used to connect their values at different renormalisation scales and refine predictions of the EFT by summing large logarithmic corrections that arise due to scale separations. The differential equation describing the evolution between scales is derived by the scale independence of the bare WCs as [58]

$$\frac{\mathrm{d}C(\mu)}{\mathrm{d}\log\mu} = \gamma^T C(\mu), \tag{2.99}$$

where γ is a matrix with the dimension of the operator basis. One solution to this differential equation is [17]

$$C(\mu) = U(\mu,\mu_0)C(\mu_0), \tag{2.100}$$

with a scale-dependent operator that encodes the cumulative effect of the anomalous dimension between the scales μ_0 and μ, constructed as [73]

$$U(\mu,\mu_0) = \exp\left(\int\limits_{\alpha_s(\mu_0)}^{\alpha_s(\mu)} \frac{\gamma^T}{2\beta(\alpha_s')}\,\mathrm{d}\alpha_s'\right). \tag{2.101}$$

Note that the integral is ordered in the coupling constants, such that they increase from right to left. This is necessary because the anomalous dimension matrices do not necessarily commute with each other. The evolution matrix can be evaluated perturbatively by expanding it in the coupling constants as

$$U(\mu,\mu_0) = \sum_{n=0}\left(\frac{\alpha_s(\mu)}{4\pi}\right)^n U^{(n)}(\mu,\mu_0). \tag{2.102}$$

The leading log (LL) term sums the terms proportional to $(\alpha_s\mathrm{log})^n$, where $\mathrm{log} = \log {}^{\mu}/_{\mu_0}$, to all orders in the strong coupling constant. The next (N) higher-order terms then sum terms proportional to $\alpha_s^m(\alpha_s\mathrm{log})^n$ as N^{m}LL. Expanding the WCs similarly to the evolution matrix and using Eq. (2.100) the individual contributions to the WCs can be found as [74]

$$C^{(n)}(\mu) = \sum_{k=0}^{n}\eta^{n-k}U^{(k)}(\mu,\mu_0)C^{(n-k)}(\mu_0), \tag{2.103}$$

where $\eta := \alpha_s(\mu_0)/\alpha_s(\mu)$. To obtain an explicit perturbative description for the evolution matrix, it can be expressed by the leading order term as

$$U(\mu,\mu_0) = K(\mu)U^{(0)}K^{-1}(\mu_0), \tag{2.104}$$

where K is expanded in the strong coupling as [74]

$$K(\mu) = 1 + \sum_{n=1}\left(\frac{\alpha_s(\mu)}{4\pi}\right)^n J^{(n)}. \tag{2.105}$$

The leading order term of the evolution matrix can be derived from the leading order RGE of the strong coupling to

$$U^{(0)} = V\eta^{\mathrm{diag}(\vec{a})}V^{-1}, \tag{2.106}$$

where the matrix V diagonalises the leading order ADM and the magic numbers a_i determined by the entries of the diagonalised leading order ADM as

$$\left(V^{-1}\gamma^{(0)T}V\right)_{\nless\trianglelefteq} = 2\beta_0 a_{\nless}\delta_{\nless\trianglelefteq}. \tag{2.107}$$

$A_{\nless}$ The J-matrices are calculated with [74]

$$J^{(n)} = VH^{(n)}V^{-1} \tag{2.108}$$

of which the leading order term reads

$$H^{(1)}_{\nless\trianglelefteq} = \frac{\beta_1}{(2\beta_0^2}\gamma^{(0)}_{\nless}\delta_{\nless\trianglelefteq} - \frac{1}{2\beta_0 + \gamma^{(0)}_{\nless} - \gamma^{(1)}_{\trianglelefteq})}G^{(1)}_{\nless\trianglelefteq} \tag{2.109}$$

and

$$G^{(n)} = V^{-1}\gamma^{(n)T}V. \tag{2.110}$$

Putting all Eqs. (2.98), (2.103), (2.104) and (2.105) together yields the result for the WC. Note that in case a threshold in the RGE is reached from higher scales to lower, the evolution matrix has to be recalculated with the respective degrees of freedom integrated out.

Unphysical operators

During intermediate steps of computations, unphysical operators appear but do not contribute directly to physical observables. Two primary classes of unphysical operators are those eliminated by the equations of motion (EOM) and evanescent operators. The EOM can be used to simplify the operator basis by removing redundant operators, using the fact that any operator proportional to the classical EOM of the considered fields vanishes in on-shell matrix elements. For example, consider a scalar field with its EOM $(\partial_\mu\partial^\mu + m^2)\phi = 0$. Any operator containing a term proportional to it can be rewritten in terms of other operators in the EFT basis. However, they are necessary to fully project the full theory onto the EFT.

Evanescent operators arise specifically in the context of dimensional regularisation. They vanish identically in $d = 4$ but mix with physical operators under renormalisation, leading to corrections of order ϵ to the WCs, particularly at two-loop and higher-order calculations. See [74–76] for details. They emerge during the reduction of Dirac structures in loop diagrams, like

$\gamma^\mu\gamma^\nu\gamma^\rho\gamma_\nu\gamma_\mu$ to γ^ρ and in the renormalisation of four-fermion operators. Terms proportional to ϵ emerge and multiplied by $1/\epsilon^2$ singularities in two-loop diagrams, they contribute to the $1/\epsilon$ poles relevant for renormalisation. These contributions are dependent on the renormalisation scheme and on the definition of the evanescent operators.

Chapter 3

Setup - EFTs and Observables

After introducing the key theoretical concepts that are required for this work, we now detail the specific setup of our analysis. This includes the EFTs, namely the κ framework and the Standard Model Effective Field Theory (SMEFT), as well as the experimental observables relevant for constraining the Wilson coefficients. The focus is on the EDMs and collider observables in particular, while constraints from EWBG are discussed in context but will not be included in the subsequent analyses. Finally, an overview of the statistics of global analyses is presented at the end.

3.1 Standard Model Effective Field Theory and the κ Framework

The κ framework

One minimalistic extension of the SM Yukawa interactions is the so-called κ-framework [14], enabling the inclusion of explicit CP-violating effects by the addition of a pseudo-scalar term

$$\mathcal{L}_{hqq} = -\frac{y_q^{\mathrm{SM}}}{\sqrt{2}}\kappa_q \overline{q}\left(\cos\phi_q + i\gamma_5 \sin\phi_q\right) q\, h\,, \tag{3.1}$$

where h denotes the SM Higgs field in the broken phase and q the SM quark fields. Moreover, $y_q^{\mathrm{SM}} \equiv e\, m_q/(\sqrt{2}s_w M_W)$ is the SM Yukawa, with e the positron charge, s_w the sine of the weak mixing angle, and M_W the W-boson mass, respectively. The mass of the light quark q is denoted by m_q. The real parameters $\kappa_q \geq 0$ parameterise modifications to the absolute value of the SM Yukawa couplings, while the phases $\phi_q \in [0, 2\pi)$ parameterise CP violation and the sign of the Yukawa. This parameterisation is motivated by 6-dimensional Yukawa operators in the SMEFT studied in chapter 5. However, only the four-dimensional Yukawa coupling gets modified. The SM value is obtained in the limit $\kappa_q = 1$ and $\phi_q = 0$. In other descriptions, the two terms are parameterised by a CP-conserving κ and a CP-violating $\tilde{\kappa}$ [14]. There, $\kappa \sin\phi \mapsto \tilde{\kappa}$ and $\kappa\cos\phi \mapsto \kappa$.

Standard Model Effective Field Theory - SMEFT

In Sec. 2.2 we introduced several aspects of the SM always as a renormalisable QFT. However, it is very likely that at some scale Λ significantly above the EW scale, new physics effects have to be considered. Up to this new physics scale, the SM symmetries are assumed to remain valid, and the Higgs boson is embedded in a weak doublet field, spontaneously breaking the electroweak symmetry. Higher-dimensional operators, suppressed by Λ, are only constructed out of the unbroken SM field content obeying the gauge symmetries. This is SMEFT [77], see [15, 78] for details. At dimension six, a consistent basis can be constructed of 2499 baryon number-preserving operators in the case of three fermion generations. The Higgs potential in the SMEFT is

$$V(H) = \lambda \left(H^\dagger H - \frac{1}{2}v^2\right)^2 - \frac{C_H}{\Lambda^2}\left(H^\dagger H\right)^3, \tag{3.2}$$

yielding the vev shifted $v^2 \to v_T^2 = (1 + 3C_H v^2/(8\lambda\Lambda^2))v^2$ to linear order in C_H [79].

In Ch. 5, we consider the SM augmented with SMEFT operators that induce tree-level modifications to the Yukawa couplings. In the unbroken phase, the relevant part of the Lagrangian reads [78]

$$\begin{aligned} \mathscr{L}_{\text{Yukawa}} = &- \bar{Q}_L \tilde{H} Y_u u_R + \frac{1}{\Lambda^2}(H^\dagger H)\bar{Q}_L \tilde{H} C'_{uH} u_R \\ &- \bar{Q}_L H Y_d d_R + \frac{1}{\Lambda^2}(H^\dagger H)\bar{Q}_L H C'_{dH} d_R \\ &- \bar{L}_L H Y_\ell \ell_R + \frac{1}{\Lambda^2}(H^\dagger H)\bar{L}_L H C'_{\ell H} \ell_R + \text{h.c.}\,. \end{aligned} \tag{3.3}$$

Here, u_R, d_R, ℓ_R denote the triplets (in generation space) of right-handed up-, down-, and charged-lepton fields, while Q_L and L_L are the corresponding left-handed triplets. In accordance, the Yukawa matrices Y_u, Y_d, Y_ℓ and Wilson coefficients (WCs) C'_{uH}, C'_{dH}, $C'_{\ell H}$, are generic complex 3×3 matrices. The primes indicate that they are not necessarily couplings in the mass-eigenstate basis. Phases in the Yukawa couplings and WCs can potentially induce beyond-the-SM (BSM) CP-violating contributions to Higgs-Yukawa couplings.

Crucial for the correct initial conditions for the UV-sensitive term in the effective operator basis are the dipole operators in the unbroken phase

$$\begin{aligned} \mathcal{L}_{\text{dipole}} = &+ \frac{C_{eB}}{\Lambda^2}\bar{L}_L \sigma^{\mu\nu} e_R H B_{\mu\nu} + \frac{C_{uB}}{\Lambda^2}\bar{Q}_L \sigma^{\mu\nu} u_R \tilde{H} B_{\mu\nu} + \frac{C_{dB}}{\Lambda^2}\bar{Q}_L \sigma^{\mu\nu} d_R H B_{\mu\nu} \\ &+ \frac{C_{eW}}{\Lambda^2}\bar{L}_L T^a \sigma^{\mu\nu} e_R H W^a_{\mu\nu} + \frac{C_{uW}}{\Lambda^2}\bar{Q}_L T^a \sigma^{\mu\nu} u_R \tilde{H} W^a_{\mu\nu} \\ &+ \frac{C_{dW}}{\Lambda^2}\bar{Q}_L T \sigma^{\mu\nu} d_R H W^a_{\mu\nu} + \text{h.c.}\,. \end{aligned} \tag{3.4}$$

At the two-loop electroweak order, the 6-dimensional Yukawa operators in Eq. (3.3) mix into the dipole moment operators of the B and W bosons [80]. The matching on the EDM operator at the electroweak scale creates the leading term for its initial condition. No similar contribution to the chromo-EDM operator comes from a mixing from the Yukawa operators.

3.2 Constraining Observables

3.2.1 Electric Dipole Moments

An electric dipole moment (EDM) quantifies the charge distribution within a particle. It is an expectation value of an operator, defined as

$$\vec{d} = \sum_i \vec{r}_i e_i, \tag{3.5}$$

with position vectors $\vec{r}_i$ and the charge of the constituent particles e_i, see [81–83]. For a fermion, such as the neutron, the expectation value of the EDM operator is proportional to its spin angular momentum

$$\langle N, s|\vec{d}|N, s\rangle = C\langle N, s|\vec{J}|N, s\rangle \tag{3.6}$$

where C is a proportionality constant, $\vec{J}$ is the angular momentum operator, and $|N, s\rangle$ is the spin state of the neutron. The presence of an EDM implies that $\vec{d}$ does not vanish, breaking T symmetry. Under time reversal, $\vec{d}$ and $\vec{J}$ transform as

$$T\vec{d}T^{-1} = \vec{d}, \qquad T\vec{J}T^{-1} = -\vec{J}. \tag{3.7}$$

Their different transformation properties are incompatible with T-invariance if $C \neq 0$. More specifically, T-invariance implies a degeneracy of $2j + 1$ states for fermions, see Sec. 2.2, which is lifted in the case of a non-vanishing EDM. However, for bosons, no such degeneracy is protected by T-invariance. Hence, no inherent mechanism is present that would violate the invariance in bosonic systems [29]. The non-relativistic Hamiltonian of the electromagnetic dipole moment d_f of a fermionic system f is

$$\mathcal{H}_{\text{cl}} = -d_f \vec{\sigma} \cdot \vec{E}, \tag{3.8}$$

where $\vec{E}$ is the external electric field and $\vec{\sigma}$ is the Pauli matrix vector representing the spin of the particle. This operator induces a split of the neutron spin states, analogous to the Zeeman effect, where the magnetic moment in a magnetic field experiences an energy splitting. This splitting is the uplifting of Kramers' degeneracy, discussed in Sec. 2.2.

The relativistic generalisation of interaction between a fermion and the electromagnetic

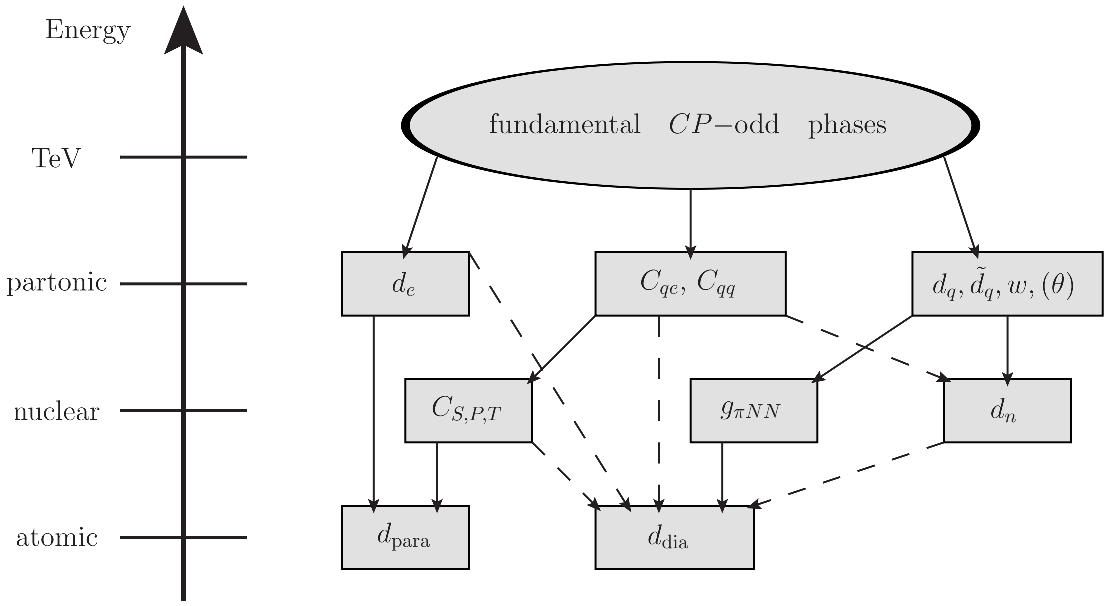

Figure 3.1: Energy scale hierarchy depicting the connection between BSM origins of CP-odd phases and observable EDMs. This figure is an adaptation of [81].

potential is given by this general Lagrangian

$$\begin{aligned}\mathcal{L} = -\bar{\psi}\Bigg[&\gamma^\mu F_1(q^2) + \frac{\mathrm{i}}{2m}q_\nu\left(\sigma^{\mu\nu}F_2(q^2) + \frac{1}{2}\epsilon^{\mu\nu\alpha\beta}\sigma_{\alpha\beta}F_3(q^2)\right)\\ &+\frac{1}{2m}\left(q^\mu - \frac{q^2}{2m}\gamma^\mu\right)\gamma_5 F_4(q^2)\Bigg]\psi A_\mu(q),\end{aligned} \tag{3.9}$$

with the Dirac form factor F_1, the Pauli form factor F_2, the EDM form factor F_3 and the anapole moment F_4 [84]. In the non-relativistic limit, the form factor F_3 is connected to the electric dipole moment as $-{}^1\!/_{2m}\,F_3(0) = d$. This term can be expressed in a gauge-invariant form in spatial coordinates as

$$\mathcal{L}_{\rm EDM} = -\frac{d}{2}\bar{\psi}\sigma^{\mu\nu}\mathrm{i}\gamma_5\psi F_{\mu\nu}. \tag{3.10}$$

It is odd under parity and time-reversal and, hence, violates CP-symmetry.

The calculation of an observable EDM from underlying CP-violating interactions involves renormalisation group evolution over several energy scales, depicted in Fig. 3.1. At the highest scale, presumed to be at the order of a few TeV, the new physics Lagrangian gives rise to CP-violating WCs that are evolved to the nuclear scale to be related to the observable EDMs. These are in general not solely dependent on the EDMs of their partons (Eq. (3.10)) but also include contributions from CP-odd four-fermion operators and nucleon-nucleon pairs. The relevant effective Lagrangian at the nuclear scale is expressed as:

$$\mathcal{L}^{\text{eff}}_{\text{nuclear}} = \mathcal{L}_{\text{EDM}} + \mathcal{L}_{\pi NN} + \mathcal{L}_{eN}, \tag{3.11}$$

with the CP-odd pion-nucleon interaction

$$\mathcal{L}_{\pi NN} = \bar{g}^{(0)}_{\pi NN}\bar{N}T^a N\pi^a + \bar{g}^{(1)}_{\pi NN}\bar{N}N\pi^0 + \bar{g}^{(2)}_{\pi NN}(\bar{N}T^a N\pi^a - 3\bar{N}T^3 N\pi^0) \tag{3.12}$$

and the CP-odd electron-nucleon interaction

$$\mathcal{L}_{eN} = C^{(0)}_S \bar{e}\mathrm{i}\gamma_5 e\bar{N}N + C^{(0)}_P \bar{e}e\bar{N}\mathrm{i}\gamma_5 N + C^{(0)}_T \epsilon_{\mu\nu\alpha\beta}\bar{e}\sigma^{\mu\nu}e\bar{N}\sigma^{\alpha\beta}N \tag{3.13}$$

plus isospin-dependent terms $C^{(1)}_{S,C,P}$ involving the nucleon isospin matrix τ_3. We consider three classes of observable EDMs in our analysis in Ch. 5, paramagnetic atoms and molecules, diamagnetic atoms and the neutron.

Paramagnetic Atoms

Paramagnetic systems contain one or more unpaired electrons. The observable EDM in such systems primarily arises due to the contributions of the intrinsic electron EDM d_e and the scalar CP-odd electron-nucleus interaction described by C_S

$$d_{\text{para}} = k_1 d_e + k_2 C_S, \tag{3.14}$$

with system-specific enhancement factors k_1, k_2. The pseudoscalar C_P and tensor coupling C_T do not contribute significantly relative to the scalar coupling. The scalar term directly couples the electron CP-odd axial spin density to the nucleus scalar charge density. The pseudoscalar term involves the interaction with the nuclear axial charge density. This is suppressed, as it does not induce a direct interaction with the electron spin and does not lead to a perturbation of the atomic electron cloud aligned with the external electric field. A similar argument holds for the tensor coupling. For heavy atoms and molecules, C_S gets enhanced from relativistic contraction of inner electron orbitals. This leads to a higher probability of finding the electron near the nucleus. In contrast, C_P and C_T do not benefit from these effects.

Diamagnetic Atoms

In contrast to paramagnetic systems, diamagnetic atoms are systems in which all electron spins are paired, which is why they are rather insensitive to CP-violating effects arising directly from the electron EDM. The most dominating contribution results from the nuclear Schiff moment. The Schiff moment is a CP-violating electric-dipole charge distribution for a nucleus that results from its finite size, thus breaking the conditions of Schiff's theorem, which states that the net electric field at the nucleus cancels the applied external electric field, rendering the EDM of the atom zero [85]. The CP-violating pion-nucleon interactions are a source of Schiff moments, given in Eq. (3.12). The isoscalar term $\bar{g}^{(0)}_{\pi NN}$ is proportional to $\tilde{d}_u + \tilde{d}_d$. This arises from quark-gluon interactions that affect the up and down quarks symmetrically. The isovector term $\bar{g}^{(1)}_{\pi NN}$ is proportional to $\tilde{d}_u - \tilde{d}_d$ which is due to the isospin asymmetry in the charge distribution. The isotensor coupling arises from higher-order corrections from chiral perturbation theory being suppressed by the difference of the up and down masses. In addition to the pion-nucleon interactions, contributions from the unpaired protons and neutrons to the Schiff moment can also be sizeable. The enhancement factors for the neutron s_n and proton EDMs s_p are nuclear structure-dependent and account for their spatial distributions in the nucleus. The relation of the partonic EDMs to that of the mercury is given by [83]

$$\frac{d_{\text{Hg}}}{e} = \kappa_S \left[g_{\pi NN} \left(\frac{a_0}{e} \bar{g}^{(0)}_{\pi NN} + \frac{a_1}{e} \bar{g}^{(1)}_{\pi NN} \right) + s_n \frac{d_n}{e} + s_p \frac{d_p}{e} \right] + a_e \frac{d_e}{e} \,. \tag{3.15}$$

Here, $\kappa_S = -2.8 \times 10^{-4}\,\text{fm}^{-2}$ denotes the contribution of the Schiff moment to the mercury EDM, with an error not exceeding 20% [86]. The expression in square brackets is the Schiff moment for mercury. The CP-odd isoscalar and isovector pion-nucleon interactions are given by $g^{(0)}_{\pi NN} = (5 \pm 10) \times (\tilde{d}_u + \tilde{d}_d)\,\text{fm}^{-1}$, $g^{(1)}_{\pi NN} = 20^{+40}_{-10} \times (\tilde{d}_u - \tilde{d}_d)\,\text{fm}^{-1}$, obtained from QCD sum-rule estimates [87], while $g_{\pi NN} \simeq 13.5$ [88, 89] is the CP-even pion-nucleon coupling. The contribution of these interactions to the Schiff moment is given by the parameters $a_0 = 0.01\,e\,\text{fm}^3$ and $a_1 = \pm 0.02\,e\,\text{fm}^3$. We take these "best values" from Ref. [83]; they have an intrinsic uncertainty of about an order of magnitude. The contributions of unpaired protons and neutrons to the Schiff moment has been calculated in Ref. [90], with result $s_p = 0.20(2)\,\text{fm}^2$ and $s_n = 1.895(35)\,\text{fm}^2$. Finally, the contribution of the electron EDM is subdominant; no explicit uncertainty is given for the prefactor $a_e = 10^{-2}$ [83, 87]; however, different evaluations lead to different signs [91]. See Ref. [83] for a detailed discussion of all contributions to the mercury EDM. Employing "central values" for all parameters, we find numerically

$$\frac{d_{\text{Hg}}}{e} = -3.8 \times 10^{-4} \left[0.5 \big(\tilde{d}_u + \tilde{d}_d\big) \pm 4 \big(\tilde{d}_u - \tilde{d}_d\big) \right] - 5.3 \times 10^{-4} \frac{d_n}{e} \,, \tag{3.16}$$

with d_n/e given in Eq. (3.17).

We neglect several contributions in Eq. (3.15). The isotensor coupling contributes in principle but is expected to be small in comparison to the scalar and vector coupling, as it arises at higher-order in chiral perturbation theory [83]. Contributions of four-fermion operators are smaller than the chromo-EDM (CEDM) contributions by two orders of magnitude and are also neglected. Finally, in our analysis, we neglect the proton EDM contribution that is one order of magnitude smaller than the neutron EDM contribution, as well as the small electron EDM contribution.

Neutron

The simplest hadronic system used in our fit is the neutron. Throughout this work, we assume that the θ_{QCD} term has a negligible effect on any EDMs and all effects arise from the Yukawa SMEFT operators. The dipole moments of the partons then contribute to the neutron EDM as

$$\frac{d_n}{e} = (1.1 \pm 0.55)(\tilde{d}_d + 0.5\tilde{d}_u) + \left(g_T^u \frac{d_u}{e} + g_T^d \frac{d_d}{e} + g_T^s \frac{d_s}{e}\right) \pm \frac{74}{3}(1 \pm 0.5) w \,\text{MeV}\,. \quad (3.17)$$

The hadronic matrix elements of the CEDMs ($\tilde{d}_q$) and the Weinberg operator (w) are estimated using QCD sum rules and chiral techniques [81, 83, 92]. For the matrix elements of the electric dipole operators (d_q) we use the lattice results $g_T^u = -0.204(15)$, $g_T^d = 0.784(30)$, $g_T^s = -0.0027(16)$ [93]. The sign of the hadronic matrix element of the Weinberg operator is not known; to be definite, we choose the positive sign in our analysis. Note that in our scenario the contribution of the Weinberg operator is always subdominant (either suppressed by small quark masses or numerically small compared to the electron EDM bound), such that the sign ambiguity does not affect the results of our global fit.

3.2.2 Collider Searches

In addition to the low energy scale EDM observables, we consider constraints from collider searches, from the Large Hadron Collider (LHC) in particular. Higgs boson signals are characterised by the production cross-section σ multiplied by the branching ratio BR for a specific decay channel. This determines the expected event rate for a given process. The calculation of a signal depends on the production mechanisms of the Higgs boson. These typically include QCD and electroweak interactions. Theoretical calculations rely on event generators like `MadGraph5` [94] or `POWHEG` [95] which provide matrix elements at higher order accuracy in QCD. See [96–98] for more details. Parton distribution functions such as `NNPDF3.0` [99] are incorporated, which describe the momentum distribution of partons within the proton. The partons undergo parton showering and hadronisation to form stable final-state particles. The former simulates the soft and collinear emissions of gluons and quarks, performed by programs like `Pythia` [100]. Hadronisation converts partons into hadrons, forming jets observable in detectors [101]. To differentiate the production of a Higgs boson from background processes like $t\bar{t}$ production with additional jets, the signal has to be isolated. This is done by programs like `Sherpa` [102]. Accurate signal extraction requires a realistic simulation of the detector response. Tools like `GEANT4` [103] model the interactions of particles with detector material, including energy deposits in calorimeters.

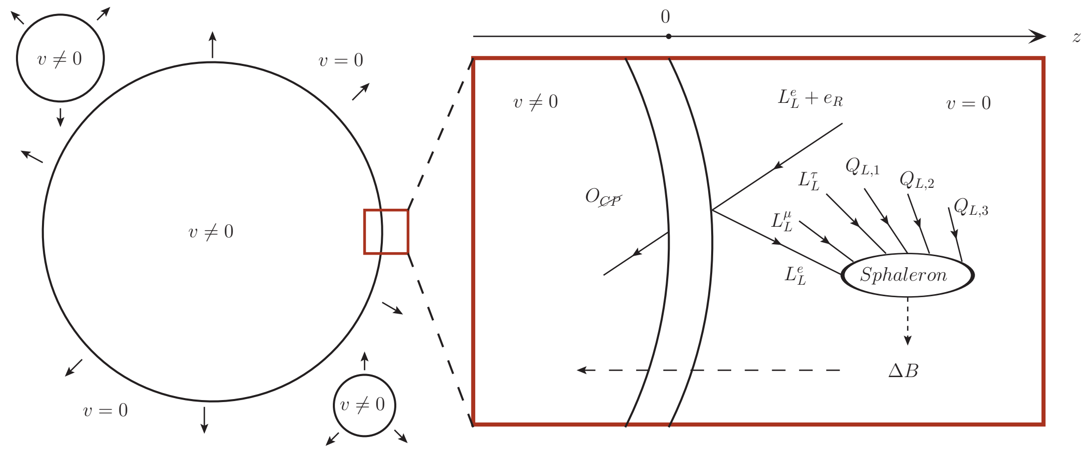

Figure 3.2: Depiction of Electroweak Baryogenesis via the nucleation of bubbles with a broken phase $v \neq 0$. See text for details.

3.2.3 Electroweak Baryogenesis

As a third observable, the baryon asymmetry in the universe (BAU) Y_B is introduced. See [9, 11, 12] for details. One widely considered approach to explain this asymmetry is electroweak baryogenesis (EWBG). Like any approach for BAU, Sakharov's conditions [104] have to be fulfilled simultaneously.

1. In thermal equilibrium, the forward and reverse rates for processes producing baryons are equal. As a result, the baryon number remains constant because any generated BAU would be erased by its reverse process. The departure of the thermal equilibrium introduces irreversibility necessary for BAU to persist.

2. Assuming a state with no BAU after an inflationary phase in the hot universe, it could not have evolved into a state with BAU without active baryon number violating processes. Hence, baryon number conservation must be violated, $\partial_\mu J^\mu_B \neq 0$.

3. To generate a BAU, C and CP invariance has to be broken. If C symmetry was conserved, the production rates for baryons B and antibaryons $\bar{B}$ by some particle X would be identical, leading to no net baryon asymmetry $\Delta B \propto \Gamma(X \to B) - \Gamma(X \to \bar{B})$. If C was broken but CP conserved, the baryon asymmetry generated by X decays would exactly be cancelled by the asymmetry generated by $\bar{X}$ decays.

Fig. 3.2 illustrates the initial stage of the first-order electroweak phase transition (EWPT), which involves the formation of bubbles of the new vacuum $v \neq 0$, a process that occurs out of equilibrium. Inside the bubble with the broken phase, the Higgs field breaks the electroweak symmetry as discussed in Sec. 2.2. When a lepton approaches the bubble wall from the symmetric phase outside, it is partially reflected and transmitted due to CP-violating interactions near the wall. This introduces a bias, resulting in a net difference between the number densities of left-handed and right-handed leptons. The left-handed doublets interact with sphalerons[1], which are non-perturbative transitions between topologically distinct vacua of the $SU(2)$ gauge fields [105]. This interaction is described by the non-conserved baryon number current at the quantum level

$$\partial_\mu J^\mu_B = \partial_\mu \sum_q (\bar{q}_L \gamma^\mu q_L) = \frac{g^2}{(4\pi)^2} \frac{n_f}{2} \mathrm{Tr} W^a_{\mu\nu} \tilde{W}^{a,\mu\nu} \neq 0, \tag{3.18}$$

where $n_f = 3$ is the number of fermion families. The same holds for the lepton current, so that $B - L$ is conserved in the SM, but not $B + L$. These sphaleron transitions change the $SU(2)$ vacuum, which is related to the baryon number violation as

$$\Delta B = n_f \Delta N_{CS}, \tag{3.19}$$

where N_{CS} is the spatial integral over the time component of the Chern-Simons current K^μ, see Eq. (2.62). Depending on the CP violating phases, the net asymmetry in left-handed lepton densities creates a preferential production of baryons over antibaryons proportional to the bias in the chiral density, which is determined by the transport equations for the diffusion and interactions in front of the bubble wall

$$\partial_t n_L - D\nabla^2 n_L = -\Gamma n_L + S_{CP}, \tag{3.20}$$

with the left-handed lepton density n_L, the diffusion constant D, the interaction rate Γ and the CP violating source term S_{CP} at the bubble wall. Due to the expansion of the bubble, the baryon number produced in the symmetric phase is swept up into the broken phase. Inside the broken phase, the energy required for the sphaleron transitions is of order $E_{\text{sph}} \approx 8\pi v/g$ and its rate,

$$\Gamma_{\text{sph}} = T^4 \exp\left(-\frac{E_{\text{sph}}}{T}\right), \tag{3.21}$$

is strongly suppressed compared to the Hubble rate. This suppression is necessary to prevent the washout of the generated BAU.

The SM fails to meet all of Sakharov's conditions sufficiently. The departure of the thermal equilibrium can be achieved through a first-order phase transition. However, for the observed Higgs boson mass $m_h \approx 125$ GeV, a smooth, continuous transition between the symmetric and the broken phase is predicted at the critical temperature. The thermal barrier between the vacua

[1]From the ancient Greek word "$\sigma\varphi\alpha\lambda\epsilon\rho\acute{o}\varsigma$" translated as "likely to make a stumble", maybe due to its geometrical interpretation as a saddle point of the electroweak potential.

is defined by the cubic term in the finite-temperature effective potential [106] $V_{\text{eff}}(H, T) \supset -ET\phi^3$ with E representing contributions from the electroweak gauge bosons and ϕ the radial part of the Higgs field, proportional to $\sqrt{H^\dagger H}$. This term, however, is too small to create a barrier [106]. SMEFT introduces operators such as $(H^\dagger H)^3$ enhancing it, see Eq. (3.2). The only source of CP violation in the SM is the complex phase in the CKM matrix. While the phase itself is maximal, its contribution to physical CP violating observables is highly suppressed due to the hierarchy of the quark masses, quantified by the Jarlskog invariant of $J_{\text{CKM}} \sim 10^{-5}$ [107]. The chiral asymmetry $\Delta n_L \propto J_{\text{CKM}}$ yielding a BAU generated by SM CP violation, estimated to be ten orders of magnitude [108] smaller than the observed value [7]

$$\eta_B = \frac{n_B}{s} \sim 10^{-10}, \tag{3.22}$$

with the entropy density s. SMEFT introduces new Yukawa operators (Eq. (3.3)) that can generate additional CP-asymmetry at the bubble walls. In contrast, no new physics contributions are required to satisfy the condition of baryon number violation since the sphaleron transitions are already efficient in front of the bubble wall and inefficient behind it.

Although EWBG may yield considerable constraints on CP-violating WCs, we do not include it in our analyses because we do not want to make specific assumptions on the dynamics of the EWBG. That includes additions to the Higgs potential to achieve sufficient first-order EWPT, specifying the transport equations and the bubble wall properties. See [109–112] where EWBG is included in the analyses.

3.3 Global Analysis and Statistics

When constructing a model with a set of parameters $\{\theta\}$, which predicts a set of observables $\{O_i^{\text{pred}}\}$, its validity is assessed by comparison to experimental measurements $\{O_i^{\text{exp}}\}$. The index i represents a the different observables. In a global analysis, the model parameter space Θ, spanned by $\{\theta\}$, is explored to identify regions that maximise the likelihood function, i.e., minimise the negative log-likelihood function [113, 114]

$$-\log L(\theta) = \sum_i \frac{O_i^{\text{pred}}(\theta) - O_i^{\text{exp}}}{2\sigma_i^2} = \frac{\chi^2}{2}, \tag{3.23}$$

with the standard deviation σ and the χ^2-value. There is a multitude of sampling procedures to scan the parameter space, like grid scanning, where the parameters are varied with regular incremental steps within defined bounds, and stochastic methods. This sampling results in a configuration of θ that results in the smallest log-likelihood value $L_{\text{best}} := \sup_{\theta\in\Theta} L(\theta)$. All other configurations can be normalised to it as the likelihood ratio

$$\lambda_{\text{LR}} := \exp \Delta \log L = \exp(-\log L_{\text{best}} + \log L), \tag{3.24}$$

which lies between 0 and 1. To assess the statistical significance of a parameter configuration, the p-value is defined and related to χ^2 and the degrees of freedom ν as

$$p(\chi_b^2, \nu) = 1 - \int\limits_0^{\chi_b^2} \chi^2(x, \nu)\, \mathrm{d}x, \tag{3.25}$$

with the χ_b^2 being the boundary value for a confidence limit b and the χ^2 probability density function

$$\chi^2(x, \nu) = \frac{1}{2^{\nu/2}\Gamma\left(\frac{\nu}{2}\right)} x^{\nu/2-1} \mathrm{e}^{-x/2}, \quad x \in \mathbb{R}^+. \tag{3.26}$$

To examine the significance of the parameter configurations, a set of relevant parameters is fixed, while the remainder is profiled such that the likelihood ratio gets maximised. For display reasons, usually one or two parameters are kept free. The boundary χ_b^2 then is related to the p-value for one or two degrees of freedom as

$$p(\chi_b^2, 1) = 1 - \text{Erf}\left(\sqrt{\frac{\chi_b^2}{2}}\right), \qquad p(\chi_b^2, 2) = \mathrm{e}^{-\chi_b^2/2}, \tag{3.27}$$

which results in $\chi^2_{68\%} \approx 0.99\,(2.28)$ and $\chi^2_{95\%} \approx 3.84\,(5.99)$ for $\nu = 1\,(2)$. These values denote the differences between the best fit value and a point in parameter space for which the significance level is reached. The likelihood ratios corresponding to these boundary values for $\nu = 2$ are then calculated as

$$\lambda_{\text{LR},b} = \exp\left(-\frac{\chi_b^2}{2}\right). \tag{3.28}$$

In general, they can be calculated as [115]

$$\lambda_{\text{LR},b} = \exp\left(P^{-1}\left(\frac{\nu}{2}, p\right)\right) \tag{3.29}$$

with the inverse to the regularised lower incomplete gamma function

$$P(a, x) = \frac{1}{\Gamma(a)} \int\limits_0^x t^{a-1} \mathrm{e}^{-t}\, \mathrm{d}t. \tag{3.30}$$

Model parameter configurations within these likelihood ratio bounds are not considered to result in the rejection of the null hypothesis at the given confidence level.

Chapter 4

CP Violating Light Quark Yukawas in The κ Framework

We turn to the exploration of one of two frameworks where CP violation is introduced into the Higgs-Yukawa coupling of the electrically charged SM fermions. This first approach considers a simple modification by adding a CP-violating phase, which is often referred to as the κ-framework, where the interaction is parameterised by a CP-conserving part κ and a CP-violating part $\tilde{\kappa}$. A CP-violation in the top Yukawa coupling is a key driver of electroweak baryogenesis (EWBG) in many models. However, as discussed in Sec. 3.2.1, such phases also induce electric dipole moments (EDMs) in various elementary particles and hadronic systems that impose stringent constraints on these phases, often excluding numerous EWBG models. As pointed out in Ref. [116], while phases in the top Yukawa are the most relevant for EWBG, phases in other Yukawa couplings can substantially influence EDM constraints. This motivates a detailed study of CP-violating contributions to <u>all</u> Yukawa couplings. Previous studies have concentrated on the electron [117] and third-generation fermions [14, 118]. Here, we focus on the light-quark Yukawa couplings - specifically, those of the up, down, and strange quarks. Constraints on these couplings were studied in Ref. [119] in the context of effective dimension-six Higgs–quark interactions. In this chapter, we provide a comprehensive calculation of the full set of contributing two-loop diagrams induced by CP-violating phases in the light-quark Yukawas. Notably, our results reveal that bosonic contributions dominate over those from top-loops.

We start by motivating and outlining the model with our choice of an operator basis, focusing on CPV phases in the couplings with $\{u, d, s\}$ in Sec. 4.1. Afterwards, we go through the method of calculating the initial expressions for these operators at the scale of electroweak interactions in Sec. 4.2 and present the results in Feynman gauge in Sec. 4.3. Up to here, the content is mainly based on our publication [120]. Finally, we conclude with the implications of choosing such a gauge in Sec. 4.4.

4.1 Model and Operator Basis for Light Quarks

In Sec. 3.2.3 we saw that baryogenesis requires CP-violation and in Sec. 2.2 we discussed its sources within the SM. These alone fall short by orders of magnitude to satisfy the requirements for EWBG as their leading contribution is a loop process and thus highly suppressed. Also, the EDM experiments are not sensitive enough, as their upper limits range orders of magnitude above the SM predictions.

As pointed out in Ref. [116] the light fermion contributions to EWBG are small compared to the one of the top quark. But as several EDMs constrain the phase in the top Yukawa, the inclusion of more phases in the light Yukawa couplings substantially lifts these bounds. EDM constraints on the electron Yukawa were studied in Ref. [117]. In this work we are interested in constraining the phases of the light-quark Yukawas, $q = u, d, s$, via their contributions to hadronic EDMs. In Sec. 3.2.1 we gave their expressions and their relations with the partonic EDMs induced by the low-energy effective Lagrangian [83] valid at energy scales of the order of $\mu_{\text{had}} = 2$ GeV which we repeat here

$$\mathcal{L}_{\text{eff}} = -d_q \, \frac{i}{2} \, \bar{q}\sigma^{\mu\nu}\gamma_5 q \, F_{\mu\nu} - \tilde{d}_q \, \frac{ig_s}{2} \, \bar{q}\sigma^{\mu\nu}T^a\gamma_5 q \, G^a_{\mu\nu} \,, \tag{4.1}$$

We calculate the contributions to this Lagrangian induced by the modified Yukawa couplings in Eq. (3.1) by first matching the modified SM to the effective Lagrangian,

$$\mathcal{L}_{\text{eff}} = -\sqrt{2}G_F \sum_q C^q_k O^q_k + \dots \,, \tag{4.2}$$

obtained by integrating out the heavy gauge bosons, the top quark, and the Higgs boson at the weak scale $\mu_{\text{ew}} \sim M_h = 125.18\,\text{GeV}$. Here, the sum runs over all active quark fields below the weak scale ($q = u, d, s, c, b$), G_F is the Fermi constant and the operators are defined as

$$O^q_1 = \frac{ieQ_q}{2} \, m_q \, \bar{q}\sigma^{\mu\nu}\gamma_5 q \, F_{\mu\nu} \,, \qquad O^q_2 = -\frac{i}{2} \, g_s \, m_q \, \bar{q}\sigma^{\mu\nu}\gamma_5 T^a q \, G^a_{\mu\nu} \,. \tag{4.3}$$

There are many more effective operators being generated by the matching procedure, such as CP-violating four-fermion operators. But for the hadronic EDMs their contribution, if any, is small compared to the ones expressed here. So they are denoted by the ellipsis in Eq. (5.11).

Apart from the four-fermion operators, a noteworthy example is the Weinberg operator (WBO) [121]

$$O_3 = -\frac{1}{3\,g_s} f^{abc} \, G^a_{\mu\sigma} G^{b,\sigma}_{\nu} \widetilde{G}^{c,\mu\nu} \tag{4.4}$$

that also receives a contribution from modified quark couplings (see Fig. 4.1). However, as

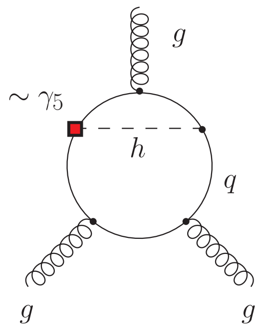

Figure 4.1: The contributions to the Weinberg operator are suppressed with respect to the dipole contributions by an additional power of a light-quark Yukawa and are neglected. Here and in the following, the CP-violating Higgs coupling ($\sim \gamma_5$) to the light quarks $q = u, d, s$ is denoted by a red square.

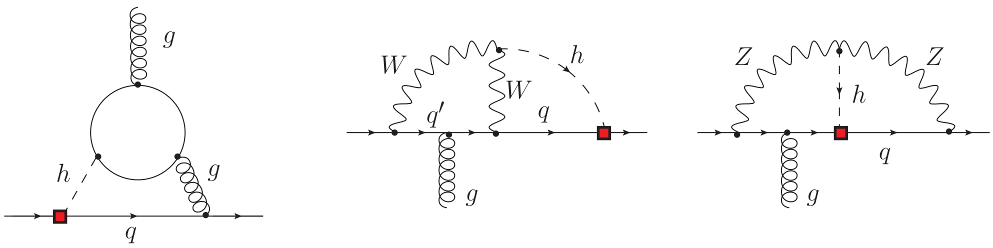

Figure 4.2: Sample two-loop Feynman diagrams inducing a chromoelectric dipole moment for the light quark $q = u, d, s$ through a CP-violating Higgs-Yukawa coupling. Six diagrams exist for the top-loop Barr-Zee (*left*), four for the W-kite (*middle*) and six for the Z-kite (*right*) The label q' denotes a quark with opposite weak isospin with respect to q.

we are only interested in the light-quark Yukawa couplings here, its contributions are further suppressed by an additional factor of a small Yukawa coupling, so that the WBO is also small with respect to the dipole operators (Eq. (4.3)). Furthermore, the dipole operators do not mix into the Weinberg operator, hence, it plays no role in our calculation.

We perform the matching at the weak scale by calculating appropriate off-shell Green's functions with light external quarks, photons, and gluons. As pointed out in Ref. [122], the leading contributions arise from two-loop diagrams in the modified SM (see Fig. 4.2-4.4). In order to project all our results, we need to include one unphysical operator that vanishes by the equations of motion (e.o.m.) of the light-quark fields. It can be chosen as

$$N_1^q = m_q \, \overline{q} \not{D} \not{D} i\gamma_5 q \,, \tag{4.5}$$

where the covariant derivative acting on quarks is defined as

$$D_\mu \equiv \partial_\mu - i g_s T^a G^a_\mu + ie Q_q A_\mu \,, \tag{4.6}$$

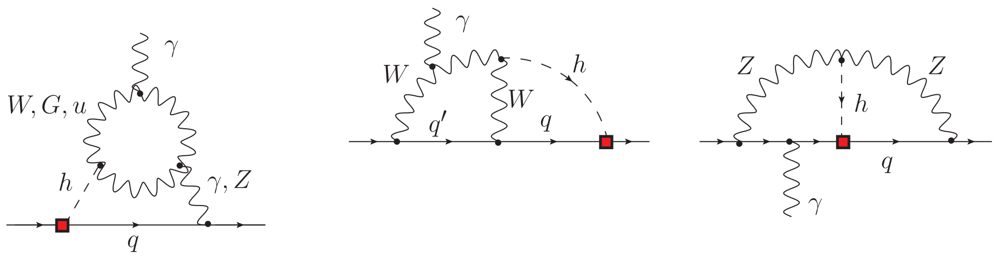

Figure 4.3: Sample two-loop Feynman diagrams inducing an electric dipole moment for the light quark $q = u, d, s$. The loop in the Barr-Zee (*left*) is depicted with a vector boson line, however, it can be swapped for one containing a Goldstone boson or a Fadeev-Popov ghost. There are 32 diagrams with a loop related to the weak gauge bosons. *Middle*: The photon can couple to the isospin partner of the external quark, giving rise to two additional diagrams compared to the leptonic case, six in total. For the Z-kite topology (*right*) the situation is identical to the former gluonic case.

with the quark electric charge Q_q. The corresponding effective Feynman rule for the interaction with an external photon is derived as described in Sec. 2.4 to

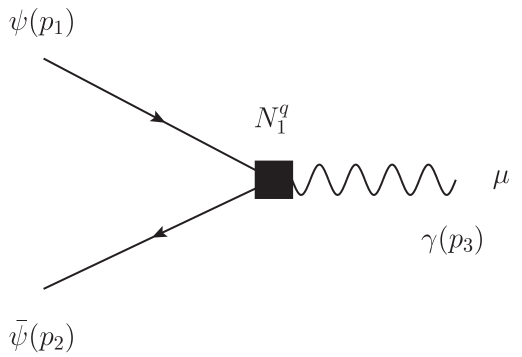

$$\sim \qquad ieQ_f \left(\not{p}_3 \gamma^\mu + 2p_1^\mu \right) \gamma_5 . \tag{4.7}$$

Many contributions to the initial conditions can be obtained, in principle, by rescaling the results for the electron EDM [117] (see also Ref. [123]). There are, however, new diagrams that appear only in the case of light-quark EDMs, since the photon does not couple to the neutrino in the case of the contributions to the electron EDM (see Fig. 4.3, middle panel). Note that the set of additional "non-Barr–Zee" diagrams with an internal top-quark line (see Fig. 4.4, right panel) are suppressed by the CKM factor $|V_{td}|^2 \approx 7 \times 10^{-5}$ and are neglected in our calculation. The corresponding diagrams with external strange quarks are suppressed by $|V_{ts}|^2 \approx 1.5 \times 10^{-3}$ and are also neglected.

In order to display our analytic results, we decompose the Wilson coefficients (WCs) as

$$\begin{aligned} C_1^q &= C_1^{q,t\gamma} + C_1^{q,tZ} + C_1^{q,W\gamma} + C_1^{q,WZ} + C_1^{q,W} + C_1^{q,Z} \,, \\ C_2^q &= C_2^{q,tg} + C_2^{q,W} + C_2^{q,Z} \,. \end{aligned} \tag{4.8}$$

The terms labelled by $t\gamma$, tZ, and tg denote the contributions from Barr–Zee-type diagrams

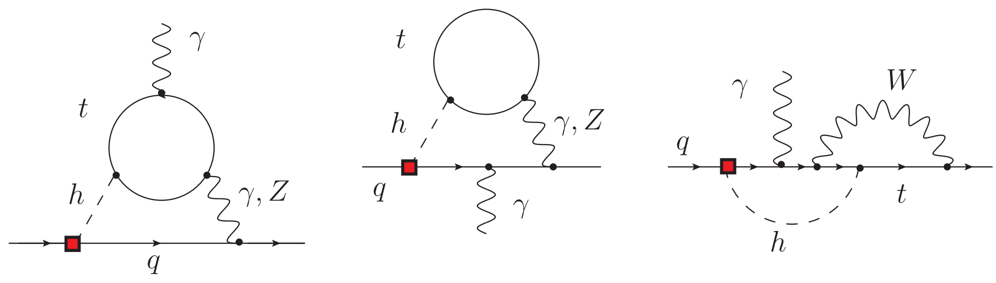

Figure 4.4: Sample two-loop Feynman diagrams with internal top quarks, inducing an electric dipole moment for the light quark $q = u, d, s$. Left panel: The classic "Barr–Zee" diagrams. The diagrams with an internal Z boson give a substantial contribution for external down quarks. The sum of diagrams of the form shown in the middle panel vanishes (the same is true for the corresponding bosonic diagrams). Right panel: This class of diagrams with an internal top-quark line is parametrically suppressed by small CKM matrix elements and has been neglected in our calculation.

containing top-quark loops and an internal photon, Z boson, or gluon, respectively (see Fig. 4.2 and Fig. 4.4, left panels); the terms labelled by $W\gamma$ and WZ denote corresponding bosonic diagrams (see Fig. 4.3, left panel). The terms labelled W and Z denote "non-Barr–Zee" type diagrams with internal W or Z bosons, respectively (see Fig. 4.2 and Fig. 4.3, middle and right panels).

4.2 Method of Calculation

The calculation of the WCs is illustrated using one generic three-point Feynman diagram with an open fermion line and an external photon. The LO amplitude for a light quark flavour $f \in \{u, d, s\}$ can be expressed as

$$A^{(0)} = K \int \frac{\mathrm{d}^d q_1}{(2\pi)^d} \int \frac{\mathrm{d}^d q_2}{(2\pi)^d} \overline{\psi}_f(p_2) \Gamma \psi_f(p_1) \frac{\mathrm{Tr}(T_{\mathrm{D}})}{D} \Pi \epsilon^*_\mu(p_3) \tag{4.9}$$

where we introduce

- the prefactor K containing all remaining numerical constants,
- the external momenta p_1, p_2 and $p_3 = p_1 - p_2$,
- the Dirac-structure of the open light fermion line Γ containing exactly one modified Yukawa coupling,
- the numerators of the vector propagators Π in Feynman-gauge ($\xi = 1$),
- the trace of the Dirac tensor T_{D} if a fermion loop is present in the diagram,

- the denominator D, which is the product of the denominators of the internal particle propagators in the diagram and
- the polarisation vector of the outgoing photon or gluon contracted with the appropriate Lorentz tensor.

Simplifications

The amplitude is evaluated by expanding Eq. (4.9) in the external momenta around zero. Light quark masses are set to zero. This is valid in our case since we do not find infrared divergences. In the general case, an artificial mass m_{IRA} is introduced in an approach called infrared rearrangement to recursively decompose propagators of potentially vanishing mass [124]. This mass regularises spurious infrared divergences and has to vanish in the final expression as the decomposition is exact. The first-order expansion in the external momenta is sufficient for matching onto the (C)EDM operator $O^f_{1,2}$ (Eq. (5.18)) and the unphysical operator N^q_1. An expansion up to third order is required to match onto the Weinberg operator O_3. The Taylor expansion to some power n for the propagators can be expressed as

$$\left.\frac{1}{(p+q)^2-m^2}\right|_{p=0} \approx \frac{1}{q^2-m^2}\sum_{k=0}^{n}\left(-\frac{2p_\mu q^\mu + p^2}{q^2-m^2}\right)^k, \tag{4.10}$$

where terms of higher order than n in the external momenta are discarded.
Evaluating the Dirac trace in d dimensions takes some special treatment, particularly when an odd number of γ_5 is present (see Sec. 2.3). This situation arises if we impose a CP-violating top-Yukawa, i.e., $\phi_t \neq 0, \pi$. In the LO analysis, the considered Feynman diagrams contain fermion loops with one vector, one scalar, and one (axial-)vector coupling. Hence, the Dirac structure in the trace is not rich enough to yield traces beyond those calculable using the standard $d = 4$ results. Without γ_5, the traces can be computed easily using the Clifford algebra (Eq. (2.8)) recursively.
From the expansion in the external momenta and the vector boson propagators, the internal momenta generate a tensor structure that can be expressed as

$$T^{a_1 a_2 \ldots a_l} := \prod_{k=1}^{l}\int \mathrm{d}^d q_k \prod_{m=1}^{a_k} q_k^{\mu_{k,m}} \tag{4.11}$$

where a_k labels the power of the internal momenta q_k. By exploiting Lorentz invariance, the momentum integrals can be reduced to combinations of the Minkowski metric and Lorentz scalars built of the momenta [125]. This leads to

$$T^{a_1 a_2 \ldots a_l} = \sum_{k}^{s_p} A_k \eta^{(\nu_1\nu_2} \cdots \eta^{\nu_{2r-1}\nu_{2r})}, \tag{4.12}$$

where the sum runs over all even, non-identical permutations of the metric tensors signified by the parentheses in the exponent. Here, $s_p = {}^{(2r)!}/_{r!\,2^r}$ counts the number of permutations with $r = {}^1/_2 \sum_k^l a_k$. Only an even amount of internal momenta yields non-trivial results. If r is odd, the integral vanishes due to the odd nature of the integrand. The A_k are functions of Lorentz scalars depending only on the internal momenta. To determine the coefficients A_k, the tensor T in Eqs. (4.11) and (4.12) is contracted with s_p permutations, yielding a matrix equation $I_m = M_{mk} \cdot A_k$, where I_m are scalar products of the internal momenta, some of which may be identical due to the symmetries in the tensor indices. The elements of the matrix M are monomials in d and the functions A are obtained by inverting this matrix. The easiest non-trivial example is

$$T^{20} = \int \mathrm{d}^d q_1 q_1^\mu q_1^\nu = A_1 \eta^{\mu\nu}. \tag{4.13}$$

Contracting with the Minkowski metric yields

$$A_1 = \frac{1}{d} \int \mathrm{d}^d q_1 q_1^2. \tag{4.14}$$

A slightly more complex example is

$$T^{22} = \int \mathrm{d}^d q_1 \, \mathrm{d}^d q_2 q_1^\mu q_1^\nu q_2^\rho q_2^\sigma = A_1 \eta^{\mu\nu}\eta^{\rho\sigma} + A_2 \eta^{\mu\rho}\eta^{\nu\sigma} + A_3 \eta^{\mu\sigma}\eta^{\rho\nu}. \tag{4.15}$$

Contracting both sides, each with the permutations of $\eta^{(\mu\nu}\eta^{\rho\sigma)}$ gives

$$\begin{pmatrix} I_1 \\ I_2 \end{pmatrix} = \begin{pmatrix} d^2 & 2d \\ d & d^2 + d \end{pmatrix} \begin{pmatrix} A_1 \\ A_2 \end{pmatrix}, \tag{4.16}$$

where $I_1 = q_1^2 q_2^2$ and $I_2 = I_3 = (p_1 p_2)^2$. Using $\eta^{\mu\nu}\eta_{\mu\nu} = d$ the coefficients A_1 and $A_2 = A_3$ are expressed by inserting the matrix as

$$A_1 = \frac{I_1(1+d) - 2I_2}{d(d^2+d-2)} \qquad\qquad A_2 = \frac{-I_1 + dI_2}{d(d^2+d-2)}. \tag{4.17}$$

For tensors with higher values of r, the inversion of M becomes more complicated. To simplify calculations, we set $d = 4 - 2\epsilon$ and expand the matrix in ϵ to the required order.

In the next step, the Lorentz scalars I_k in the numerator are eliminated by systematically cancelling the scalar products with the denominators. This reduction is achieved at the 2-loop order through identities such as

$$\frac{q_k^2}{D_k} = 1 + \frac{m_k^2}{D_k} \qquad \text{and} \qquad \frac{2q_{k_a} q_{k_b}}{D_{k_a,k_b}} = -1 + \frac{q_{k_a}^2 + q_{k_b}^2 + m_{k_a,k_b}^2}{D_{k_a,k_b}}, \tag{4.18}$$

with $D_k = q_k^2 - m_k^2$, $D_{k_a,k_b} = (q_{k_a} - q_{k_b})^2 - m_{k_a,k_b}^2$ and m representing generic particle masses. Through this procedure, terms without D_{k_a,k_b} can be present, splitting up the integral into 2 one-loop integrals. If any D_k is missing but an appropriate D_{k,k_a} is present, a shift such as $q_{k_a} \to q_{k_a} - q_k$ can be applied, converting D_{k,k_a} into a term involving D_k with the mass of the former. If no suitable denominator exists to facilitate this shift, the integral over q_k vanishes as a scaleless integral. Terms involving odd powers of $(q_{k_1} q_{k_2})$ are odd under the integration and vanish. For even powers, the two-dimensional integral becomes two one-dimensional ones

$$\int \mathrm{d}^d q_{k_1}\, \mathrm{d}^d q_{k_2} (q_{k_1} q_{k_2})^{2n} = \frac{(2n)!}{4^n n! (d/2)_n} \int \mathrm{d}^d q_{k_1} (q_{k_1}^2)^n \int \mathrm{d}^d q_{k_2} (q_{k_2}^2)^n \tag{4.19}$$

with the Pochhammer symbol $(a)_n := \Gamma(a+n)/\Gamma(a)$. These steps are repeated until no internal momenta q_k are left in the numerator. Additionally, products of propagators with distinct masses are separated using the partial fraction decomposition

$$\frac{1}{q^2 - m_1^2} \frac{1}{q^2 - m_2^2} = \frac{1}{m_1^2 - m_2^2} \left(\frac{1}{q^2 - m_1^2} - \frac{1}{q^2 - m_2^2} \right), \tag{4.20}$$

reducing the power of momenta in the denominator per term.

Evaluation

Following through with these steps, we arrive at the main two-loop integral

$$I(a_1, a_2, a_3, m_1, m_2, m_3) = \int \frac{\mathrm{d}^d q_1\, \mathrm{d}^d q_2}{(q_1^2 - m_1^2)^{a_1} (q_1^2 - m_2^2)^{a_2} [(q_1 - q_2)^2 - m_3^2]^{a_3}}. \tag{4.21}$$

For specific cases such as $m_1 = m_2 = m$ and $m_3 = 0$ or $m_2 = m_3 = 0$, closed-form solutions can be given directly via Feynman parameterisation

$$I(a_1, a_2, a_3, m, m, 0) = C \frac{(2-\epsilon)_{-a_3} (1+\epsilon)_{n_1+n_3-3} (1+\epsilon)_{n_2+n_3-3}}{(n_1-1)!(n_2-1)!(n_1+n_2+n_3-4+2\epsilon)_{n_3}} \tag{4.22}$$

$$I(a_1, a_2, a_3, m, 0, 0) = C \frac{(1+2\epsilon)_{n_1+n_2+n_3-5} (1+\epsilon)_{n_2+n_3-3} (1-\epsilon)_{1-n_2} (1-\epsilon)_{1-n_3}}{(n_1-1)!(n_2-1)!(n_3-1)!(1-\epsilon)(1 - {}^{1}\!/_{3}\pi^2 \epsilon^2 + \mathcal{O}(\epsilon^2)} \tag{4.23}$$

with the prefactor $C = (-1)^{a_1+a_2+a_3+1} m^{4-2\epsilon-a_1-a_2-a_3} \pi^{4-2\epsilon} \Gamma^2(1+\epsilon)$. For the cases of non-vanishing $m_1 \neq m_2$ and $m_3 = 0$ or with no vanishing masses, recurrence relations are derived, reducing the general two-loop integral in Eq. (4.21) into the form of $I(1,1,1,m_1,m_2,m_3)$ [126, 127]. Two frequently occurring cases are

$$\begin{aligned} I(1,1,1,m,m,M) = &\frac{A}{(1-\epsilon)(1-2\epsilon)} \\ &\times \left(-\frac{1}{\epsilon^2}(1+2z) + \frac{1}{\epsilon}(4z \log(4z)) - 2z \log^2(4z) + 2(1-z)\Phi(z) \right), \end{aligned} \tag{4.24}$$

where $m_1 = m_2 = m \neq M = m_3$ and $z = M^2/(4m^2)$ and

$$\begin{aligned} I(1,1,1,m_1,m_2,0) &= \frac{1}{2(1-\epsilon)(1-2\epsilon)} \\ &\times \left(-\frac{1+x}{\epsilon^2} + \frac{2}{\epsilon} x \log x + (1-2x)\log^2 x + 2(1-x)\mathrm{Li}_2\left(1-\frac{1}{x}\right)\right) + \mathcal{O}(\epsilon), \end{aligned} \tag{4.25}$$

with $x = m_2^2/m_1^2$. Further for $z < 1$,

$$\begin{aligned} \Phi(z) &= 4\big(\frac{z}{1-z}\big)^{1/2}\mathrm{Cl}_2\big(2\arcsin(z^{1/2})\big)\,, \\ \mathrm{Cl}_2(\theta) &= -\int_0^\theta dx \log|2\sin(x/2)|\,. \end{aligned} \tag{4.26}$$

From $0 < 2\arcsin(z^{1/2}) < \pi$ follows $2\sin(x/2) > 0$ for the considered values. So, the modulus in the integrand of Clausens function Cl_2 is trivial. Up to second order around $z = 0$ it can be approximated by

$$\mathrm{Cl}_2(\theta) \approx \int_0^\theta \frac{x^2}{24} - \log x \;\mathrm{d}x = \frac{\theta^3}{72} + \theta(1-\log\theta) \tag{4.27}$$

with a small error at the percent level at most. For $z > 1$, $\Phi(z)$ takes the form

$$\begin{aligned} \Phi(z) &= \big(\frac{z}{z-1}\big)^{1/2}\big\{ -4\mathrm{Li}_2(\xi) + 2\log^2\xi - \log^2(4z) + \frac{\pi^2}{3}\big\}\,, \\ \xi &= \frac{1-\big(\frac{z-1}{z}\big)^{1/2}}{2}\,, \end{aligned} \tag{4.28}$$

where $\mathrm{Li}_2(x) = -\int_0^x du\; \ln(1-u)/u$ is the dilogarithm. These two-loop calculations involve divergences up to $1/\epsilon^2$. While the final expressions only contain divergences to this order, intermediate steps may yield terms of $1/\epsilon^3$, encountered when the Gamma functions in the numerator and the denominator are expanded successively. This is the case for $m_1 = m_2$, $m_3 = 0$ and $a_1 = a_2 = a_3 = 1$ (see Eq. (4.22)). Therefore, the Taylor series in ϵ must be expanded to at least $\mathcal{O}(\epsilon^3)$.

Matching

This amplitude in the full theory is now matched onto the effective theory operators. Since it represents the leading order contribution, all poles in ϵ, arising from dimensional regularisation, must cancel in the final expression. Any remaining divergences would signal incomplete renormalisation or inconsistencies in the effective field theory. The matched amplitude depends on the external momenta and takes the general form

$$A^{(0)} = \left(A_1\, \not{p}_3 \gamma^\mu + A_2\, p_1^\mu + A_3\, p_3^\mu\right) \gamma_5 \epsilon^*_\mu, \tag{4.29}$$

where the A_i are coefficients determined by the steps outlined in this section. The Feynman rules for the (C)EDM and the EOM operators are given in Eqs. (5.18) and (4.7), respectively. These provide the EFT structures against which the full-theory amplitude is matched. This yields the relations $C^q_{1,2} = A_1 - A_2/2$ and $C_N = a_2/2$. Terms proportional to structures other than those corresponding to the effective operators should not remain after matching. If such terms persist, it indicates that the current operator basis is insufficient and must be extended.

4.3 Results

By explicit calculation, we find

$$\begin{aligned} C_1^{q,t\gamma} = \frac{\alpha}{12\pi^3}\, \kappa_q\, \kappa_t \Big\{ \sin(\phi_q)\cos(\phi_t)\, x_{th} \left[(2x_{th}-1)\,\Phi\left(\frac{1}{4x_{th}}\right) - 2\,(2+\log x_{th})\right] \\ - \cos(\phi_q)\sin(\phi_t)\, x_{th} \Phi\left(\frac{1}{4x_{th}}\right) \Big\}\,, \end{aligned} \tag{4.30}$$

where $x_{th} \equiv m_t^2/M_h^2$. There are contributions from six diagrams in total. For the top-loop diagrams with internal Z bosons we obtain[1]

$$\begin{aligned} C_1^{q,tZ} &= \frac{\alpha}{384 Q_q \pi^3 s_w^2 c_w^2} \kappa_q \kappa_t \left(8s_w^2 - 3\right)\left(4Q_q s_w^2 \mp 1\right) \frac{x_{th} x_{tZ}}{x_{th} - x_{tZ}} \\ &\times \Big\{ \sin(\phi_q)\cos(\phi_t) \big[(1-2x_{th})\,\Phi\left(\frac{1}{4x_{th}}\right) \\ &\qquad - 2\log x_{hZ} - (1-2x_{tZ})\,\Phi\left(\frac{1}{4x_{tZ}}\right) \big] \\ &+ \cos(\phi_q)\sin(\phi_t) \big[\Phi\left(\frac{1}{4x_{th}}\right) - \Phi\left(\frac{1}{4x_{tZ}}\right) \big] \Big\}\,, \end{aligned} \tag{4.31}$$

where $x_{tZ} \equiv m_t^2/M_Z^2$ and $x_{hZ} \equiv M_h^2/M_Z^2$. Here and in the following, the upper sign corresponds to the up quark ($q = u$) and the lower sign to the down-type quarks ($q = d, s$). Moreover, in the remainder of this chapter, we assume the SM values $\kappa_t = 1$ and $\phi_t = 0$ for the top-quark couplings. The corresponding diagrams with gluons instead of photons (see Fig. 4.2, left panel)

[1] Note that, in the case of top-quark CP violation, the off-shell Green's function is finite only after inclusion of an appropriate counterterm to cancel the divergence in the one-loop mixing of the Higgs and the Z boson. The divergent part of the amplitude projects entirely on the e.o.m.-vanishing operator (4.5), so that the physical WC $C_1^{q,tZ}$ is still renormalisation-scheme independent.

give a contribution to the initial condition of the chromoelectric dipole operator; we find

$$\begin{aligned} C_2^{q,tg} = \frac{\alpha_s}{32\pi^3}\,\kappa_q\,\kappa_t\Big\{ \sin(\phi_q)\cos(\phi_t)\,x_{th}\left[(2x_{th}-1)\,\Phi\left(\frac{1}{4x_{th}}\right)-2\,(2+\log x_{th})\right] \\ -\cos(\phi_q)\sin(\phi_t)\,x_{th}\Phi\left(\frac{1}{4x_{th}}\right)\Big\}\,. \end{aligned} \tag{4.32}$$

For the bosonic Barr–Zee-type diagrams, we find

$$\begin{aligned} C_1^{q,W\gamma} =& \frac{\alpha}{64\pi^3}\,\kappa_q\sin(\phi_q)\big[\,(1+6x_{Wh})\,(2+\log x_{Wh}) \\ &+(7-6x_{Wh})\,x_{Wh}\Phi\left(\frac{1}{4x_{Wh}}\right)\big]\,, \end{aligned} \tag{4.33}$$

where $x_{Wh}\equiv M_W^2/M_h^2$, and

$$\begin{aligned} C_1^{q,WZ} =& -\frac{\alpha}{512\pi^3 s_w^2}\,\kappa_q\sin(\phi_q)(x_{Zh}-1)^{-1}\big(4s_w^2\mp\frac{1}{Q_q}\big) \\ &\times\big[\big[3-2x_{Wh}+2c_w^2(6x_{Wh}-7)\big]x_{Zh}\Phi\left(\frac{1}{4x_{Wh}}\right) \\ &+\big[1+18x_{Wh}-2c_w^2(1+6x_{Wh})-4x_{Zh}\big]\Phi\left(\frac{1}{4c_w^2}\right) \\ &+\big(\frac{1}{c_w^2}+2x_{Zh}-2(1+6x_{Wh})\big)\log x_{Zh}\big]\,, \end{aligned} \tag{4.34}$$

where $x_{Zh}\equiv M_Z^2/M_h^2$. The contributions to the electric and chromoelectric dipoles of diagrams with internal Z bosons are equal; we find

$$\begin{aligned} C_1^{q,Z} = C_2^{q,Z} =& \frac{\alpha}{9216\pi^3 s_w^2 c_w^2}\,\kappa_q\sin(\phi_q)x_{Zh}^2\big[2\big(1\mp 4Q_q s_w^2+8Q_q^2 s_w^4\big) \\ &\times\big(24x_{hZ}-6x_{hZ}^2-\big(4+3x_{hZ}\big)\pi^2 \\ &+\big(24x_{hZ}+6x_{hZ}^2-3x_{hZ}^3\big)\Phi\left(\frac{x_{hZ}}{4}\right) \\ &+\big(24+18x_{hZ}-6x_{hZ}^3\big)\mathrm{Li}_2(1-x_{hZ}) \\ &-\big(24x_{hZ}+6x_{hZ}^2\big)\log x_{hZ}\big) \\ &-12s_w^2\big(2Q_q^2 s_w^2\mp Q_q\big)x_{hZ}^3 \\ &\times\big(6-\big(4x_{hZ}-x_{hZ}^2\big)\pi^2+\big(24-18x_{hZ}+3x_{hZ}^2\big)\Phi\left(\frac{x_{hZ}}{4}\right) \\ &+\big(12-48x_{hZ}+12x_{hZ}^2\big)\mathrm{Li}_2(1-x_{hZ}) \\ &+12\log x_{hZ}-\big(12x_{hZ}-3x_{hZ}^2\big)\log^2 x_{hZ}\big)\big]\,. \end{aligned} \tag{4.35}$$

Note the corrected sign in the x_{hZ}^2 coefficient of the $\mathrm{Li}_2(1-x_{hZ})$ term with respect to Ref. [120]. The corresponding contributions with internal W loops are

$$
\begin{aligned}
C_1^{q,W} =& \pm \frac{\alpha}{2304\pi^3 Q_q s_w^2}\,\kappa_q \sin(\phi_q) x_{hW} \\
&\times \Big[\pm Q_q\big(24x_{Wh}^2 - 6x_{Wh}\big) - 18x_{Wh} \mp Q_q\big(3x_{Wh}^2 + 4x_{Wh}^3\big)\pi^2 \\
&\quad + \Big(18\big(x_{Wh} - x_{Wh}^2\big) - 9 \pm 3Q_q\big(8x_{Wh}^2 + 2x_{Wh} - 1\big)\Big)\Phi\left(\frac{1}{4x_{Wh}}\right) \\
&\quad + \Big(18 \pm 3Q_q\big(1 - 4x_{Wh}^3 - 3x_{Wh}^2\big)\Big)\Big(2\mathrm{Li}_2(1-x_{Wh}) + \log^2 x_{Wh}\Big) \\
&\quad + \Big(18x_{Wh} \pm Q_q\big(6x_{Wh} + 24x_{Wh}^2\big)\Big)\log x_{Wh}\Big]
\end{aligned}
\tag{4.36}
$$

and

$$
\begin{aligned}
C_2^{q,W} =& \frac{\alpha}{2304\pi^3 s_w^2}\,\kappa_q \sin(\phi_q) x_{hW} \\
&\times \Big[\big(24x_{Wh}^2 - 6x_{Wh}\big) - \big(3x_{Wh}^2 + 4x_{Wh}^3\big)\pi^2 \\
&\quad + 3\big(8x_{Wh}^2 + 2x_{Wh} - 1\big)\Phi\left(\frac{1}{4x_{Wh}}\right) \\
&\quad + 3\big(1 - 4x_{Wh}^3 - 3x_{Wh}^2\big)\Big(2\mathrm{Li}_2(1-x_{Wh}) + \log^2 x_{Wh}\Big) \\
&\quad + \big(6x_{Wh} + 24x_{Wh}^2\big)\log x_{Wh}\Big]\,,
\end{aligned}
\tag{4.37}
$$

where $x_{hW} \equiv M_h^2/M_W^2$. Note the corrections of the global factor of $\sqrt{2}$ for the bosonic WCs $C_1^{q,W\gamma}$, $C_1^{q,WZ}$, $C_{1,2}^{q,W}$ and $C_{1,2}^{q,Z}$ with respect to Ref. [120]. In Eqs. (4.36) and (4.37) we suppressed the explicit dependence on the CKM factors. For $q=u$, these two results should be multiplied by $|V_{ud}|^2 + |V_{us}|^2 + |V_{ub}|^2$, for $q=d$, by $|V_{ud}|^2 + |V_{cd}|^2$, and for $q=s$, by $|V_{us}|^2 + |V_{cs}|^2$. In all cases, the squared CKM matrix elements sum to unity to a very good approximation. Note that we neglected the tiny contributions of diagrams with internal top quarks. To simplify the above expressions, we defined $c_w = M_W/M_Z$ and $s_w = \sqrt{1-c_w^2}$. The actual calculation was performed in two independent setups, both based on self-written `FORM` [128] routines. The amplitudes were generated using `QGRAF` [129] and `FeynArts` [130], respectively, using the Feynman rules in background-field gauge from Ref. [131]. Both setups implement the two-loop recursion presented in Refs. [132, 133]. Needless to say, the two calculations yield identical results.

4.4 Gauge invariance

The listed expressions for the WCs are calculated in Feynman gauge ($\xi = 1$). Employing the calculation in R_ξ gauge, keeping ξ undetermined, shows that the complete result is not gauge independent, i.e., ξ does not drop out of the final result. This is the case in particular for Feynman diagrams with the external photon coupling to the W-bosons or its associated Goldstone bosons and Faddeev-Popov ghosts. When it couples to a fermion, either the open light quark line or the closed top-loop, the amplitude is independent of the gauge parameter. Similarly, all terms contributing to the CEDM WC are gauge invariant as the gluon does not couple to the weak bosons.
Remaining dependence on ξ suggests that the calculations in the κ framework in which only the dimension-four Higgs couplings are modified are not complete. The framework resembles closely the Higgs Effective Field Theory (HEFT) [134]. In HEFT, the dimension-four couplings are complemented by the interactions of higher-dimensional couplings involving additional Higgs bosons to facilitate gauge-independent results. Although the electroweak gauge group is a symmetry of the theory, the Goldstone bosons associated with the spontaneous symmetry breaking are treated as independent fields rather than components of the $SU(2)_L$-doublet. They are typically introduced through a non-linear realisation [135]. The Higgs boson is an independent singlet and its interactions with the Goldstone bosons are not restricted, limiting the predictive power of the theory [136].

We turn to the framework of Standard Model Effective Field Theory in Ch. 5 to perform these calculations, however. Its operator basis, e.g., the Warsaw basis [78], is widely used. This simplifies the implementation in generic R_ξ gauge and the comparability with other results from the literature.

Chapter 5

Global Constraints on Yukawa Operators in SMEFT

5.1 Introduction

Charge-Parity violating contributions to Higgs–fermion couplings are a well-motivated possibility of physics beyond the SM that might help address the problem of baryogenesis with new dynamics at the electroweak scale. Any such contributions are strongly constrained by null measurements of EDMs, and less strongly by Higgs production and decay data from colliders. The presence of several CP-violating phases can lead to cancellations and thus weaker bounds [116]. The interplay of EDM and collider constraints, in the presence of several CP-violating Higgs couplings to fermions simultaneously, is less well-known. In Ref. [119] constraints in the presence of two CP-violating parameters have been studied in detail. In this work, we scan over up to six different such parameters. This chapter is based on Ref. [137].

Frequently, model-independent bounds on such interactions are obtained in the so-called "κ framework" by rescaling the SM Yukawa coupling by an overall factor and a complex phase. See Chs. 3 and 4 and, e.g., Refs. [138–140] for analyses of LHC data. In Ref. [14], bounds on these factors are obtained by studying contributions to EDMs through Barr–Zee diagrams with internal fermion loops. In Refs. [117, 120] it is shown by explicit calculation within the κ framework that bosonic two-loop diagrams have a large impact on the EDM bounds for light quarks. However, it is pointed out that the way these bosonic contributions are computed, it leads to a gauge-dependent result [141]. This is related to the fact that the naive implementation of the κ framework, in which only the dimension-four Higgs couplings are modified, is not a consistent quantum field theory.

Another consistent way of obtaining model-independent bounds for CP-violating Higgs-fermion interactions is the use of the SM effective field theory (SMEFT) [77]; see Refs. [119, 142–144] for work in this direction. We take the same approach in this chapter.

For the purpose of this work, we assume that the contributions to the EDMs of the SM fermions arise from physics at a scale Λ that is sufficiently higher than the electroweak scale. This permits us to parameterise deviations from the SM in terms of operators in SMEFT. We assume that any of the operators of the form $(H^\dagger H)\bar{F}_L f_R H$ may have non-zero coefficients. Here, H is the complex Higgs doublet field, F_L a left-handed doublet fermion field, f_R a right-handed singlet fermion field, and we have suppressed flavour indices. The reason for focusing on this class of operators is that they are the only dimension-six operators that induce tree-level modifications to Higgs–fermion couplings. See Sec. 5.2 for a discussion. These operators will contribute to leptonic and hadronic dipole moments via a series of matching and renormalisation-group (RG) evolution. Our analysis takes into account the leading effects that arise at two-loop order in the electroweak interactions, as well as leading-logarithmic QCD corrections below the electroweak scale. We neglect any effects of CP-odd, flavour off-diagonal operators. The study of these effects is relegated to future work.

To understand the complex interplay between the considered operators, multiple Wilson coefficients (WCs) need to be varied simultaneously. To explore this computationally challenging multidimensional parameter space, we make use of the `GAMBIT` [145] global fitting framework, to which we have added a new module that allows for calculations of EDMs in the SMEFT, as well as the corresponding experimental likelihoods. We have also expanded the existing `ColliderBit` [146] module to be able to determine constraints on the WCs from measured properties of the Higgs boson at the LHC.

This work contains several new aspects and presents nontrivial results. We perform a multi-parameter fit to both LHC and EDM data. This corresponds to a more realistic scenario than single-parameter fits, as in a UV-complete model several CP phases are expected to be present. Moreover, we complement and correct some of the analytic expressions in the literature. In addition to updating existing constraints on either individual CP-odd Yukawa couplings (Figs. 5.5 and 5.6), or two CP-odd Yukawa couplings as in Ref. [119] (Fig. 5.7), we scan over up to six CP-even / CP-odd Yukawa couplings simultaneously for the first time (Figs. 5.8 - 5.12). While this still represents only a subset of all Yukawa operators, we argue that with current experimental results, including more parameters will not lead to additional significant constraints. For instance, allowing for any CP-odd contribution to the Yukawa of a light fermion (electron or up- and down-quark) would allow to fully cancel the corresponding EDM constraint, thus leaving only the LHC bounds in a trivial way. However, we find several nontrivial effects. Focusing on the heavier fermions, we find an intricate interplay between LHC and precision constraints that weakens the EDM bounds without lifting them fully. Not even by allowing for six independent parameters can we cancel all EDM constraints among the third-generation fermions, and nontrivial EDM bounds remain. A detailed discussion of these issues is found in Sec. 5.6.

In our analysis, we do not take into account perturbative and hadronic uncertainties. The effects of hadronic uncertainties on EDM bounds are studied in detail in Ref. [119] (see also Ref. [147]), and are not repeated here. They are relevant mainly for bounds on CP-violating Higgs couplings to the light quarks that arise from hadronic EDMs, as collider bounds are nearly absent. When allowing for the presence of several WCs at the same time, EDM bounds tend to get cancelled, and only collider bounds remain, so hadronic uncertainties are less relevant. Note also that bounds from arising from the electron EDM have no hadronic uncertainty. However, there is a large, previously overlooked perturbative uncertainty regarding the bottom and charm couplings, as discussed in Sec. 5.3. This uncertainty is analogous to the case discussed in Ref. [118], and is studied in detail in [148]. As not all relevant higher-order corrections are currently known, they are neglected in this analysis.

This chapter is organised as follows. In Section 5.2 we specify the operators that we want to constrain; namely, those that modify the SM Yukawa couplings at tree level. We then derive the modified Higgs–fermion couplings in the broken electroweak phase. In Sec. 5.3 we discuss the effective theory valid below the electroweak scale. The analytic contributions of the SMEFT operators for the partonic EDM of leptons and quarks are collected in Sec. 5.4. Most of these results are taken from the literature. In Sec. 5.5 we summarise the contributions of the partonic EDMs to the EDM of the physical systems that are actually constrained by experiment. It also describes the collider constraints on the SMEFT operators and contains a short discussion of the expected contribution of operators with mass dimension eight. The setup we use for GAMBIT is shown in detail in Sec. Ref. 5.6. Our main results are contained in Sec. 5.7. We conclude in Sec. 5.8. App. A contains the full generic R_ξ-gauge Lagrangian in the broken phase. In App. B, we discuss the alternative flavour basis in the electroweak broken phase that is used in Ref. [149].

5.2 Effective theory above the electroweak scale – SMEFT

The relevant part of the SMEFT Lagrangian including the 6-dimensional Yukawa operators is given in Eq. (3.3) coming with complex WCs C'_{fH} for each fermion species f. As is well-known, not all these complex parameters are physical due to the freedom of choosing the phases of the left- and right-handed fermion fields. To isolate the physical BSM parameters, we express as many parameters as possible in terms of observed quantities, e.g., the fermion masses and CKM matrix elements. To this end, we rewrite the Lagrangian in Eq. (3.3) in the broken phase using the linear decomposition of the Higgs field as

$$H = \begin{pmatrix} G^+ \\ \frac{1}{\sqrt{2}}(v + h + iG^0) \end{pmatrix} . \tag{5.1}$$

The terms that induce the fermion masses are

$$\mathcal{L}_{\text{mass}} = -\sum_{f=u,d,\ell} \frac{v}{\sqrt{2}} \bar{f}_L \left(Y_f - \frac{v^2}{2\Lambda^2} C'_{fH} \right) f_R + \text{h.c.}\,. \tag{5.2}$$

In analogy to the SM, we diagonalise the complete matrix in parentheses by biunitary transformations, parameterised by the field redefinitions

$$f_L \to U_f f_L\,, \qquad f_R \to W_f f_R\,, \tag{5.3}$$

with $f = u, d, \ell$, and U_f, W_f complex 3×3 matrices chosen such that after this rotation, the mass Lagrangian is

$$\mathcal{L}_{\text{mass}} = -\sum_{f=u,d,\ell} \frac{v}{\sqrt{2}} \bar{f}_L y_f^{\text{SM}} f_R + \text{h.c.}\,. \tag{5.4}$$

Here, the y_f^{SM} are real and diagonal matrices with entries that correspond to the observed fermion masses, i.e., $m_f = \frac{v}{\sqrt{2}} y_f^{\text{SM}}$. In other words, the conditions on U_f, W_f read

$$y_f^{\text{SM}} \equiv U_f^\dagger \left(Y_f - \frac{v^2}{2\Lambda^2} C'_{fH} \right) W_f\,. \tag{5.5}$$

The kinetic terms of the fermions are also affected by the transformation in Eq. (5.3), which leads to the appearance of the CKM matrix $V_{\text{CKM}} \equiv U_u^\dagger W_d$ in the charged gauge interactions of the left-handed quarks, in complete analogy to the SM.

The interaction terms of the fermions with a single Higgs field from Eq. (3.3) *after* performing the transformation in Eq. (5.3) are given by

$$\begin{aligned} \mathcal{L}_h &= -\sum_{f=u,d,\ell} \frac{h}{\sqrt{2}} \bar{f}_L U_f^\dagger \left(Y_f - \frac{3v^2}{2\Lambda^2} C'_{fH} \right) W_f f_R + \text{h.c.} \\ &= -\sum_{f=u,d,\ell} \frac{h}{\sqrt{2}} \bar{f}_L \left(y_f^{\text{SM}} - \frac{v^2}{\Lambda^2} C_{fH} \right) f_R + \text{h.c.}\,, \end{aligned} \tag{5.6}$$

where we defined $C_{fH} \equiv U_f^\dagger C'_{fH} W_f$. We see that, in the most general case, we can parameterise any deviation with respect to the SM by the rotated WCs C_{fH}. For later convenience, we split these coefficients into their real and imaginary parts,

$$C_{fH,ij} = \text{Re}[C_{fH,ij}] + i\,\text{Im}[C_{fH,ij}] \equiv C_{fH+,ij} + iC_{fH-,ij}\,. \tag{5.7}$$

with $C_{fH\pm,ij}$ real. This implies that the operator combinations proportional to the diagonal terms $C_{fH\pm,ii}$ are self-adjoint.

In the current work we consider the effect of the flavour-diagonal contributions, $C_{fH,ii}$, for the case that they contain additional sources of CP violation. This implies, as we shall see, that $C_{fH-,ii}$ is non-zero. Note, however, that in the absence of any type of flavour alignment with the SM Yukawas these operators also induce flavour violation beyond the SM, which we do not consider in this work. In a concrete model, we thus expect additional constraints from such flavour off-diagonal contributions of C_{fH} (see Refs. [109, 150] for a recent discussion). It is, however, possible to obtain both CP-even and CP-odd modifications in the flavour-diagonal Yukawas without any flavour-violation beyond the SM. This corresponds to a UV scenario in which the unitary transformations in Eqs. (5.5) and (5.3) that rotate to the mass eigenstates simultaneously diagonalise the coefficients C'_{fH}. In this setup, C_{fH} is diagonal but not necessarily real, meaning that CP violation beyond the SM is still possible.

In unitarity gauge, all BSM effects in our setup are contained in the Yukawa Lagrangian in the mass-eigenstate basis

$$\begin{aligned}\mathscr{L}_{\text{Yukawa}} = \sum_f \Bigg[\Bigg(-m_f - m_f \frac{h}{v} + \frac{v^3}{2\sqrt{2}\Lambda^2} C_{fH+} \left(2\frac{h}{v} + 3\frac{h^2}{v^2} + \frac{h^3}{v^3} \right) \Bigg) \bar{f} f \\ + \frac{v^3}{2\sqrt{2}\Lambda^2} C_{fH-} \left(2\frac{h}{v} + 3\frac{h^2}{v^2} + \frac{h^3}{v^3} \right) \bar{f} i \gamma_5 f \Bigg]\end{aligned} \tag{5.8}$$

Here, the sum runs over all charged fermion fields, $f = u, d, s, c, b, t, e, \mu, \tau$, and we have traded the generation indices on the WCs in favour of the flavour label, f, since we focus on the flavour-diagonal case. We will use this more compact notation in the remainder of this work. In App. A we present the corresponding Lagrangian for the generic R_ξ gauge. A different basis has been used in Ref. [149] to present the bounds on the WCs, see App. B.

As long dimension-six SMEFT is a good approximation, and the h^2 and h^3 interactions in Eq. (5.8) do not affect the observables considered, the bounds on $C_{fH\pm}$ directly translate to bounds on the κ-framework parameters, discussed in Sec. 3.1, via

$$\kappa_f \cos\phi_f \mathrel{\hat{=}} 1 - \frac{v}{\sqrt{2} m_f} \frac{v^2}{\Lambda^2} C_{fH+} \,, \qquad \kappa_f \sin\phi_f \mathrel{\hat{=}} - \frac{v}{\sqrt{2} m_f} \frac{v^2}{\Lambda^2} C_{fH-} \,. \tag{5.9}$$

This is actually the case for the observables and the precision that we consider. A possible exception is the top contribution to the LHC observables, see the discussion in Sec. 5.5.

Using the Lagrangian in Eq. (5.8), we will be able to set constraints on the $C_{fH\pm}$ couplings from LHC measurements. Low-energy probes of CP violation, however, also place significant constraints on these couplings. Our aim is to capture the numerically leading effects. To this end we work with a tower of effective theories. Apart from a few exceptions that we discuss below, the RG evolution from Λ to μ_{ew} within SMFET can be neglected, as (most) Yukawa operators do not mix into the CP-violating dipoles for the electron and light-quarks, relevant for EDMs. In this case, the leading effects are obtained at the electroweak scale by matching to the effective theory in which the heavy degrees of the SM are integrated out, and by subsequently running to the hadronic scale. In contrast, the few contributions that are induced from (two-loop) mixing within SMEFT will come with a UV-sensitive logarithm, $\log M_h/\Lambda$.

5.3 Effective theory below the electroweak scale

We will extract constraints on the coefficients in Eq. (5.8) from the experimental bounds on the electron, neutron, and mercury EDMs. We will make the assumption that these EDMs are induced solely by the electron and partonic CP-violating electric (EDM) and chromoelectric dipole operators (CEDM), and the purely gluonic CP-violating Weinberg operator [121] with coefficients d_e, d_q, $\tilde{d}_q$, and w, respectively. Therefore, we neglect (subleading) contributions from the matrix elements of four-fermion operators. Here, q collectively denotes light quarks, u, d, s. The charm-quark is typically not included since presently there are no lattice computations for the hadronic matrix elements of its operators. The above coefficients are traditionally defined via the effective, CP-odd Lagrangian valid at hadronic energies $\mu_{\text{had}} \simeq 2\,\text{GeV}$ [83],

$$\begin{aligned}\mathcal{L}_{\text{eff}} = &- d_e \frac{i}{2}\bar{e}\sigma^{\mu\nu}\gamma_5 e F_{\mu\nu} - d_q \frac{i}{2}\bar{q}\sigma^{\mu\nu}\gamma_5 q F_{\mu\nu} \\ &- \tilde{d}_q \frac{ig_s}{2}\bar{q}\sigma^{\mu\nu}T^a\gamma_5 q G^a_{\mu\nu} + \frac{1}{3} w f^{abc} G^a_{\mu\sigma} G^{b,\sigma}_{\nu} \widetilde{G}^{c,\mu\nu}\,.\end{aligned} \tag{5.10}$$

Here, $\sigma^{\mu\nu} = \frac{i}{2}[\gamma^\mu, \gamma^\nu]$, T^a are the generators of SU(n_c) in the fundamental representation normalised as $\text{Tr}[T^a, T^b] = \delta^{ab}/2$, $n_c = 3$ is the number of colours, and we collect our conventions for the field strength and its dual below. The contributions from the Weinberg operator turn out to be subdominant because of its small nuclear matrix elements [81, 83], but we keep them for completeness.

The partonic dipole moments d_q and $\tilde{d}_q$ as well as the coefficient w are obtained from the SMEFT WCs in Eq. (5.8) via a sequence of matching at the weak scale, and the bottom- and charm-flavour thresholds, as well as the RG evolution between each scale, as outlined in Refs. [14, 80, 118, 151, 152]. The resummation of logarithms is phenomenologically relevant for the hadronic dipole operators that mix under QCD. In the current analysis, we work at the leading-logarithmic order for quark operators. QCD corrections are also large for the bottom- and charm-quark contributions to the electron EDM. They are calculated here [148] but are not included in our analysis.

To perform the sequence of matching and RG evolution connecting the electroweak-scale Lagrangian, Eq. (5.8), with the hadronic-scale one, Eq. (5.10), requires the full flavour-conserving, CP-odd effective Lagrangian below the electroweak scale up to mass dimension six. In the conventions and basis of Ref. [118], adapted from Ref. [152], it reads:

$$\mathcal{L}_{\text{eff}} = -\sqrt{2}G_F \Bigg(\sum_{q\neq q'} \Big[\sum_{i=1,2} C_i^{qq'} O_i^{qq'} + \frac{1}{2} \sum_{i=3,4} C_i^{qq'} O_i^{qq'} \Big] + \sum_q \sum_{i=1,\dots,4} C_i^q O_i^q + C_w O_w + \sum_\ell C_3^\ell O_3^\ell \Bigg) , \tag{5.11}$$

where the sums run over all active quarks with masses below the weak scale, e.g., $q, q' = u, d, s, c, b$ in the five-flavour theory. The linearly independent operators are[1]

$$O_1^{qq'} = (\bar{q}q)\,(\bar{q}'\,i\gamma_5 q')\,, \qquad O_2^{qq'} = (\bar{q}\,T^a q)\,(\bar{q}'\,i\gamma_5 T^a q')\,, \tag{5.12}$$

$$O_3^{qq'} = \frac{1}{2}\epsilon^{\mu\nu\rho\sigma}(\bar{q}\sigma_{\mu\nu}q)\,(\bar{q}'\sigma_{\rho\sigma}q')\,, \qquad O_4^{qq'} = \frac{1}{2}\epsilon^{\mu\nu\rho\sigma}(\bar{q}\sigma_{\mu\nu}T^a q)\,(\bar{q}'\sigma_{\rho\sigma}T^a q')\,, \tag{5.13}$$

$$O_1^q = (\bar{q}q)\,(\bar{q}\,i\gamma_5 q)\,, \qquad O_2^q = \frac{1}{2}\epsilon^{\mu\nu\rho\sigma}(\bar{q}\sigma_{\mu\nu}q)\,(\bar{q}\,\sigma_{\rho\sigma}q)\,, \tag{5.14}$$

$$O_3^q = \frac{eQ_q}{2}\frac{m_q}{g_s^2}\,\bar{q}\sigma^{\mu\nu}q\,\widetilde{F}_{\mu\nu}\,, \qquad O_4^q = -\frac{1}{2}\frac{m_q}{g_s}\,\bar{q}\sigma^{\mu\nu}T^a q\,\widetilde{G}^a_{\mu\nu}\,, \tag{5.15}$$

$$O_3^\ell = \frac{eQ_\ell}{2}\frac{m_\ell}{e^2}\,\bar{\ell}\sigma^{\mu\nu}\,i\gamma_5\ell\,F_{\mu\nu}\,, \qquad O_w = -\frac{1}{3\,g_s}f^{abc}\,G^a_{\mu\sigma}G^{b,\sigma}_{\nu}\widetilde{G}^{c,\mu\nu}\,. \tag{5.16}$$

The powers of e and g_s in the operator definitions above are fixed such that all WCs have the same $\hbar$ dimension, thus making the calculation of operator mixing more transparent.

C_w as well as some of the anomalous dimensions that control operator mixing depend on the conventions for the covariant derivatives for quarks and leptons, the field strength tensor, and the dual tensors. Our conventions (same as in Ref. [118]) read

$$D_\mu^q \equiv \partial_\mu - ig_s T^a G^a_\mu + ieQ_q A_\mu\,, \qquad D_\mu^\ell \equiv \partial_\mu + ieQ_\ell A_\mu\,, \tag{5.17}$$

$$G^a_{\mu\nu} \equiv \partial_\mu G^a_\nu - \partial_\nu G^a_\mu + g_s f^{abc} G^b_\mu G^c_\nu, \quad \widetilde{G}^{a,\mu\nu} \equiv \frac{1}{2}\epsilon^{\mu\nu\rho\sigma}G^a_{\rho\sigma}\,, \quad \widetilde{F}^{\mu\nu} \equiv \frac{1}{2}\epsilon^{\mu\nu\rho\sigma}F_{\rho\sigma}\,,$$

with $\epsilon_{0123} = -\epsilon^{0123} = 1$.

For the correct projections onto the (C)EDM operators, their effective Feynman rules are obtained by adding source terms $\bar{\eta}\psi + \bar{\psi}\eta + J^\mu A_\mu$ to the exponential on the right-hand side of Eq. (2.19). Applying Eq. (2.21) with the source functions η, $\bar{\eta}$ and J^μ we obtain the Green's

[1] The definition of the $O_3^{qq'}$, $O_4^{qq'}$ operators in terms of the ϵ-tensor is convenient when going beyond the leading-logarithmic approximation, as they remain self-adjoint also in $d = 4 - 2\epsilon$ dimensions. It is thus convenient to also define O_2^q and the dipoles O_3^q and O_4^q in an analogous manner. To express the operators in the more conventional $i\sigma^{\mu\nu}\gamma^5$ notation, one can use the $d = 4$ relation

$$i\sigma^{\mu\nu}\gamma_5 \overset{[d=4]}{=} \frac{1}{2}\epsilon^{\mu\nu\rho\sigma}\sigma_{\rho\sigma}\,,$$

where $\epsilon_{0123} = -\epsilon^{0123} = 1$. For details concerning the next-to-leading-logarithmic analysis, see Ref. [118].

function for the vertex of a photon, a fermion, and an antifermion. Omitting the external fields yields the Feynman rule for the EDM in momentum space

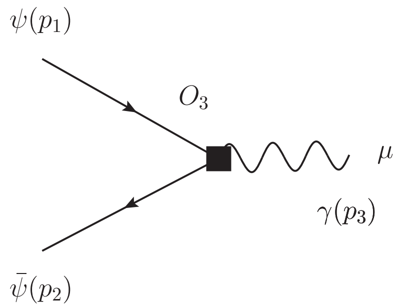

$$\sim \qquad ieQ_f\left(\not{p}_3\gamma^\mu - p_3^\mu\right)\gamma_5 \tag{5.18}$$

with $p_1 = p_2 + p_3$. If the external boson is a gluon, the eQ_f gets swapped for a QCD generator $g_s T^A_{ij}$ with gluon index A and the colour indices i and j for the incoming and outgoing quarks, respectively.

The comparison of Eqs. (5.10) and (5.11) gives the relation between d_e, d_q, $\tilde{d}_q$, w and the WCs of the three-flavour EFT evaluated at the hadronic scale $\mu_{\text{had}} = 2\,\text{GeV}$:

$$\begin{aligned} d_e &= \sqrt{2}G_F\,\frac{eQ_e}{4\pi\alpha}m_e\,C_3^e\,, \\ d_q(\mu_{\text{had}}) &= \sqrt{2}G_F\,\frac{eQ_q}{4\pi\alpha_s}m_q\,C_3^q(\mu_{\text{had}})\,, \\ \tilde{d}_q(\mu_{\text{had}}) &= -\sqrt{2}G_F\,\frac{1}{4\pi\alpha_s}m_q\,C_4^q(\mu_{\text{had}})\,, \\ w(\mu_{\text{had}}) &= \sqrt{2}G_F\,\frac{1}{g_s}\,C_w(\mu_{\text{had}})\,. \end{aligned} \tag{5.19}$$

Note that C_3^e is scale independent with regard to the strong interaction, i.e., $C_3^e(\mu_{\text{had}}) = C_3^e(\mu_{\text{ew}})$ with $\mu_{\text{ew}} \simeq 100\,\text{GeV}$. The procedure to calculate C_3^e, $C_3^q(\mu_{\text{had}})$, $C_4^q(\mu_{\text{had}})$, and $C_w(\mu_{\text{had}})$ depends on the flavour quantum numbers of the SMEFT operators. In the following section, we describe the different cases and present the corresponding results.

5.4 Electroweak matching and RG evolution to the hadronic scale

In this section, we discuss how to obtain the WCs of the EFT below the electroweak scale as a function of the Yukawa SMEFT WCs. Since all operators in Eq. (5.11) are CP odd, all contributions are proportional to the CP-odd couplings C_{fH-}. The final results for the required initial conditions $C_1^{qq'}(\mu_{\text{ew}})$, $C_1^q(\mu_{\text{ew}})$, $C_w(\mu_{\text{ew}})$, $C_3^e(\mu_{\text{ew}})$, $C_3^q(\mu_{\text{ew}})$, and $C_4^q(\mu_{\text{ew}})$ are collected below in Eqs. (5.20), (5.21), (5.22), (5.23), and (5.24), respectively. These are all the initial conditions required for the leading-log QCD analysis.

We begin the discussion with contributions that are UV sensitive, i.e., proportional to

$\log(\mu_{\rm ew}/\Lambda)$. There are two equivalent ways of obtaining them. One way is to identify those SMEFT Yukawa operators O_{fH} that mix into the SMEFT dipole operators O_{fW}, O_{fB} and O_{qG}. The mixing induces dipole WCt proportional to the leading UV logarithm $\log \mu_{\rm ew}/\Lambda$, and the subsequent tree-level matching onto the Lagrangian Eq. (5.11) potentially induces non-zero coefficients $C_3^e(\mu_{\rm ew})$, $C_3^q(\mu_{\rm ew})$, and $C_4^q(\mu_{\rm ew})$. In fact, only the cases occur in which the six-dimensional Yukawa operators in Eq. (3.3) mix into their respective six-dimensional dipole operators in Eq. (3.4) Here, we consider only mixing into dipole operators with light fermions. The two-loop mixing has been calculated for the electron case in Ref. [80].

An alternative way of obtaining these $\log \mu_{\rm ew}/\Lambda$ terms is to directly perform the two-loop electroweak matching calculation to extract $C_3^f(\mu_{\rm ew})$, for the light-fermion flavours $f = e, u, d, s$ (see representative diagrams in the lower panels in Fig. 5.2). For these coefficients, the contributions to the matching proportional to the SMEFT coefficients C_{fH-} are divergent and thus include a term proportional to the UV-sensitive logarithm $\log M_h/\Lambda$. We perform the matching calculation explicitly and find that only the contributions to $C_3^f(\mu_{\rm ew})$ are UV sensitive, while the matching for $C_4^q(\mu_{\rm ew})$ is UV finite. To obtain gauge-independent results in this calculation, it was necessary [141] to include the dimension-five vertices in the Lagrangian in the broken phase (see App. A) that were missed in Ref. [117]. The UV-divergent contributions are a direct consequence of including these dimension-five vertices. The corresponding logarithmic terms in our results for $C_3^e(\mu_{\rm ew})$ are in agreement with the anomalous dimension presented in Ref. [80]. The UV-sensitive logarithms for the quark case are presented here in our publication [137] for the first time.

When electroweak UV logarithms are induced, the electroweak non-logarithmic terms in the matching at $\mu_{\rm ew}$ that accompany them are scheme dependent and formally part of the next-to-leading-logarithmic (NLL) approximation. They should not be included in the analysis, and we thus disregard them.

For those contributions that are not UV sensitive, we directly perform the matching of the SMEFT Lagrangian Eq. (5.8) onto the effective Lagrangian Eq. (5.11), integrating out the heavy degrees of the SM (top-quark, Higgs, and the W and Z bosons). In all calculations, we employ a general R_ξ gauge for all gauge bosons and have verified the independence of our results from the gauge-fixing parameters. All calculations were performed using self-written `FORM` [128] routines, implementing when necessary the two-loop recursion presented in Refs. [132, 133]. The amplitudes were generated using `QGRAF` [129] and `FeynArts` [130].

At tree level and leading order in the $1/\Lambda$ expansion, integrating out the Higgs induces the following non-zero initial conditions for four-quark operators (see first two diagrams in Fig. 5.1)

$$C_1^{qq'}(\mu_{\rm ew}) = \frac{m_q m_{q'}}{M_h^2}\frac{v}{\sqrt{2}m_{q'}}\frac{v^2}{\Lambda^2}C_{q'H-}\,, \qquad C_1^q(\mu_{\rm ew}) = \frac{m_q^2}{M_h^2}\frac{v}{\sqrt{2}m_q}\frac{v^2}{\Lambda^2}C_{qH-}\,, \tag{5.20}$$

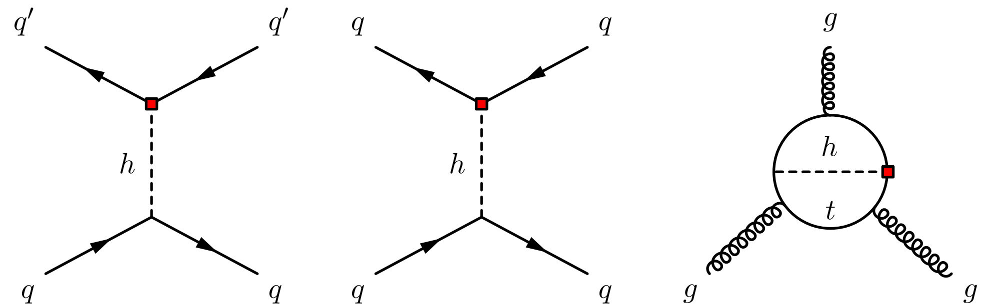

Figure 5.1: Sample Feynman diagrams contributing to the tree-level matching of four-quark operators (first two diagrams) and the two-loop matching inducing the Weinberg operator (third diagram). The red square vertex indicates a CP-violating Higgs Yukawa, C_{fH-}.

with $q, q' = u, d, s, c, b$. In principle, also the analogous operators with leptons are induced ($\bar{q}q\bar{\ell}\ell$, $\bar{\ell}'\ell'\bar{\ell}\ell$). However, since we will rely on a fixed-order computation to predict $d_e \propto C_3^e$ (see below), these operators do not enter our analysis.

The matching at the electroweak scale also induces the Weinberg and dipole operators, but only at the two-loop level. The Weinberg operator obtains a two-loop initial condition at μ_{ew} only from the top-quark operator (see third diagram in Fig. 5.1):

$$
\begin{aligned}
C_w(\mu_{\text{ew}}) = \frac{\alpha_s^2}{(4\pi)^2}\frac{v}{\sqrt{2}m_t}\frac{v^2}{\Lambda^2}C_{tH-}\frac{x_{th}}{2(1-4x_{th})^3}\Big\{&3 - 14x_{th} + 8x_{th}^2 \\
&+ 6x_{th}(1-2x_{th}+2x_{th}^2)\Phi\left(\frac{1}{4x_{th}}\right) + \left(2+10x_{th}-12x_{th}^2\right)\log x_{th}\Big\}\,,
\end{aligned}
\tag{5.21}
$$

with $\Phi(z)$ defined in Eq. (5.38). This result agrees with Ref. [14], but is, as far as we are aware, presented here in our publication [137] for the first time in a non-parametric form.

The electron photon dipole (O_3^e), and light-quark photon and gluon dipoles (O_3^q, O_4^q with $q = u, d, s$) all receive two-loop initial conditions by integrating out the top-quark and the Higgs, W, and Z bosons:

$$
C_3^e(\mu_{\text{ew}}) = \frac{\alpha^2}{(4\pi)^2}\sum_{f'=e,\mu,\tau,b,c,t}\frac{v}{\sqrt{2}m_{f'}}\frac{v^2}{\Lambda^2}C_{f'H-}\,A^e[f']\,,
\tag{5.22}
$$

$$
C_3^q(\mu_{\text{ew}}) = \frac{\alpha\alpha_s}{(4\pi)^2}\sum_{f'=q,\tau,t}\frac{v}{\sqrt{2}m_{f'}}\frac{v^2}{\Lambda^2}C_{f'H-}\,A^q[f']\,,
\tag{5.23}
$$

$$
C_4^q(\mu_{\text{ew}}) = \left(\sum_{q'=q,t}\frac{\alpha_s^2}{(4\pi)^2}B_s^q[q'] + \frac{\alpha\alpha_s}{(4\pi)^2}B_{\text{ew}}^q[q]\right)\frac{v}{\sqrt{2}m_{q'}}\frac{v^2}{\Lambda^2}C_{q'H-}\,,
\tag{5.24}
$$

with the precise decomposition of the coefficient functions A^f, B_s^q, and B_{ew}^q discussed below.

A few clarifications regarding Eqs. (5.22)–(5.24) are in order. We calculate the electroweak

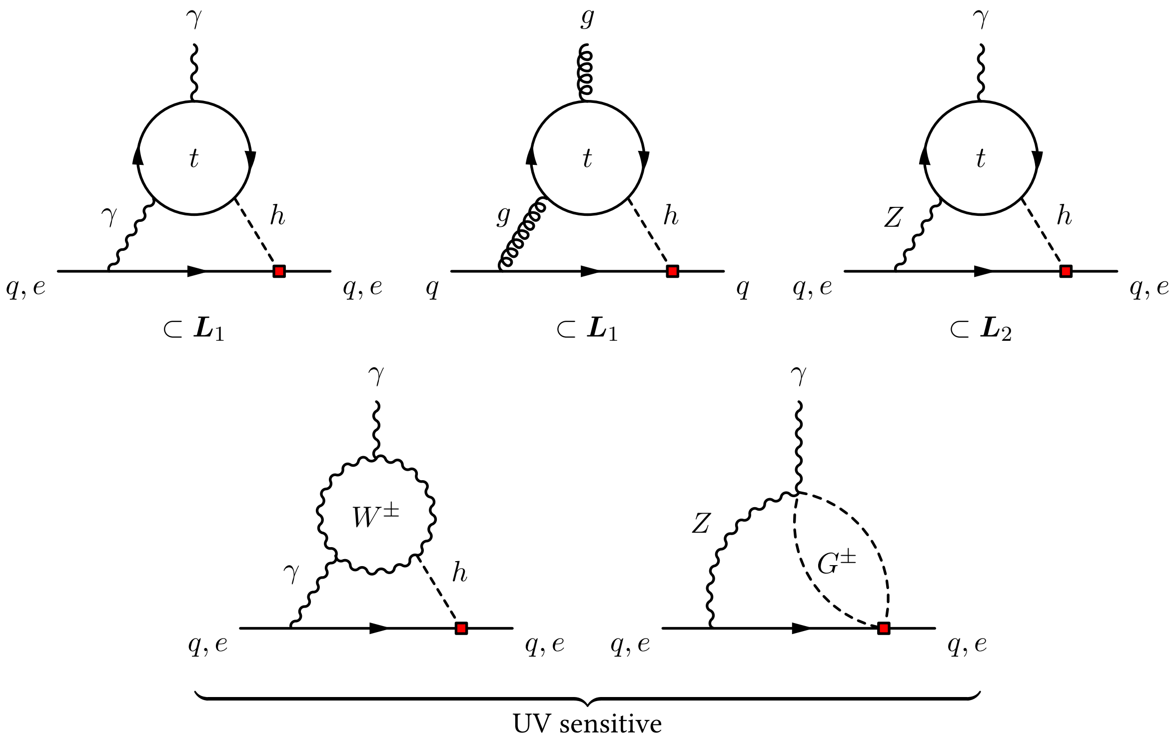

Figure 5.2: Representative Barr–Zee-type Feynman diagrams contributing to the two-loop matching of dipole operators at the electroweak scale. The label under the diagrams indicates the loop function ($\boldsymbol{L}_1$ and $\boldsymbol{L}_2$) to which the corresponding diagram contributes. The red square vertex indicates a CP-violating Higgs Yukawa, C_{fH-}. Electroweak diagrams like those in the second row are responsible for the UV sensitivity of contributions proportional to C_{eH-} and C_{qH-} for the electron and light-quark EDM operators, respectively. Diagrams with dimension-five couplings (lower right) are required to obtain a gauge-invariant result. See main text for details.

matching in fixed-order perturbation theory whenever there are no QCD corrections that are enhanced by large logarithms related to light fermion masses. This is the case for all diagrams with top-quark loops, and the diagrams with lepton loops contributing to the electron dipole, i.e., the contributions $C_3^e(\mu_{\rm ew})$ that are proportional to $C_{\ell H-}$. (We also neglect the running of the electromagnetic coupling constant.) Therefore, the coefficients $C_{3/4}^q(\mu_{\rm ew})$ do not receive threshold contributions from virtual quarks other than the top quark, since those are properly included via the RG-mixing of the four-quark operators (Eq. (5.20)) into $C_{3/4}^q$, see below. In principle, also the contributions to $C_3^e(\mu_{\rm ew})$ of all quarks other than the top should be obtained from the RG evolution; however, the corresponding mixed QED-QCD RG evolution is currently unknown[1]. Thus, we temporarily include the contribution of bottom and charm quarks to $C_3^e(\mu_{\rm ew})$ with a fixed-order calculation, with the understanding that corrections to these results

[1]The QCD corrections to the bottom and charm contributions are naively estimated to be large (factor of a few in C_3^e) but require a more complex calculation [148].

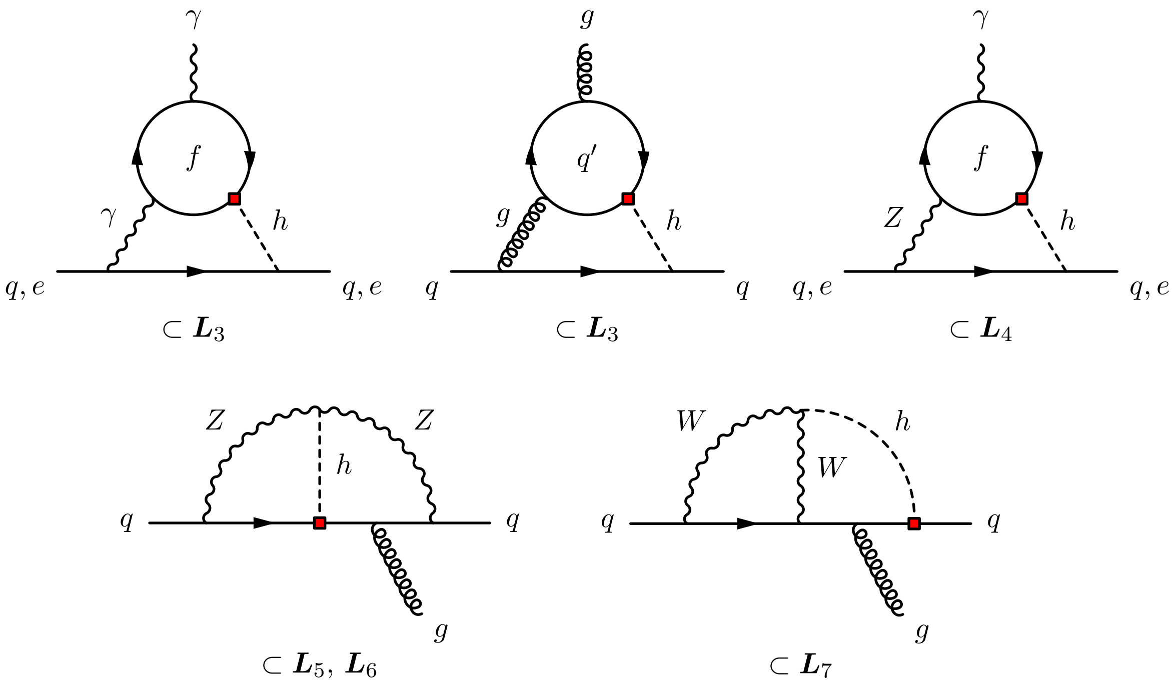

Figure 5.3: Representative Barr–Zee-type Feynman diagrams contributing to the two-loop matching of dipole operators at the electroweak scale. The label under the diagrams indicates the loop function ($\boldsymbol{L}_3$ – $\boldsymbol{L}_7$) to which the corresponding diagram contributes. The red square vertex indicates a CP-violating Higgs Yukawa, C_{fH-}. Here, f denotes fermions and q' quarks. The electroweak contributions to the CEDM operator from diagrams like the ones in the second row are UV finite, as opposed to the ones in Fig. 5.2. See main text for details.

may be large. On the other hand, we do not include the corresponding fixed-order results for the light-quark (u, d, s) contributions to $C_3^e(\mu_{\rm ew})$. In addition to the issue of the large unknown QCD corrections, these contributions are suppressed by the light-quark masses. Therefore, it is not C_3^e but the $C_{3/4}^q$ coefficients that provide the numerically leading constraints on the C_{qH-} couplings for light quarks. Similarly, we do not include the contributions of the electron and muon to $C_3^q(\mu_{\rm ew})$. The appearance of their masses (which are much smaller than the lowest scale, $\mu_{\rm had}$, where these operators can be meaningfully defined) in the logarithms would spuriously enhance the corresponding bounds by large factors. These contributions should be taken into account properly by using the RG. The tau, on the other hand, has a mass large enough to justify a fixed-order calculation as an estimate and is thus included. Note, however, that numerically the strongest bounds on the coefficients of all three leptons by far arise from the electron EDM, and their contributions to the hadronic EDMs do not play a role in our analysis, given current experimental data. The decomposition of the coefficients A^f, B_s^q, and

B^q_{ew} in Eqs. (5.22)–(5.24) are

$$A^f[f'] = \begin{cases} \underbrace{4n_c Q_t^2 \boldsymbol{L}_1}_{t\gamma-\text{Barr–Zee}} \quad + \underbrace{4n_c Q_t Q_f^{-1} v_{Zf} v_{Zt} \boldsymbol{L}_2}_{tZ-\text{Barr–Zee}} \quad - \underbrace{\frac{4Q_f + 2T_3^f}{Q_f c_w^2} \log \frac{M_h^2}{\Lambda^2}}_{\text{ew UV sensitivity}} & \text{for } f = f' \\ \underbrace{4n_c[f'] Q_{f'}^2 \boldsymbol{L}_3}_{f'\gamma-\text{Barr–Zee}} \quad + \underbrace{4n_c[f'] Q_{f'} Q_f^{-1} v_{Zf} v_{Zf'} \boldsymbol{L}_4}_{f'Z-\text{Barr–Zee}} & \text{for } f \neq f' \end{cases} \tag{5.25}$$

$$B^q_s[q'] = \begin{cases} \underbrace{2\boldsymbol{L}_1}_{tg-\text{Barr–Zee}} & \text{for } q = q' \\ \underbrace{2\boldsymbol{L}_3}_{tg-\text{Barr–Zee}} & \text{for } q \neq q' = t \end{cases} \tag{5.26}$$

$$B^q_{\text{ew}}[q] = \underbrace{(v_{Zq}^2 - a_{Zq}^2)\boldsymbol{L}_5 + (v_{Zq}^2 + a_{Zq}^2)\boldsymbol{L}_6}_{\text{ew-finite } qZ \text{ contribution}} \quad \underbrace{+\frac{1}{s_w^2}\boldsymbol{L}_7}_{\text{ew-finite } qW \text{ contribution}} \tag{5.27}$$

with $n_c[t] = n_c[q] = n_c$ and $n_c[\ell] = 1$. The vector and axial-vector coupling of the Z boson to a fermion are $v_f^Z \equiv \frac{1}{2s_w c_w}(T_3^f - 2Q_f s_w^2)$ and $a_f^Z \equiv \frac{1}{2s_w c_w} T_3^f$, respectively. In Fig. 5.2 and Fig. 5.3, we show representative diagrams contributing to $\boldsymbol{L}_1$–$\boldsymbol{L}_7$. They can be inferred from the expressions in Eqs. (4.30) to (4.37) without the gauge-dependent bosonic EDM coefficients. As discussed, only $A^e[e]$ and $A^q[q]$ contain UV-sensitive electroweak contributions proportional to $\log M_h^2/\Lambda^2$. The individual contributions coming from γ, $W^\pm$ and Z coupling to the open fermion line in the lower right Feynman diagram in Fig. 5.2 are

$$A^f_{\text{UV-sensitive}}[f] = \quad A^f_\gamma + A^f_W + A^f_Z \tag{5.28}$$

$$= \left(-8Q_f + \frac{2T_3^f}{s_w^2} - \frac{(c_w^2 - s_w^2)(2T_3^f - 4Q_f s_w^2)}{c_w^2 s_w^2} \right) \log\left(\frac{M_H^2}{\Lambda^2} \right). \tag{5.29}$$

All other scheme-dependent finite electroweak threshold corrections have been dropped in $A^e[e]$ and $A^q[q]$. We have, however, kept the terms from top-quarks loops (proportional to $\boldsymbol{L}_1$ and $\boldsymbol{L}_2$) as they depend on the top-quark Yukawa and as such, are independent of the scheme-dependent electroweak corrections. The loop functions ($\boldsymbol{L}_i$) read

$$\boldsymbol{L}_1 = 2x_{th}\left(2 + \log x_{th}\right) + x_{th}\left(1 - 2x_{th}\right)\Phi\left(\frac{1}{4x_{th}}\right), \tag{5.30}$$

$$\boldsymbol{L}_2 = \frac{x_{tZ} x_{th}}{x_{tZ} - x_{th}}\left[(1 - 2x_{th})\Phi\left(\frac{1}{4x_{th}}\right) - 2\log x_{hZ} - (1 - 2x_{tZ})\Phi\left(\frac{1}{4x_{tZ}}\right)\right], \tag{5.31}$$

$$\boldsymbol{L}_3 = x_{f'h}\Phi\left(\frac{1}{4x_{f'h}}\right) \overset{x_{f'h} \ll 1}{\simeq} x_{f'h}\left(\log^2 x_{f'h} + \frac{\pi^2}{3}\right), \tag{5.32}$$

$$\boldsymbol{L}_4 = \frac{x_{f'Z}x_{f'h}}{x_{f'Z}-x_{f'h}}\left[\Phi\left(\frac{1}{4x_{f'Z}}\right)-\Phi\left(\frac{1}{4x_{f'h}}\right)\right] \tag{5.33}$$

$$\overset{x_{f'Z},x_{f'h}\ll 1}{\simeq} \frac{x_{f'Z}x_{f'h}}{x_{f'Z}-x_{f'h}}\left(\log^2 x_{f'h}-\log^2 x_{f'Z}\right), \tag{5.34}$$

$$\begin{aligned}\boldsymbol{L}_5 = \frac{1}{3}\Big[&\left(3x_{hZ}^3-18x_{hZ}^2+24x_{hZ}\right)\Phi\left(\frac{x_{hZ}}{4}\right)+6x_{hZ}\left(1+2\log x_{hZ}\right)\\ &+\left(12x_{hZ}^3-48x_{hZ}^2+12x_{hZ}\right)\mathrm{Li}_2(1-x_{hZ})\\ &+\left(x_{hZ}^3-4x_{hZ}^2\right)\pi^2+\left(3x_{hZ}^3-12x_{hZ}^2\right)\log^2 x_{hZ}\Big],\end{aligned} \tag{5.35}$$

$$\begin{aligned}\boldsymbol{L}_6 = \frac{2}{9}x_{Zh}^2\Big[&\left(3x_{hZ}^3-6x_{hZ}^2-24x_{hZ}\right)\Phi\left(\frac{x_{hZ}}{4}\right)\\ &+\left(6x_{hZ}^2+24x_{hZ}\right)\log x_{hZ}+\left(6x_{hZ}^2-24x_{hZ}\right)\\ &+\left(6x_{hZ}^3-18x_{hZ}-24\right)\mathrm{Li}_2(1-x_{hZ})+\left(3x_{hZ}+4\right)\pi^2\Big],\end{aligned} \tag{5.36}$$

$$\begin{aligned}\boldsymbol{L}_7 = \frac{1}{18}x_{hW}\Big[&\left(3-6x_{Wh}-24x_{Wh}^2\right)\Phi\left(\frac{x_{hW}}{4}\right)+\left(3x_{Wh}^2+4x_{Wh}^3\right)\pi^2\\ &-\left(6x_{Wh}+24x_{Wh}^2\right)\log x_{Wh}+\left(6x_{Wh}-24x_{Wh}^2\right)\\ &+\left(12x_{Wh}^3+9x_{Wh}^2-3\right)\left(2\mathrm{Li}_2(1-x_{Wh})+\log^2 x_{Wh}\right)\Big],\end{aligned} \tag{5.37}$$

where we defined the mass ratios $x_{ij} \equiv M_i^2/M_j^2$. For the case of small fermion masses, i.e., when $x \ll 1$, we have expanded for convenience the $\Phi(z)$ function. Our loop functions $\boldsymbol{L}_5$, $\boldsymbol{L}_6$, $\boldsymbol{L}_7$ correct a global factor of $\sqrt{2}$ with respect to the corresponding ones in Ref. [120] and a typographical sign mistake in the x_{hZ}^3 coefficient of $\mathrm{Li}_2(1-x_{hZ})$ in $\boldsymbol{L}_5$ in the same reference. The loop function $\boldsymbol{L}_2$ implicitly corrects an error in Eq. (A.5) of Ref. [80], where two logarithms seem to have been incorrectly added. The function $\Phi(z)$ in the results above is presented before in Eqs. (4.26) and (4.28) and repeated here by [132]

$$\Phi(z) = \begin{cases} 4\sqrt{\frac{z}{1-z}}\mathrm{Cl}_2\left(2\arcsin(\sqrt{z})\right) & \text{for } 0 \le z < 1\,, \\ \frac{1}{\lambda}\left(-4\,\mathrm{Li}_2(\frac{1-\lambda}{2})+2\log^2(\frac{1-\lambda}{2})-\log^2(4z)+\frac{\pi^2}{3}\right) & \text{for } z > 1\,. \end{cases} \tag{5.38}$$

Having computed the initial conditions at the electroweak scale, we perform the QCD RGE evolution from $\mu_{\rm ew}$ to the hadronic scale $\mu_{\rm had} = 2\,\mathrm{GeV}$ (see Refs. [14, 118] for details). For operators with quarks, the RGE evolution resums large QCD logarithms and accounts for mixing among different operators. In the case of light-quark SMEFT operators, the tree-level induced four-quark operators ($O_1^{qq'}$ and O_1^q) mix at one-loop under QCD into the quark dipoles. Nevertheless, the contributions to $C_3^q(\mu_{\rm ew})$ and $C_4^q(\mu_{\rm ew})$ of two-loop diagrams with top-quark and Z-boson loops provide the numerically dominant effect [121] as the four-fermion operators

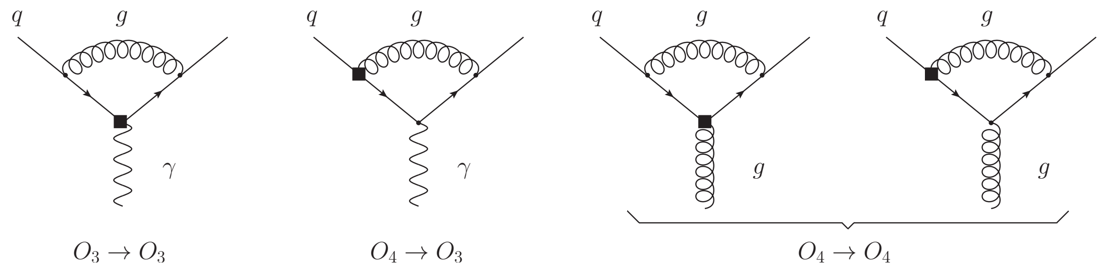

Figure 5.4: Feynman diagrams contributing to the operator mixing among the (C)EDM operators at the 1-loop order in α_s. The black square vertex indicates a (C)EDM operator.

are additionally suppressed by an extra light-quark mass (see Eq. (5.20)). In Fig. 5.4 the relevant Feynman diagrams for the operator mixing among O_3 and O_4 at leading order in α_s are shown. Their calculation only differs in the arrangement of the $SU(3)$ generators and can be related through

$$T^A T^B T^A = T^A T^A T^B - T^A \left[T^A, T^B\right] = \left(C_F + \frac{1}{4}N_c\right) T^B. \tag{5.39}$$

The contributions from bottom- and charm-quark SMEFT operators are different. Here the leading contribution to partonic dipoles (d_q, $\tilde{d}_q$) and the Weinberg operator (w) are induced by mixing during the RG evolution. The main reason is that the nuclear matrix elements of bottom and charm dipole operators are tiny. Therefore, diagrams like the ones in Fig. 5.2 do not contribute, i.e., bottom and charm quarks only enter as virtual particles in loop diagrams. At the same time, their mass is significantly below the electroweak scale. For this reason, a tree-level matching at the electroweak scale and the subsequent one-loop RG evolution [152], which must include the mixing of four-fermion operators into dipole and Weinberg operators, is sufficient (and necessary) to obtain the leading-logarithmic result. The two-loop calculation has been performed in Ref. [118] but is not used in this work, as perturbative uncertainties and higher-order corrections are generally neglected in our analysis (see the discussion in Sec. 5.7.3).

5.5 Experimental constraints

Electric dipole moments

Non-zero coefficients of the higher dimension operators in Eq. (5.8) induce in general EDMs in nucleons, atoms, and molecular systems via contributions to the hadronic Lagrangian in Eq. (5.10). Here, we summarise the status of the induced dipole moments for the systems used in our fit, namely, the electron, neutron, and mercury EDMs.

In addition to these EDMs there are also constraints from the experimental measurement of the muon EDM [153], as well as other systems with a hadronic component. The direct constraint from the current muon EDM measurement leads to constraints that are about six orders of magnitude weaker than the one obtained via virtual muon contributions to the electron EDM, and will thus not be used. Concerning other hadronic EDMs, we have checked that within our setting the experimental bounds on the radium [154] and xenon [155] EDMs are not competitive with the neutron and mercury bounds and we do not include them in the fit either.

Electron

The most recent experimental bound on the electron EDM from HfF^+ is [13], $4.1\times10^{-30}e\,\mathrm{cm}@\,90\%$ CL, improving the former upper limit by a factor of 2.7 referenced in [156]

$$|d_e| < 1.1 \times 10^{-29}\, e\,\mathrm{cm} \qquad @\ 90\%\ \text{confidence level (CL)}\,, \tag{5.40}$$

which we use here. This value was obtained using ThO molecules, neglecting any CP-violating electron–nucleon couplings. Bounds on the electron EDM have also been obtained using YbF [157].

Neutron

The simplest hadronic system used in our fit is the neutron. The most recent experimental bound on the neutron EDM is [36]

$$|d_n| < 1.8 \times 10^{-26} e\,\mathrm{cm} \qquad @\ 90\%\ \text{CL}\,. \tag{5.41}$$

The future projections estimate an improvement of the limit to $|d_n| < 10^{-27}\, e\,\mathrm{cm}$ [36]. Throughout this work, we assume that the θ_{QCD} term has a negligible effect on any EDMs and all effects arise from the Yukawa SMEFT operators.

Mercury

Significant constraints in our fit also arise from the mercury EDM. The experimental bound is [158]

$$|d_{\mathrm{Hg}}| < 7.4 \times 10^{-30} e\,\mathrm{cm} \qquad @\ 95\%\ \text{CL}\,. \tag{5.42}$$

In addition to these EDMs there are also constraints from the experimental measurement of the muon EDM [153], as well as other systems with a hadronic component. The direct constraint from the current muon EDM measurement leads to constraints that are about six orders of magnitude weaker than the one obtained via virtual muon contributions to the electron EDM, and will thus not be used. Concerning other hadronic EDMs, we have checked that within our setting the experimental bounds on the radium [154] and xenon [155] EDMs are not competitive with the neutron and mercury bounds and we do not include them in the fit either.

Collider observables

The SMEFT couplings in the Lagrangian in Eq. (5.8) do not only induce EDMs, but also affect the production cross sections and decay branching ratios of the Higgs boson. In this section we give an overview of the most important effects; the actual numerical implementation of the LHC constraints is discussed in Sec. 5.6. The main effects are captured by considering modifications of the gluon fusion production cross section ($gg \to h$) and the $h \to \gamma\gamma$ branching ratio (both are one-loop induced both in the SM and in our setup), as well as of the branching ratios to fermions observed by ATLAS and CMS ($h \to b\bar{b}$, $h \to c\bar{c}$, $h \to \tau\tau$, $h \to \mu\mu$), and the total decay width of the Higgs. The strongest constraints on the τ WCs are obtained from the angular distribution analysis of the $h \to \tau\tau$ measurement by CMS [159]. It is convenient to parameterise these modifications in terms of the parameters

$$r_{f,\pm} \equiv \frac{v}{\sqrt{2}m_f}\frac{v^2}{\Lambda^2}C_{fH\pm}\,. \tag{5.43}$$

Using Eq. (5.9), we can readily translate $r_{f,\pm}$ to the κ-framework parameters, i.e., $\kappa_f \cos\phi_f = 1 - r_{f,+}$ and $\kappa_f \sin\phi_f = -r_{f,-}$.

The deviation from the SM gluon fusion cross section or the decay to gluon-induced light jets can be effectively captured by (see Ref. [14] for details)

$$R_{gg} \equiv \frac{\sigma(gg \to h)}{\sigma(gg \to h)_{\rm SM}} = \left(\Big|\sum_q \big(1 - r_{q,+}\big)A(\tau_q)\Big|^2 + \Big|\tfrac{3}{2}\sum_q r_{q,-}B(\tau_q)\Big|^2\right)\Big/\Big|\sum_i A(\tau_q)\Big|^2\,, \tag{5.44}$$

where we have defined $\tau_q \equiv 4\,m_q^2/M_h^2 - i\varepsilon$, the sum runs over all quark flavours $q = u, d, s, c, b, t$, and the fermionic one-loop functions are given by

$$A(\tau) = \frac{3\tau}{2}\left(1 + (1-\tau)\arctan^2\frac{1}{\sqrt{\tau - 1}}\right), \qquad B(\tau) = \tau\arctan^2\frac{1}{\sqrt{\tau-1}}\,. \tag{5.45}$$

Similarly, the modification of the Higgs decays into two photons with respect to the SM reads

$$\begin{aligned} R_{\gamma\gamma} &\equiv \frac{\Gamma(h \to \gamma\gamma)}{\Gamma(h\to\gamma\gamma)_{\rm SM}} \\ &= \frac{\Big|A_W + \frac{1}{6}\sum_f Q_f^2 n_c(f)\big(1 - r_{f,+}\big)A(\tau_f)\Big|^2 + \Big|\frac{1}{4}\sum_f Q_f^2 n_c(f) r_{f,-}B(\tau_f)\Big|^2}{\Big|A_W + \frac{1}{6}\sum_f Q_f^2 n_c(f)A(\tau_f)\Big|^2}\,, \end{aligned} \tag{5.46}$$

where the sums run over all charged fermions f with $n_c(f) = 3$ for quarks and $n_c(f) = 1$ for leptons, and the bosonic contribution is given by

$$A_W = -\frac{1}{8}\left(2 + 3\,\tau_W + 3\,\tau_W\,(2-\tau_W)\arctan^2\frac{1}{\sqrt{\tau_W - 1}}\right)\,, \tag{5.47}$$

with $\tau_W = 4M_W^2/M_h^2 - i\varepsilon$. We keep the modifications of the Higgs coupling to WW and ZZ bosons unmodified, as the contributions from Yukawa operators are loop induced compared to the tree-level contributions already present at the dimension-four level. Moreover, $h \to Z\gamma$ is omitted as its decay width is suppressed by a smaller coupling compared to $h \to \gamma\gamma$.

The signal strengths of searches for Higgs decays to fermions are also affected by the corresponding modifications of the partial widths, namely:

$$R_{ff} \equiv \frac{\Gamma(h\to ff)}{\Gamma(h\to ff)_{\text{SM}}} = (1 - r_{f,+})^2 + r_{f,-}^2\,. \tag{5.48}$$

As of now, the ATLAS and CMS collaborations have observed Higgs decays into $f = b, c, \tau, \mu$. However, the modifications of the partial widths to any fermion affect the total width of the Higgs via

$$\frac{\Gamma^{\text{tot}}}{\Gamma^{\text{tot}}_{\text{SM}}} = 1 + \sum_f (R_{ff} - 1)\text{Br}(h\to\bar{f}f)_{\text{SM}} + \sum_{X=gg,\gamma\gamma}(R_X - 1)\text{Br}(h\to X)_{\text{SM}}\,, \tag{5.49}$$

which in turn affects all its branching ratios, i.e., all the signal strength for Higgs searches. The SM branching ratios for the light flavors are estimated by $\text{BR}(h\to\bar{q}q)_{\text{SM}} = \text{BR}(h\to\bar{b}b)_{\text{SM}}{m_q^2}/{m_b^2}$ for $q = u, d$ and $\text{BR}(h\to\bar{e}e)_{\text{SM}} = \text{BR}(h\to\bar{\mu}\mu)_{\text{SM}}{m_e^2}/{m_\mu}.{}^2$.

We conclude this section with some remarks concerning the convergence of the SMEFT expansion and the potential impact of dimension-eight operators. The issue arises because the squared amplitude enters the expression (5.48), leading to terms proportional to $1/\Lambda^4$ in R_{ff} that we keep in our numerics. What would be the impact of including dimension-eight Yukawa operators (of the generic form $Q^{(8)} \sim (H^\dagger H)^2\bar{Q}_L H C_{qH} q_R$) in the amplitude? While this question is hard to answer quantitatively without actually performing the analysis, the following arguments suggest that the impact would result only in minimal changes on the bounds of the dimension-six coefficients.

First, note that this issue concerns only the real parts of the WCs. As there is no interference with the SM in the CP-odd part of the amplitude, such dimension-eight terms would be of order $1/\Lambda^8$. The first term on the right side of Eq. (5.48), on the other hand, would be changed to

$$(1 - r_{f,+})^2 \to 1 - 2C^{(6)}\frac{v}{\sqrt{2}m_f}\frac{v^2}{\Lambda^2} + \big(C^{(6)}\big)^2\frac{v^2}{2m_f^2}\frac{v^4}{\Lambda^4} - C^{(8)}\frac{v}{\sqrt{2}m_f}\frac{v^4}{\Lambda^4} + \mathcal{O}\big(\Lambda^{-6}\big)\,. \tag{5.50}$$

Here, $C^{(6)}$ and $C^{(8)}$ denote generic dimension-six and dimension-eight WCs, respectively. We see that the additional last term in Eq. (5.50) is parameterically suppressed with respect to the linear dimension-six term by a factor of v^2/Λ^2, and with respect to the quadratic dimension-six term by a factor of m_f/v. A potential problem arises if the term quadratic in $C^{(6)}$ dominates the fit. A direct comparison between the last two terms in Eq. (5.50), under the "EFT assumption" $C^{(6)} \sim C^{(8)}$, shows that the dimension-eight contribution will be subleading as long as $C^{(6)} > \sqrt{2}m_f/v$. We will see in Fig. 5.5 that this condition is clearly satisfied for all fermions apart from the top-quark. While this is only a rough estimate, we interpret this as an indication that the impact of the dimension-eight terms on the fit would be tiny. By contrast, Fig. 5.6 shows that for the top-quark $C_{tH+} \lesssim 3$, which is larger than $\sqrt{2}m_t/v \sim 1$, such that for values of $C^{(8)} \sim 9$ the dimension-eight term would contribute significantly to the fit. While this required value of $C^{(8)}$ is close to the perturbativity limit, we conclude that the EFT expansion in the collider observables might not work as well for the top-quark as it does for all other fermions. CP-odd contributions, on the other hand, are not expected to receive large corrections from dimension-eight operators for any of the fermions, as discussed above.

5.6 Global Analyses with GAMBIT

Having obtained in the previous sections the expressions for the relevant observables, EDMs, Higgs production cross sections (σ), and branching ratios (BR) decay widths, we now combine the constraints on the considered WCs in a global analysis. For this purpose we use the `GAMBIT` (Global and Modular BSM Inference Tool) global fitting framework [145] to calculate a combined likelihood based on these two sets of constraints. As the name suggests, `GAMBIT` consists of a suite of independent modules that are connected via a central database, allowing users to easily mix and match different components as needed. It includes a range of statistical and computational tools for performing global fits of theoretical models to experimental data, such as several sampling algorithms and likelihood calculations. A big variety of external programs for performing computations of observables is included as well.

In this section, we will go through the setup used in this chapter in some detail. As an example, we will only consider the electron WCs for simplicity. Extending to quarks requires the inclusion of the RGE and the effective ggh-coupling. The `odeint` library within `Boost` project, the `gsl_integration` module of the GNU Scientific Library [160] and the Eigen library [161] can be used for the implementations. To create a new model, it has to be registered in the central model data file

```
config/models.dat (yaml)
CPVYukawas:
```

Comments on the model can be made after the vertical bar. The model parameters are defined in a new header file as

```c++
Models/include/gambit/Models/CPVYukawas.hpp (c++)
#define MODEL CPVYukawas
  START_MODEL
  DEFINEPARS(CeHm, CeHp, ...) // add all 18 parameters
#undef MODEL
```

Note that in newer versions, a model machine GUM was implemented to generate GAMBIT from Lagrangian-Level definitions [162]. However, we use version 1.4.3. The theoretical model descriptions and the respective experimental data are stored in the modules also named "Bits". For the collider observables, we make use of the preexisting ColliderBit module [146] while we create the new LowEBit module[1] to include EDMs. A parameter YAML file is called with GAMBIT in which the user initialises model constants or specifies ranges for varied parameters. Also, observables, their calculation description and the sampling method are declared there.

LowEBit module

In [145], details on the creation of a new module and usage of GAMBIT in general are presented. When setting up a module, two header files are required to define the variables of the model, the types header and the rollcall header. The former defines classes for the WCs of the CP-violating operators and (C)EDMs.

```c++
LowEBit/include/gambit/LowEBit/LowEBit_types.hpp (c++)
class CPV_WC_l{
  CPV_WC_l();
  double Ce, Cmu, Ctau;};
class dl{
  dl();
  double e, mu, tau;};
```

The result variables used to scan over the parameter space are necessarily floating point numbers. The rollcall header defines and organises the model capabilities. They are the quantities calculated by module or backend functions.

```c++
LowEBit/include/gambit/LowEBit/LowEBit_rollcall.hpp (c++)
#include gambit/LowEBit/LowEBit_types.hpp
#define MODULE LowEBit
#define CAPABILITY CPV_Wilson_coeff_l
START_CAPABILITY
  #define FUNCTION CPV_Wilson_l
    START_FUNCTION(CPV_WC_l)
    ALLOW_MODELS(CPVYukawas)
  #undef FUNCTION
#undef CAPABILITY
```

[1]The LowEBit module is, however, not accessible through the publicly released GAMBIT versions.

```
#define CAPABILITY EDM_para
START_CAPABILITY
  #define FUNCTION EDM_ThO
    START_FUNCTION(double)
    DEPENDENCY(dl)
    ALLOW_MODELS(CPVYukawas)
  #undef FUNCTION
#undef CAPABILITY
#define CAPABILITY lnL_EDM_para
START_CAPABILITY
  #define FUNCTION lnL_EDM_ThO
    START_FUNCTION(double)
    DEPENDENCY(EDM_para, double)
  #undef FUNCTION
#undef CAPABILITY
#undef MODULE
```

GAMBIT makes a lot of use of macros to simplify and standardise the declaration and registration of capabilities and functions. This enhances code efficiency by minimising repetitive code. The EDM_ThO function uses the WC values calculated in the CPV_Wilson_l function which is why the CPVYukawas model needs to be linked. The calculation of the log-likelihood only requires its result. Interfaces with backends are declared in the rollcall header but are only relevant for us in the ColliderBit since we calculate the likelihoods from EDMs directly. Similar to the model, these capabilities are registered in a capabilities data file

```
config/capabilities.dat (yaml)
CPV_Wilson_coeff_l:
EDM_para:
lnL_EDM_para:
```

Again, comments can be made after the vertical bar. The actual function declarations are given in source files. They contain the initial conditions (5.22)-(5.24), the log-likelihood calculations (5.51) and in the hadronic case, also the renormalisation group evolution. Diamagnetic EDMs other than that of mercury, ^{129}Xe, ^{211}Rn and ^{225}Ra, are also included but consistently give weaker constraints.

```
LowEBit/src/LowEBit.cpp
#include "gambit/LowEBit/LowEBit_rollcall.hpp"
//load the numerical values for masses, BRs, etc.
#include "gambit/LowEBit/input.h"
//declare the L1-L7 functions (see Eqs. (5.33)-(5.40)
#include "gambit/LowEBit/LoopFunctions.h"

static double Ce3[9]; //contains the WCs at Mh for the charged SM fermions
// set the WC initial values at the EW scale
void initialise(double muH, double Lambda){
```

```
  static bool first = true;
  // calculate once as loop functions do not change
  if(first){
    LoopFunctions l;
    for(int i = 0; i<9; ++i){
      int c[9] = {0};
      cs[i] = 1;
      Ce3[i]=l.C3e('e',muH,Lambda,cs);}
    first = false;}
// calculate contributions to the WC from all fermions
void CPV_Wilson_l(CPV_WC_l &result){
  using namespace Pipes::CPV_Wilson_l;
  double Lambda = 1000.0;
  initialise(Mh,Lambda);
  double ClH[9] = {(*Param["CeHm"]),...,(*Param["CtHm"])};
  for(int i = 0; i<9; i++){
    result.Ce = result.Ce + Ce3[i]*ClH[i];
  }}
// compute electron EDM from the thorium-oxide EDM
void EDM_ThO(double &result){
  using namespace Pipes::EDM_ThO;
  CPV_WC_l c = *Dep::CPV_Wilson_Coeff_l;
  result = sqrt(2.)*gf*(-1.)*me*c.Ce*gev2cm;}
// compute log-likelihood assuming gaussian distribution
void lnL_EDM_ThO_gaussianStep(double &result){
  using namespace Pipes::lnL_EDM_ThO;
  double mu = 0, sig = 4.0E-30;
  result = -1./2*pow((abs(*Dep::EDM_l) - mu)/(sig),2);}
```

In each function part of registered capabilities the usage of the safe `Pipes` pointer is necessary to exchange information between other functions and backends. We use an auxiliary `initialise` function that calculates the renormalisation group evolution for a given new physics scale only once at the beginning of the sampling procedure with a static boolean. To compute a likelihood from the EDM measurements, we assume their experimental uncertainties σ_{exp} to be Gaussian distributed, yielding the likelihoods ($\log\mathcal{L}$)

$$\chi^2_X = -2\log\mathcal{L}_X = \frac{\left(d_X(2\,\text{GeV}) - d_X^{\text{exp}}\right)^2}{\sigma^2_{X,\text{exp}}}\,, \tag{5.51}$$

with $X = n$, e, Hg. The uncertainties $\sigma_{X,\text{exp}}$ are obtained from the upper limits given in Eqs. (5.40), (5.41), and (5.42) by assuming zero central values for d_X^{exp}.

ColliderBit module

In this module, a set of files similar to the LowEBit module is dedicated to Higgs physics. The collider likelihoods are taken from the HiggsSignals_2.5.0 and HiggsBounds_5.8.0 codes [163, 164], written in Fortran, interfaced with the ColliderBit module [146] of GAMBIT.

```
Backends/include/gambit/Backends/frontends/HiggsSignals_2_5_0.hpp
BE_FUNCTION(HiggsSignals_LHC_Run1_combination, void, (double&,...),
    "run_higgssignals_lhc_run1_combination_",
    "run_HiggsSignals_LHC_Run1_combination")
BE_FUNCTION(HiggsSignals_STXS, void, (double&,...),
    "run_higgssignals_stxs_", "run_HiggsSignals_STXS")
BE_FUNCTION(HiggsBounds_neutral_input_properties_HS, void,
    (double*,double*,double*), "higgsbounds_neutral_input_properties_",
    "HiggsBounds_neutral_input_properties_HS")
BE_FUNCTION(HiggsBounds_neutral_input_effC_HS, void, (double*,...),
    "higgsbounds_neutral_input_effC_", "HiggsBounds_neutral_input_effC_HS")
BE_ALLOW_MODELS(CPVYukawas)
```

The backend function macro has five parameters. A custom function name, void as a function type, the types of the function parameters which need to match the types in the backend module, the exact symbol name as in the backend module and a custom capability name. Currently, GAMBIT can communicate with backends written in c c++ and Fortran. The translation of the latter is done by a parsing script written in Python. This works for most simple data types, but differences arise, for example with arrays. In GAMBIT, a class Farray, also present in ColliderBit is included.

HiggsSignals comprises three modules that utilize Higgs measurement from the LHC to calculate likelihoods. Each module calls HiggsBounds to determine the production cross sections and branching ratios within our SMEFT model, and to obtain the signal strengths implemented in the modules. Specifically, a backend function, designed for a setup with modified effective couplings, is employed.

The first module HiggsSignals_LHC_Run1_combination calculates a likelihood for Run 1 Higgs measurements using a set of signal strengths provided by the ATLAS and CMS combination of Run 1 data [165]. In this module, the signal strengths are "pure channels" wherein one decay channel is combined with one specific production channel, i.e., $\mu_i^f = (\sigma_i \mathrm{BR}^f)/(\sigma_{i,\mathrm{SM}}\mathrm{BR}^f_{\mathrm{SM}})$ with i and f indicating different production modes (ggh, VBF, Wh, Zh, tth) and decay channels (ZZ, WW, $\gamma\gamma$ $\tau\tau$, $b\bar{b}$), respectively. Run 1 data are sensitive to 20 such signal strengths. The (log)likelihood is then obtained from

$$\chi^2 = (\boldsymbol{\mu} - \boldsymbol{\mu}^{\mathrm{exp}})^T C_{\mathrm{cov}}^{-1} (\boldsymbol{\mu} - \boldsymbol{\mu}^{\mathrm{exp}})\,, \tag{5.52}$$

where $\boldsymbol{\mu}$ are the vectors containing the 20 signal strengths computed as a function of the SMEFT WCs, $\boldsymbol{\mu}^{\rm exp}$ are the corresponding experimental combinations, and the superscript "T" denotes transposition. The matrix $C_{\rm cov}$ is the signal-strength covariance matrix describing the uncertainties of and correlations among the signal strengths.

For Run 2 measurements, `HiggsSignals` provides two modules to compute a likelihood, one that uses the simplified template cross section measurements (STXS) `HiggsSignals_STXS` [166] and another that uses the peak-centreed method. In our analysis, we primarily use the former, as the peak-centreed is considerably slower in computation time by almost an order of magnitude and has also less constraining power, as we have checked explicitly. However, we make the exception in which we do use the peak-centreed-method module for the two $h \to \mu\mu$ analyses, which contain a total of 34 peak measurements [167, 168]. Each signal strength is a combination of various production modes, which are weighted by the corresponding experimental efficiency (ϵ_i) accounting for the detector's ability to identify signal events, i.e.,

$$\mu = \frac{\sum_j^N (\sigma \cdot {\rm BR})_j \epsilon_j}{\sum_j^N (\sigma^{\rm SM} \cdot {\rm BR}^{\rm SM})_j \epsilon_j^{\rm SM}} \,. \tag{5.53}$$

In our analysis, we include the signal strengths of 56 measurements originating from experimental searches from June 2021 [169–188]. The corresponding (log)likelihood is then obtained in an analogous manner as for the Run 1 data in Eq. (5.52). The SM predictions for the cross sections are obtained through a fit to the predictions from Yellow Report 4 [166].

Similar to the `LowEBit` module, the capabilities are registered in the rollcall header. We compute the log-likelihood within one function. The calculation of the signal strengths and the χ^2 value is performed by the respective backend functions.

```
ColliderBit/include/gambit/ColliderBit/ColliderBit_Higgs_rollcall.hpp
#define CAPABILITY LHC_Higgs_LogLike
START_CAPABILITY
#define FUNCTION calc_HS_LHC_LogLike_CPVYukawas
  START_FUNCTION(double)
  ALLOW_MODELS(CPVYukawas)
  BACKEND_REQ(HiggsBounds_neutral_input_effC_HS, (libhiggssignals), void,
      (double, ...)) //a double for each considered effective coupling
  BACKEND_REQ(HiggsBounds_neutral_input_properties_HS, (libhiggssignals),
      void, (double, double, double))
  BACKEND_REQ(run_HiggsSignals_LHC_Run1_combination, (libhiggssignals),
      void, (double&, double&, double&, int&, double&))
  BACKEND_REQ(run_HiggsSignals_STXS, (libhiggssignals), void, (double&,
      double&, double&, int&, double&))
  BACKEND_OPTION( (HiggsSignals, 2.5.0), (libhigssignals))
  BACKEND_OPTION( (HiggsBounds, 5.8.0), (libhigsbounds))
#undef FUNCTION
```

```
#undef CAPABILITY
```

We only show the entries relevant for our setup. The implementation of the log-likelihood function is presented in the following source file. Essentially, the effective couplings, alluding to the backend function `effC`, are initialised. For the effective $h\gamma\gamma$ and hgg the one-loop functions for each flavour are calculated once at the beginning to reduce computing time. We do not show the `initialise` function here, as it is conceptually the same as in the `LowEBit` module.

```
ColliderBit/src/gambit/ColliderBit/ColliderBit_Higgs.cpp
#include "gambit/ColliderBit/ColliderBit_rollcall.hpp"

void calc_HS_LHC_LogLike_CPVYukawas(double &result){
  using namespace Pipes::calc_HS_LHC_LogLike_CPVYukawas;
  //calculate the CP even (odd) prefactors in Eqs. (5.44) and (5.46) once.
  initialise();
  double ghjee_p = -((*Param["CeHm"]))*vev*vev*vev/Lambda/Lambda/mu/sqrt(2.);
  double ghjee_s =
      1.-((*Param["CeHp"]))*vev*vev*vev/Lambda/Lambda/mu/sqrt(2.);
  // continue for all charged fermions
  // compute ghjgaga, ghjgg and GammaTot according to eqrefs by looping over
      fermions
  BEreq::HiggsBounds_neutral_input_properties_HS(&Mh, &GammaTot[0], 0);
  BEreq::HiggsBounds_neutral_input_effC_HS(&ghjss_s, &ghjss_p, ...,
      &ghjgaga[0], ...);
  double csqtot1, csqtot2;
  BEreq::run_HiggsSignals_LHC_Run1_combination(..., csqtot1, ...);
  BEreq::run_HiggsSignals_STXS(..., csqtot2, ...);
  result = -0.5*(csqtot1 + csqtot2);
  }
```

The `csqtot1` and `csqtot2` variables are calculated by reference. The other backend function parameters are not used here. Note the subtle adjustment that has to be made to the default number of Higgs bosons.

```
Backends/src/frontends/HiggsSignals_2_5_0.cpp
#include "gambit/Backends/frontends/HiggsSignals_2_5_0.hpp"
...
int nHneut = 1; // number of neutral Higgses
int nHplus = 0; // number of charged Higgses
...
```

In the public release, three neutral and one charged Higgs are assumed. The STXS and peak-centreed modules do not yield results in our case if this is not adapted. As a final note, the analysis using the angular correlation between the decay planes of two taus from Higgs decays [159] is not included in `HiggsSignals`; we have implemented it separately in the source file with a linear interpolation of the data points. As this angular analysis is not strongly correlated with any of the other branching ratio measurements, we simply add this one χ^2 value.

ScannerBit module and post-processing

Given interval ranges for n scanned parameters ScannerBit [189] provides routines to sample the n-dimensional hypercube in three distinct steps. First, a sampler chooses a value in the unit interval. This can happen randomly or with more sophisticated methods to find best fit values more efficiently. Our intention in this chapter is not to find the optimal parameter set minimising the global χ^2 but rather to scan the whole n-dimensional parameter space. Hence, we use a grid sampler and make use of parallelisation with MPI [190]. Second, the parameter set is converted using a prior depending on the desired sampling distribution. We do not prefer specific regions in the parameter space and choose a flat prior type. Third, the parameters are passed to defining functions calculating the observables, such as signal strengths or EDMs and the corresponding likelihoods based on experimental data. The total likelihood of a parameter point is computed from the sum of the χ^2 values from the EDM and LHC likelihoods. Observables, total and individual likelihoods are printed in a HDF5 [191] database files due to its high read and write performance. A configure file in YAML contains the relevant information and gets directly called with GAMBIT. Here is an example file for a single-flavour electron simulation.

```yaml
yaml_files/CPVYuk_eThOHS.yaml
Parameters:
  # define fixed values or ranges for sampled parameters
  CPVYukawas:
    CeHm:
      range: [-3.5e-05,3.5e-05]
      prior_type: flat
    CeHp:
      range: [-0.3,0.3]
      prior_type: flat
    # all other CfHx: 0.0
Printer:
  # use hdf5 for efficient post-processing
  printer: hdf5_v1
Scanner:
  # sample over a regular grid
  use_scanner: grid
  scanners:
    grid:
      plugin: grid
      like: LogLike
      grid_pts: [100,100]
```

```
   parameters: ["CPVYukawas::CeHm","CPVYukawas::CeHp"]
ObsLikes:
 # declare which observables will be included in the scan
 # all capabilities with purpose: LogLike get added to the combined LogLike
 - capability: lnL_EDM_para
   function: lnL_EDM_ThO
   purpose: LogLike
 - capability: LHC_Higgs_LogLike
   function: calc_HS_LHC_LogLike_CPVYukawas
   purpose: LogLike
   dependencies:
   - capability: HB_ModelParameters
     function: SMHiggs_ModelParameters
     module: ColliderBit
KeyValues:
 default_output_path: "runs/CPVYukawas"
```

To identify preferred regions in a subspace of the scanned parameters, we must profile over the remaining scanned parameters. We perform the profiling using `pippi` [115], which computes the lowest possible χ^2 value of each parameter point in the subspace of interest by allowing all other parameters to float simultaneously to minimise the χ^2. Internally, all data is stored in one list, which, in consequence, limits the amount of sampling points depending on the physical and virtual memory of the computing device. In our case it is at about 25 billion points. To give an estimate of required computation time, a scan including both EDM and collider observables running on up to 16 machines with eight CPUs (3.40 GHz) each takes about seven days.

When projecting onto a two-parameter subspace, the allowed regions at 68% and 95% CL correspond to the parameter space for which the difference $\chi^2 - \chi^2_{\text{best}}$ is less or equal than $\chi^2_{68\%} \approx 2.28$ and $\chi^2_{95\%} \approx 5.99$, respectively (cf. Sec. 3.3). χ^2_{best} is the χ^2 value of the best-fit point, i.e., the lowest χ^2 value. In our case the χ^2 value of the SM (all SMEFT WCs are zero) divided by the number of the included $N_{\text{d.o.f.}} = 79$ observables is $\frac{\chi^2_{\text{SM}}}{N_{\text{d.o.f.}}} = 0.83$, where we did not include the 34 peak observables from the $h \to \mu\mu$ measurements and the angular analysis of $h \to \tau\tau$; they only affect the muon and tau Yukawas, respectively. In the scans that we present, the difference between the χ^2 of the best-fit point and the SM is always less than 0.1, so we do not display the best-fit value in the plots.

5.7 Results

5.7.1 One-flavour scans

To set the stage, we first perform two-dimensional scans over the WCs of each fermion individually, with the WCs of all other fermions set to zero. The results are shown in Fig. 5.5. We allow

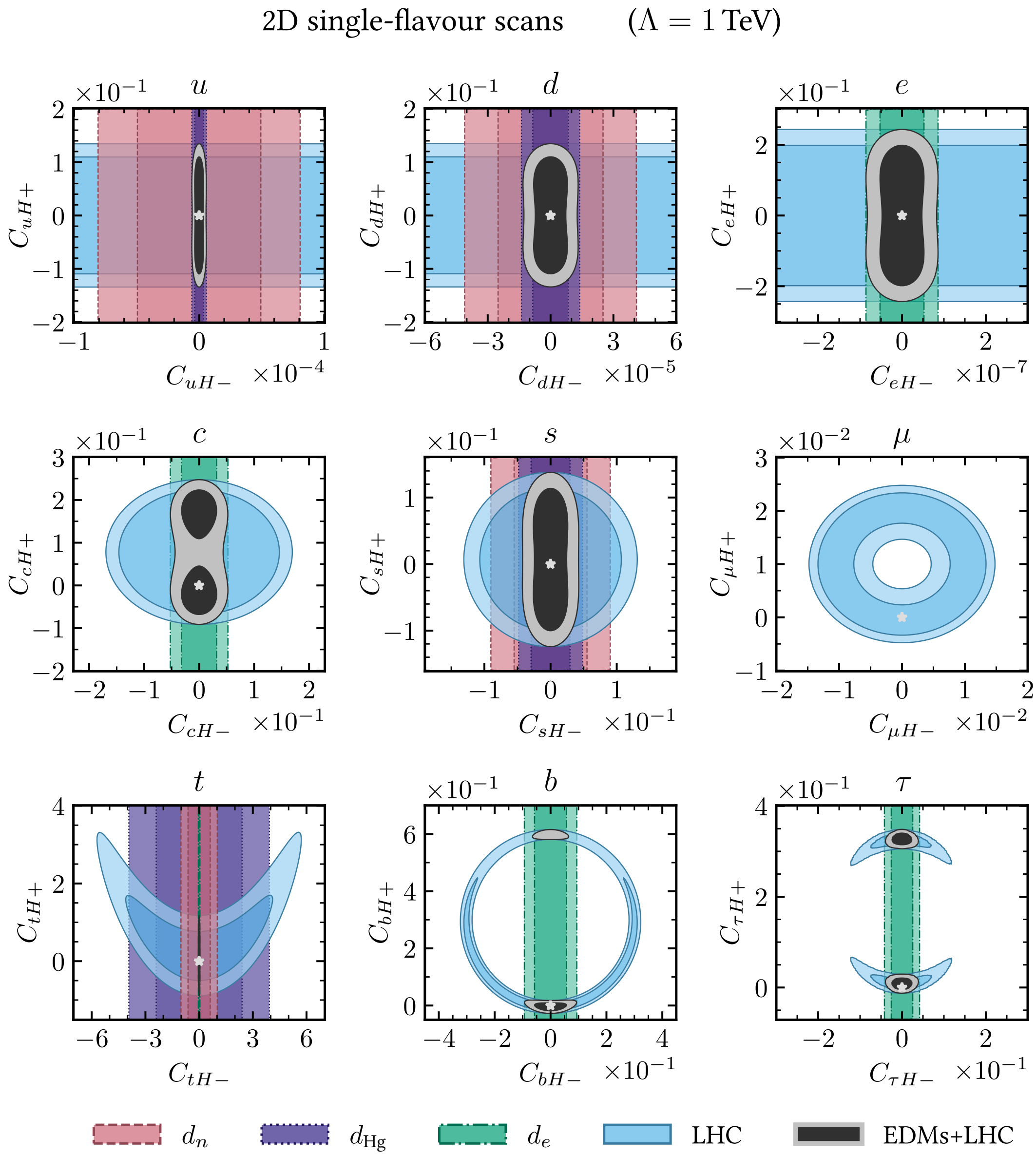

Figure 5.5: EDM and LHC constraints on CP-even (C_{fH+}) and CP-odd (C_{fH-}) Higgs Yukawa couplings assuming $\Lambda = 1$ TeV. Each plot shows the result of a 2D scan in which only the two WCs of the respective fermion are sampled. The contours represent the allowed 68% and 95% confidence regions for their respective observables. The colour coding of individual constraints is given in the legend; grey/black areas correspond to the regions allowed by the combination of all constraints. Regions allowed by an individual observable are only shown if the observable has a constraining effect on the parameter space. The sampled intervals are bounded by the perturbativity condition $|C_{fH\pm}| \leq 4\pi$.

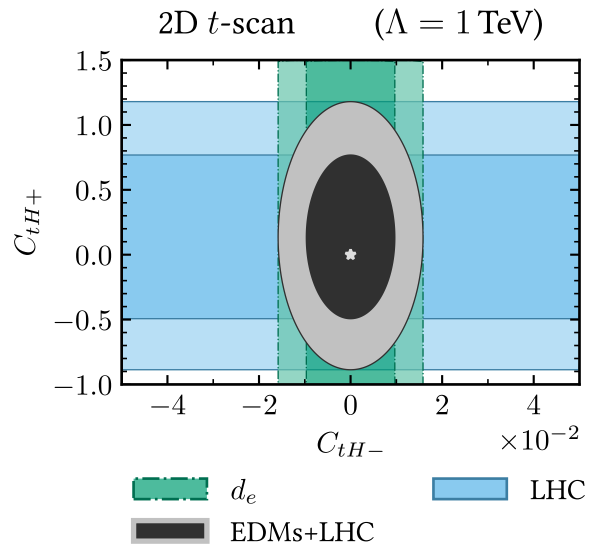

Figure 5.6: Magnification of the lower left plot of Fig. 5.5 showing the constraints on CP-even and CP-odd contributions to the top-quark Yukawa ($C_{tH\pm}$).

the WCs to float within their perturbative values, $|C_{fH\pm}| \leq 4\pi$, and fix $\Lambda = 1$ TeV in our scan. All numerical input parameters are taken from Ref. [192].

In this work, we parameterise the effects beyond the SM by the SMEFT WCs in Eq. (5.8). EDMs only constrain the imaginary part of the WCs, C_{fH-}, while LHC observables also constrain the real parts, C_{fH+}. In general, the electron EDM gives the strongest bounds on CP-violating parts of the lepton and heavy-quark (top, bottom, charm) coefficients, while the corresponding light-quark (up, down, strange) coefficients are mainly constrained by a combination of neutron and mercury EDM measurements.

- **Top**

The constraints from the modification of Higgs production in gluon fusion have the parametric dependence $\mu_{gg} = (1 - r_{t,+})^2 + r_{t,-}^2$, where we used the asymptotic values $A(\infty) = B(\infty) = 1$, valid to good approximation for the top quark, and neglected the contribution of all other quark flavours. In the same approximation, we have $\mu_{\gamma\gamma} = (1.0 + 0.27 r_{t,+})^2 + 0.17 r_{t,-}^2$. These are the dominant LHC constraints on the top couplings; note, however, that all production channels are included in our analysis. The corresponding constraints are shown in Fig. 5.5 (bottom left panel). The strongest individual bound on the CP-odd coefficient C_{tH-} arises from the electron EDM, while the constraints arising from the hadronic systems are much weaker, see Fig. 5.5. A zoomed-in version of the combined fit region is shown in Fig. 5.6.

- **Bottom, charm, tau, muon**

None of the bottom, charm, tau, and muon EDMs themselves have been measured with high precision. Consequently, EDM bounds on CP-odd Higgs couplings of the fermions arise from their virtual contributions to the electron EDM (again, the bounds arising from hadronic systems are negligible in comparison). It is remarkable that the presence of a large quadratic logarithm (see Eq. (5.32)) makes the electron EDM bound weaker than that on the top by only a factor 5 for the bottom, a factor 2 for the charm, a factor 6 for the muon, and of the same order for the tau, rather than being suppressed by the much larger factor $Q_t^2 m_t / Q_f^2 m_f = \mathcal{O}(50-500)$, expected naively [80] from the Yukawa suppression. For the bottom and charm-quarks, this strong logarithmic enhancement indicates that QCD corrections are large in these cases and should be included [148], similar to the case of hadronic dipole moments [14, 118] (see the discussion in Sec. 5.3).

Measurements at the LHC directly constrain the decay of the Higgs into bottom, charm, tau, and muon pairs. The main effect comes from the modification of the partial $h \to f\bar{f}$ widths (see Eq. (5.48)). This is a simplified picture, as modifying any Yukawa also affects the total Higgs decay width (see Eq. (5.49)), the $h \to \gamma\gamma$ decay and, for quarks, also Higgs production via gluon-fusion. This effect is largest for the bottom-quark (which dominates the SM Higgs decay width); nevertheless, we include the effect of all fermions on the total Higgs width.

Note that a negative value for the bottom Yukawa (in the sense of Eq. (5.9)) is excluded at 68% CL (bottom middle panel in Fig. 5.5). Note also that for the muon Yukawa, the recent LHC measurements are more constraining than the electron EDM by an order of magnitude [193]. Regarding tau couplings, the CMS analysis on the CP structure of the $h \to \tau\tau$ decay [159] disfavours large values of $|C_{\tau H-}|$, and the 2σ LHC constraint (blue region in lower right panel of Fig. 5.5) is split into two distinct regions. However, the constraint on $|C_{\tau H-}|$ from the electron EDM is still stronger.

• Electron, up, down, strange

The main EDM bounds on the electron and light-quark (up, down, strange) SMEFT coefficients arise from their contributions to the electron EDM and the neutron and mercury EDMs, respectively, as discussed in Sec. 5.4. Note the different impact of the neutron and mercury EDMs on the up and down coefficients due to the strong isospin dependence of the corresponding EDM predictions.

LHC bounds on the WCs for the electron and the up- and down-quarks arise from modifications of the total Higgs decay width Eq. (5.49). Indeed, we checked that the contributions to gluon fusion and $h \to \gamma\gamma$ are subleading. (For modifications of Higgs production induced by parton distribution functions, see Ref. [194].) However, the resulting constraints are very weak when compared to the SM Yukawas, as illustrated by the corresponding ratios $|r_{e,+}| \lesssim 4000$, $|r_{u,+}| \lesssim 500$, and $|r_{d,+}| \lesssim 225$. In contrast, the bound on the CP-odd strange-quark coefficient from LHC is almost competitive with the hadronic EDM bounds (central panel in Fig. 5.5).

5.7.2 Two-, three-flavour scans, and beyond

Next, we let the WCs of more than one fermion flavour float simultaneously. This allows for the cancellation of the contributions of the considered WCs to the constraining EDMs, thereby relaxing the bounds in certain regions of parameter space. There are no such cancellations possible in the collider observables because the main effect comes from partial decay widths where no interference is possible. (The small interference term between top- and bottom-quark contribution to Higgs production via gluon fusion and $h \to \gamma\gamma$ is negligibly small.) However, the bounds on the different WCs are still correlated. For instance, the Higgs decay into bottom-quark dominates the total Higgs decay width, and thus the $h \to b\bar{b}$ rate affects all branching ratios significantly. The same is true, albeit to a lesser extent, for all other Higgs decays.

- **Up and down**

In the left panel of Fig. 5.7, we show the results of a two-parameter scan over C_{uH-} and C_{dH-}. We do not scan over the corresponding CP-even WCs as they do not enter the EDM predictions. The different dependence of the neutron and the mercury EDMs on the up- and down-quark coefficients is clearly visible. With the isoscalar pion-nucleon coupling (entering the mercury EDM prediction) being subdominant, the bands of the two observables are nearly orthogonal, thus allowing setting stringent constraints on both C_{uH-} and C_{dH-}.

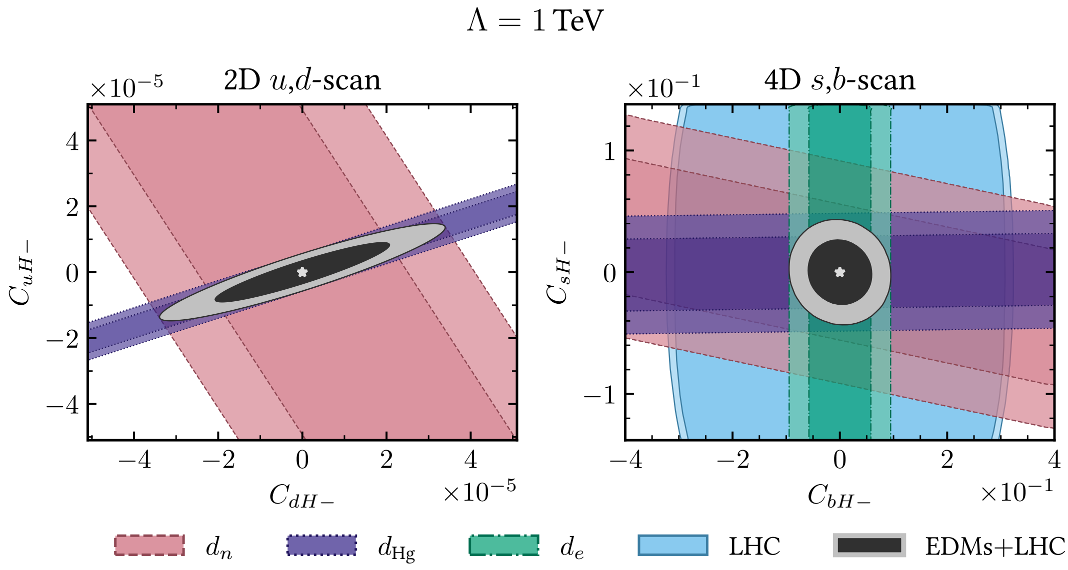

Figure 5.7: ***Left:*** Constraints resulting from the combined 2D scan of CP-odd up and down Yukawas (C_{uH-}, C_{dH-}). As the EDMs are not sensitive to the CP-even parts and the corresponding LHC constraints are weak, we do not scan over those parameters. ***Right:*** Constraints resulting from the combined 4D scan of CP-even and CP-odd bottom and strange Yukawas ($C_{bH\pm}$, $C_{sH\pm}$). Contours represent the allowed 68% and 95% confidence regions; the colour coding of individual constraints is given in the legend, and grey/black areas correspond to the combined regions. For more details see caption of Fig. 5.5.

• Bottom and strange

In the right panel of Fig. 5.7, we show the results of a four-parameter scan over $C_{bH\pm}$ and $C_{sH\pm}$ after profiling over the CP-even couplings. As we neglect the tiny strange-quark contribution to the electron EDM, the only constraint on C_{sH-} arises from the two hadronic EDMs. On the other hand, C_{bH-} receives its dominant constraint from the electron EDM, while the contributions to the hadronic EDMs are also taken into account.

We include the CP-even WCs in the scan as they are both bounded by LHC measurements. As there is no direct measurement of $h \to s\bar{s}$, the correlation between C_{sH-} and C_{bH-} results from the contributions to the total Higgs decay width. The analogous plots with CP-even WCs do not contain any additional information compared to the one-flavour scans and are thus not shown here.

• Top and bottom; top and tau; top and charm

In Fig. 5.8, we show the results of three different four-parameter scans, floating $C_{tH\pm}$ simultaneously with $C_{bH\pm}$ (first column), with $C_{\tau H\pm}$ (second column), and with $C_{cH\pm}$ (third column). The electron EDM bounds on C_{tH-} could, in principle, be lifted by two orders of magnitude compared to the single-flavour scan by choosing values close to the perturbativity limit for C_{bH-}, $C_{\tau H-}$, and C_{cH-}. However, given the LHC bounds on these parameters, the bound on C_{tH-} is weakened by only a factor of the order of five. Note also that allowing C_{tH+} to float significantly increases the allowed range of values for C_{bH+} at the 68% CL (upper left panel in Fig. 5.8). The relaxation of the bounds compared to the single-flavour fit is even more pronounced for the charm-quark (upper right panel in Fig. 5.8). In the last row, we present the constraints on the parameters C_{tH+} and C_{tH-}, with the other parameters profiled. This can be directly compared to Fig. 5.6, showing a significant relaxation of the bounds.

Interestingly, the combination of the electron EDM with LHC constraints has a profound impact on the constraint on the CP-even WCs and not only on the CP-odd ones as one would naively expect. To understand this better, we first consider the second panel from above in the first column of Fig. 5.8 showing the allowed C_{tH-}–C_{bH-} region. Here, the allowed combined region corresponds to the intersection of the electron EDM and the LHC constraint, which implies that for each allowed pair of (C_{tH-}, C_{bH-}), it is possible to find corresponding allowed values of C_{bH+} and C_{tH+} (which have been profiled out in the plot). This can easily be verified by looking at the bottom left and bottom centre panels of Fig. 5.5. By contrast, the electron EDM on its own does not constrain the C_{tH-}–C_{bH+} subspace at all, i.e., the whole parameter space of the third panel in the first column of Fig. 5.8 (C_{tH-}–C_{bH+} plot) is allowed with respect to the electron EDM. The reason being that one can always cancel the top against the bottom contributions to the EDM (see green band in the upper left panel). However, the combined EDM–LHC region is smaller than the one allowed by LHC alone, as not all values of C_{bH-} required to cancel the contributions of C_{tH-} are allowed by LHC bounds. In fact, the bottom single-flavour analysis (bottom centre panel of Fig. 5.5) indicates that roughly $C_{bH-} \approx C_{bH+}$, resulting in the much smaller allowed combined region in the 4D scan. Similar arguments apply to the plots that show the top–tau and top–charm coefficients. Regarding the case of the charm-quark, note that its contribution to the electron EDM is larger than that of the bottom-quark, while the LHC constraint is comparatively weaker, resulting in a larger allowed combined region. Finally, we remark that while the contribution to the electron EDM of the muon is similar to that of the bottom, the muon Yukawa is so strongly constrained by recent LHC measurements that no appreciable cancellation can occur, which is why we do not present this scan.

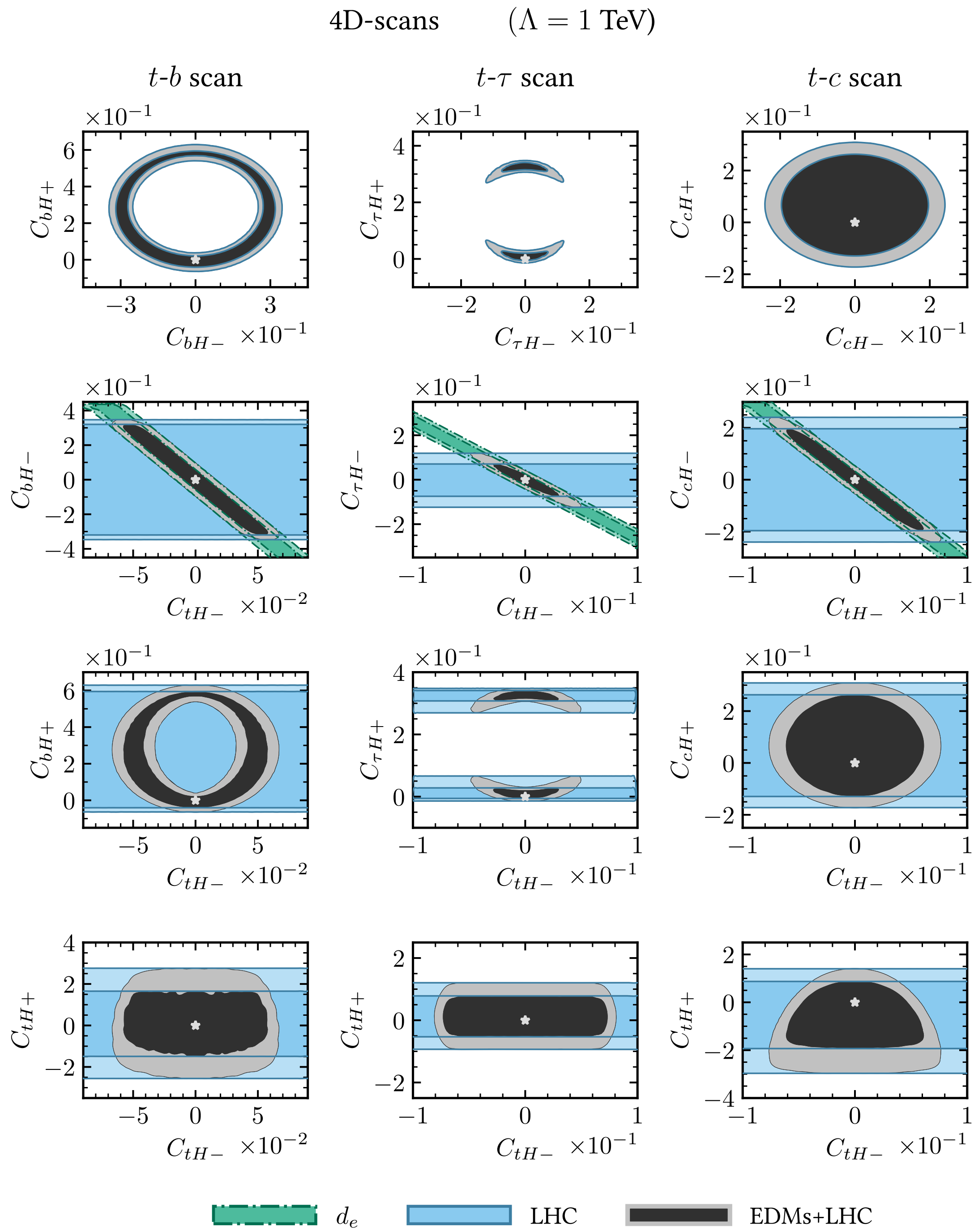

Figure 5.8: Constraints resulting from a 4D scan of top and bottom coefficients ($C_{tH\pm}$, $C_{bH\pm}$; first column), top and tau coefficients ($C_{tH\pm}$, $C_{\tau H\pm}$; second column), and top and charm coefficients ($C_{tH\pm}$, $C_{cH\pm}$; third column), assuming $\Lambda = 1$ TeV. In each plot only two parameters are shown, the remaining two are profiled over (see main text). Contours represent the allowed 68% and 95% confidence regions; the colour coding of individual constraints is given in the legend, and grey/black areas correspond to the combined regions. For details see main text and the caption of Fig. 5.5.

• **Bottom and tau**

In Fig. 5.9 we show the results of a scan of the four parameters $C_{bH\pm}$ and $C_{\tau H\pm}$. As in the previous four-parameter scans, there is an interesting interplay between EDM and LHC bounds. When considering EDM bounds only, we can always cancel the constraint if either C_{bH-} or $C_{\tau H-}$ is profiled. Hence, there are no pure EDM constraints in any but the upper centre panel where the CP-odd coefficients C_{bH-} and $C_{\tau H-}$ are displayed. In contrast, the EDM constraints cannot always be satisfied if also LHC constraints are included. In the upper left plot with the two bottom coefficients displayed, one can see that the allowed, combined region is enlarged compared to the single-flavour scan. However, for extreme values for C_{bH-}, still allowed by LHC bounds, $C_{\tau H-}$ cannot be profiled such that it compensates for the bottom contribution to the electron EDM and simultaneously still be within the 2σ-level τ LHC bounds. In contrast, C_{bH-} can be profiled such that the $C_{\tau H-}$ coefficient in the upper right plot is only bounded by LHC constraints.

Even though the tau contributions to the electron and quark EDMs are larger than those of the bottom by about a factor of $3m_\tau \log^2(m_\tau/M_h)/m_b \log^2(m_b/M_h) \approx 2$ (apparent from Eq. (5.22)), the allowed range for $C_{\tau H-}$ is so strongly bounded by LHC constraints that the tau contribution can always be fully cancelled by the bottom contribution, but not vice versa. This implies that, given current data, the combined bounds (apart from the combination $(C_{\tau H+}, C_{\tau H-})$) are more stringent than either the LHC bounds or the EDM bounds alone. The effect of the electron EDM, further restricting the parameter regions allowed by LHC data, is also clearly visible in the combined region in the lower centre panel that shows the bounds on the two CP-even coefficients C_{bH+} and $C_{\tau H+}$.

• **Charm and tau**

In Fig. 5.10 we present the results of a scan of the four parameters $C_{cH\pm}$ and $C_{\tau H\pm}$. The results are analogous to the case of bottom and tau discussed above. Note that the charm contribution to the electron EDM is larger than the bottom contribution by a factor of roughly $4m_c \log^2(m_c/M_h)/m_b \log^2(m_b/M_h) \approx 1.6$, while the LHC bounds on the charm-quark are considerably weaker than those on the bottom-quark.

• **Top, bottom, and tau** (third generation)

In Fig. 5.11 we present a scan of all six third-generation parameters $C_{bH\pm}$, $C_{\tau H\pm}$, and $C_{tH\pm}$. It is interesting to compare the results to the case in which only two out of the three flavours were included in the fit (Figs. 5.8, 5.9).

First, we focus on the set of the four panels (middle and lower row, left and centre) that show the same parameter combinations as the panels at similar positions in Fig. 5.8. We see that after profiling the remaining third-generation couplings, an "indirect" electron EDM constraint on C_{tH-} remains, although the allowed region is now significantly larger. By contrast, the "indirect"

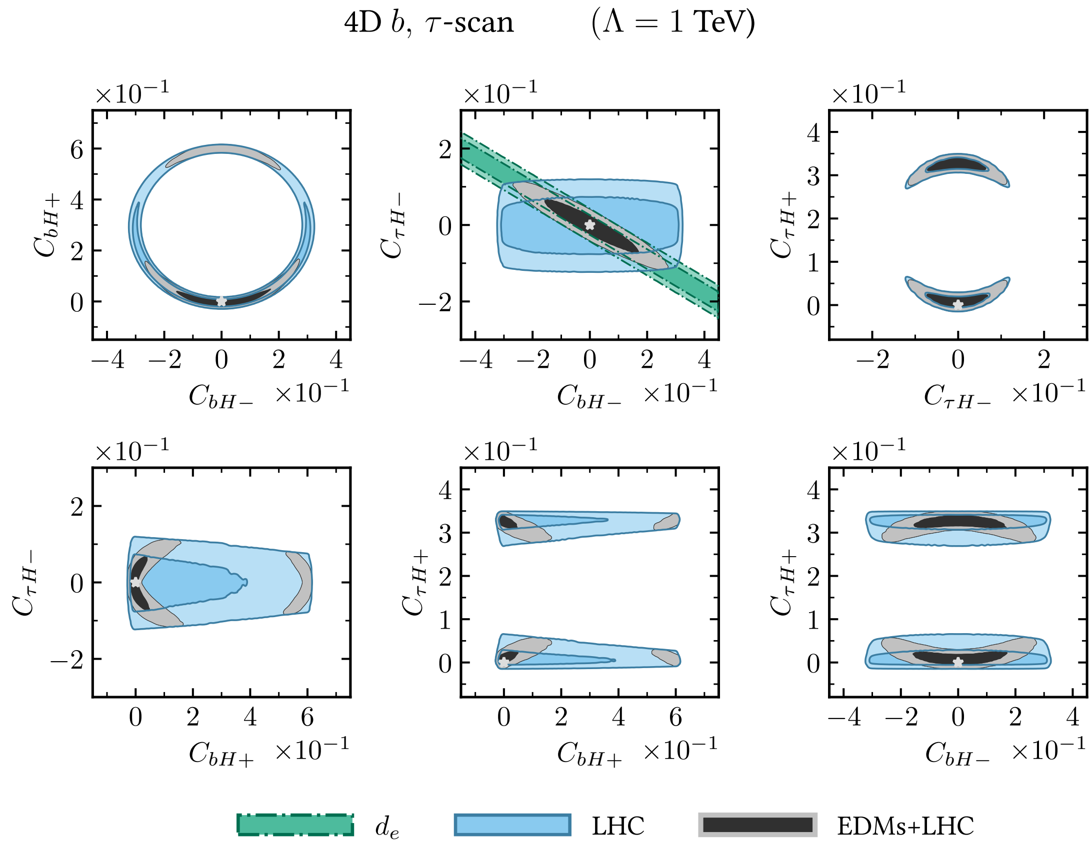

Figure 5.9: Constraints resulting from a 4D scan of bottom and τ WCs ($C_{bH\pm}$, $C_{\tau H\pm}$) assuming $\Lambda = 1$ TeV. In each plot only two parameters are shown, the remaining two are profiled over (see main text). Contours represent the allowed 68% and 95% confidence regions; the colour coding of individual constraints is given in the legend, and grey/black areas correspond to the combined regions. For details see main text and the caption of Fig. 5.5.

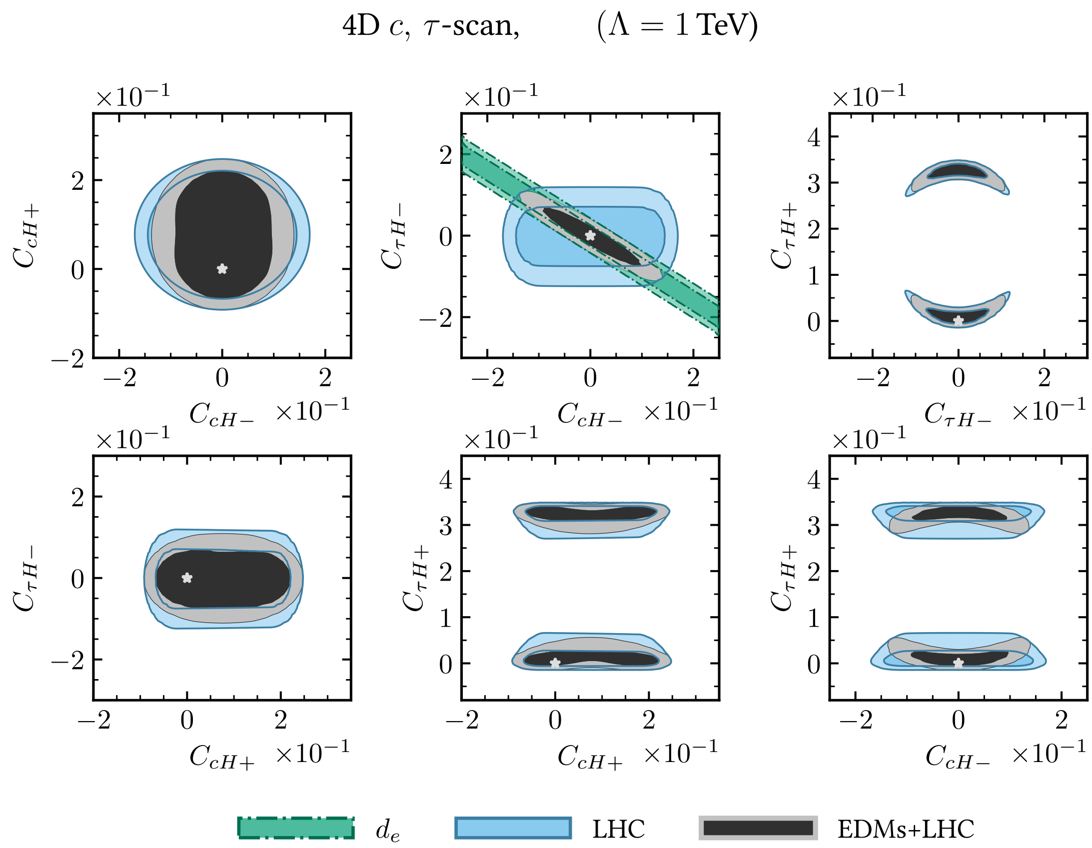

Figure 5.10: Constraints resulting from a 4D scan of charm and τ WCs ($C_{cH\pm}$, $C_{\tau H\pm}$) assuming $\Lambda = 1$ TeV. In each plot only two parameters are shown, the remaining two are profiled over (see main text). Contours represent the allowed 68% and 95% confidence regions; the colour coding of individual constraints is given in the legend, and grey/black areas correspond to the combined regions. For details see main text and the caption of Fig. 5.5.

electron EDM constraint can be lifted completely by C_{tH-} (that is only weakly constrained from LHC measurements) in the panels in the top row and centre right of Fig. 5.11, leaving only the LHC constraints. This should be compared to the corresponding, much smaller combined regions in Fig. 5.9.

The bottom right panel of Fig. 5.11 shows the constraints on both top WCs, $C_{tH\pm}$. Notice that the allowed values increased by about a factor of two for C_{tH+} and by one order of magnitude for C_{tH-} compared to the single-flavour scan (Fig. 5.6).

The large computational resources required for scans with more than six parameters prevent us from scanning over more than three flavours. Nevertheless, we can infer some results in this direction from the one-, two-, and three-flavour scans above. Specifically, we will consider how the constraints on the third-generation WCs change when including more flavours in the scans.

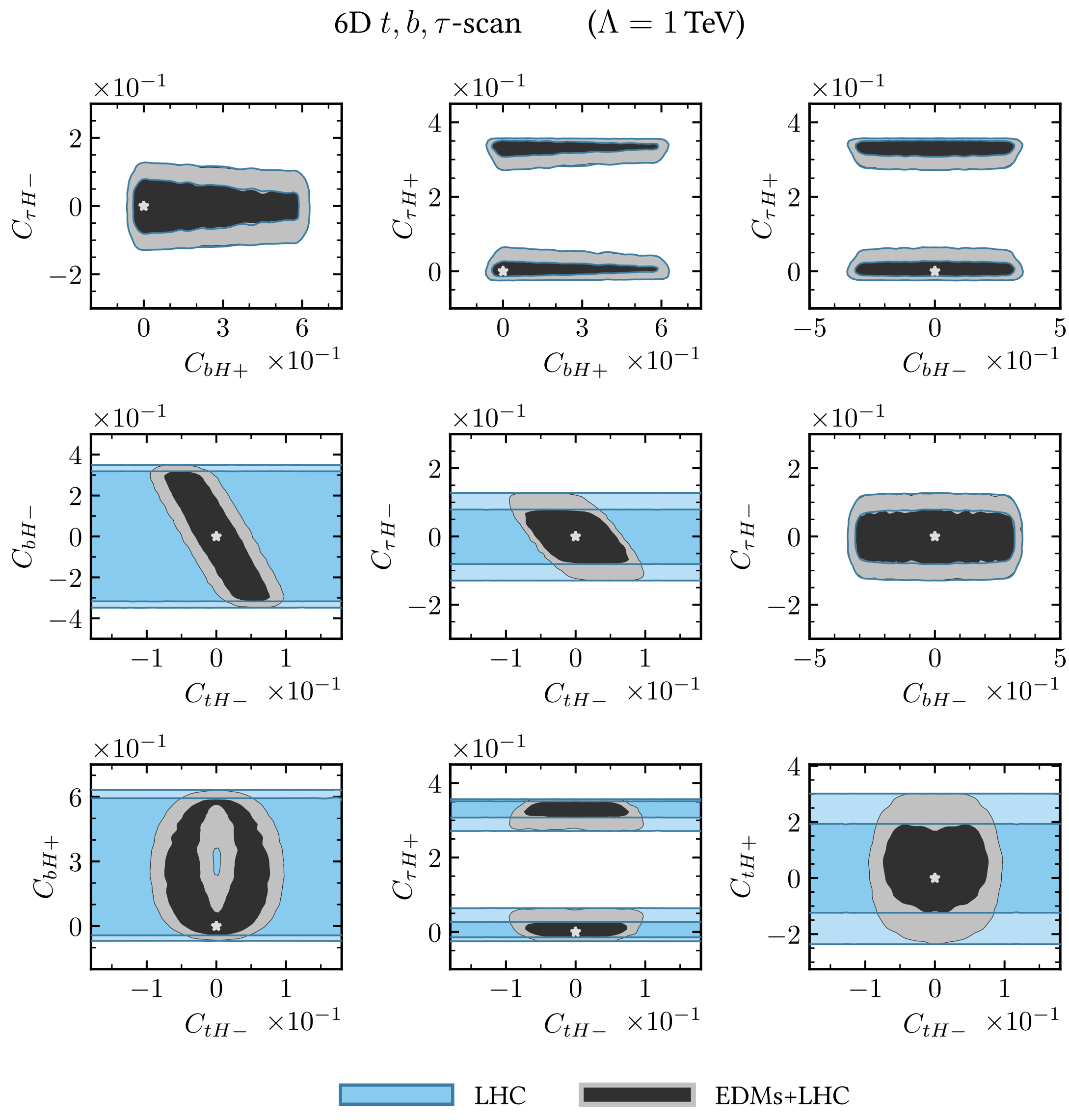

Figure 5.11: Constraints resulting from a 6D scan of top, bottom, and τ WCs ($C_{tH\pm}$, $C_{bH\pm}$, $C_{\tau H\pm}$) assuming $\Lambda = 1$ TeV. In each plot only two parameters are shown, the remaining ones are profiled over (see main text). Contours represent the allowed 68% and 95% confidence regions; the colour coding of individual constraints is given in the legend, and grey/black areas correspond to the combined regions. For details see main text and the caption of Fig. 5.5.

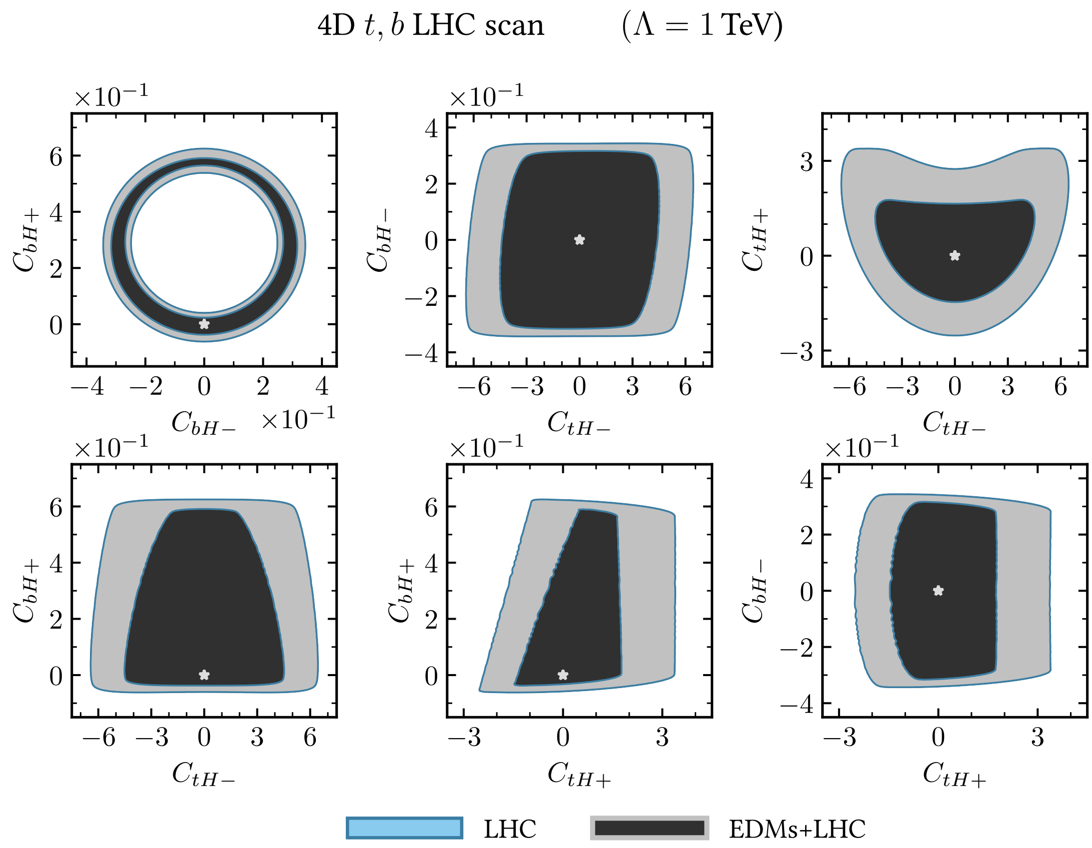

Figure 5.12: LHC constraints resulting from a 4D scan of top and bottom WCs ($C_{tH\pm}$, $C_{bH\pm}$) assuming $\Lambda = 1$ TeV. In each plot only two parameters are shown, the remaining ones are profiled over (see main text). Contours represent the allowed 68% and 95% confidence regions; the colour coding of individual constraints is given in the legend, and grey/black areas correspond to the combined regions. For details see main text and the caption of Fig. 5.5.

- **Top, bottom, (electron, light quark)**

As an example, we float $C_{tH\pm}$ and $C_{bH\pm}$ under the presumption that any contributions to EDMs can be compensated by appropriate values of the coefficients C_{eH-} and C_{qH-}, $q = u, d$, which we, however, do not scan over. In this way only LHC bounds remain, which are one to two orders of magnitude weaker for C_{tH-} with respect to the electron EDM. The results are shown in Fig. 5.12. We find that the LHC constraints on C_{tH+} and C_{bH+} are somewhat lifted compared to the single-flavour scans due to the large contribution of the bottom to the total Higgs width, while the absence of EDM bounds allows for much larger allowed ranges of C_{tH-} and C_{bH-}. The analogous results for the charm instead of the bottom couplings are shown in Fig. 5.13.

More generally, the CP-violating up, down, and electron WCs are merely and severely constrained by EDM measurements. Hence, including C_{eH-}, C_{uH-}, and C_{dH-} in a scan over the WCs of the second or third generation would allow to completely cancel any EDM

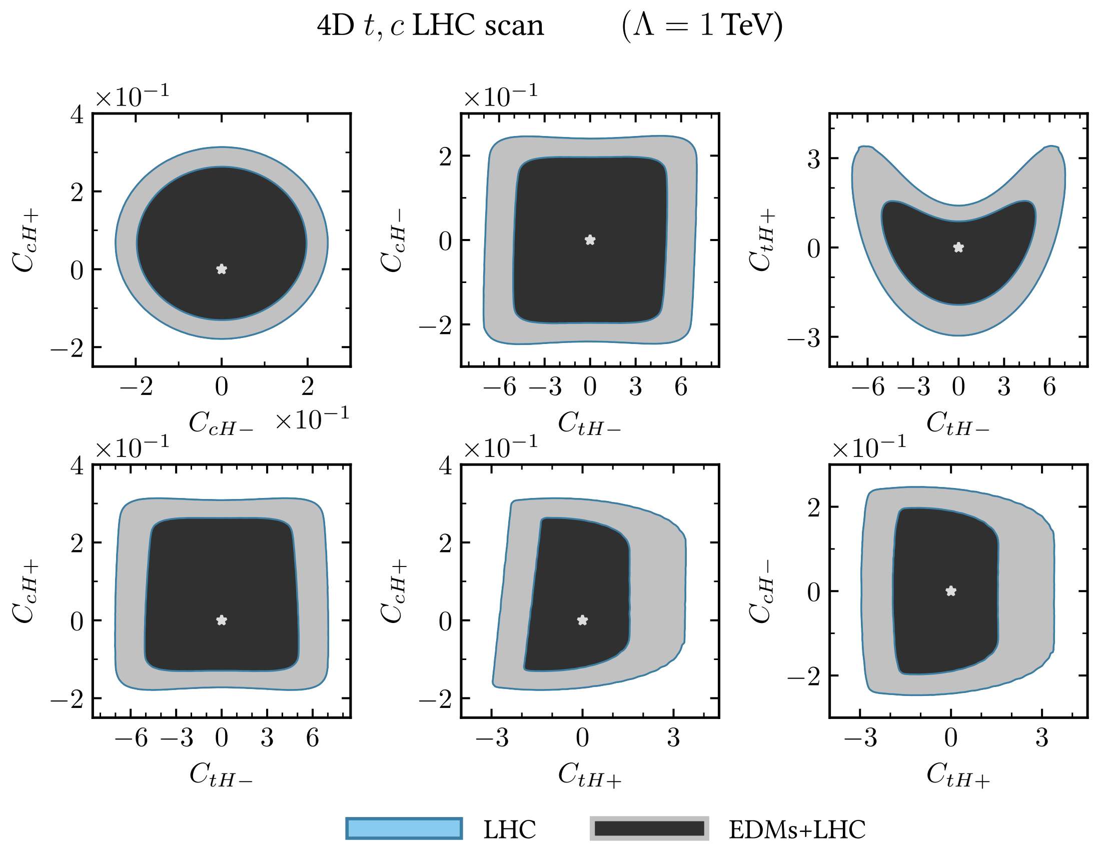

Figure 5.13: LHC constraints resulting from a 4D scan of top and charm WCs ($C_{tH\pm}$, $C_{cH\pm}$) assuming $\Lambda = 1$ TeV. In each plot only two parameters are shown, the remaining ones are profiled over (see main text). Contours represent the allowed 68% and 95% confidence regions; the colour coding of individual constraints is given in the legend, and grey/black areas correspond to the combined regions. For details see main text and the caption of Fig. 5.5.

constraints and again only LHC constraints would remain.

5.7.3 Theory uncertainties

In this work, we did not study the impact of theoretical uncertainties on the bounds on the WCs. Hence, a short discussion of these effects is in order. The relevant uncertainties are: (i) uncertainties in the hadronic matrix elements; and (ii) perturbative uncertainties.

(i) The uncertainties on the hadronic matrix elements have been shown in Sec. 3.2.1. Note that, in addition to the ranges given for the parameters, also some of the relative signs are not determined. In our numerical analysis, we have taken the central values for the hadronic matrix elements, and (somewhat arbitrarily) chosen the positive signs where they were not determined. We did not include these uncertainties in our likelihood function. In fact, no bounds at the 68% CL would result from the mercury EDM, while the neutron EDM bounds would get weaker by about a factor of 2. At 95% CL, there would also be no bound from the neutron EDM. (In Ref. [119], much smaller effects of the hadronic uncertainties have been found. This may be related to the statistical treatment of the uncertainties; in our computation we take uncertainty on the EDMs from hadronic input, $\sigma^2_{\rm had}$, to scale with the WCs.) On the other hand, the bounds on the heavy quarks (top, bottom, charm) are dominated by the electron EDM that has no hadronic uncertainties. Recall also, as discussed above, that EDM constraints become less relevant upon including more WCs in the fit, implying that the hadronic uncertainties do not (currently) play a significant role in the multi-parameter fits.

(ii) It is important to recognise that, in many cases, the perturbative uncertainties are as large as the non-perturbative uncertainties. As an example, consider the bounds on the bottom and charm WCs, studied (within the κ framework) in Ref. [118]. There it was shown that the QCD corrections are large; after inclusion of the two-loop leading-logarithmic QCD corrections, the uncertainties on the electric and chomoelectric WCs are reduced to order of 30%. We do not include the NLO corrections here, as lattice results are not available for all required matrix elements (see Refs. [195–197] for preliminary results). Maybe somewhat surprisingly, also the electron EDM bound on the CP-violating bottom and charm Yukawas receives large QCD corrections. The calculation of these effects is done in [148] but also not included in this work. No theory uncertainties are included in the LHC constraints. Note that they are partially contained in the uncertainties quoted by the experiments.

5.8 Discussion

In this work we present high-dimensional fits of the coefficients of Yukawa-type SMEFT operators to multiple EDMs and LHC data. As expected, upon inclusion of a sufficient number of WCs, all EDM constraints can be evaded by cancellations, and only LHC bounds remain. However, when considering the heavy fermions only, a nontrivial interplay between contributions remains.

There are several ways to further extend our analysis in the future. As discussed in Sec. 5.7.3, we neglect the impact of hadronic and perturbative uncertainties on our fit results. This impact can be profound in the lower-dimensional scans, and further motivates the ongoing efforts to decrease the uncertainties.

Improved experimental bounds (or discoveries), as well as the inclusion of additional EDMs such as those of proton and deuterium, once available, are expected to have a significant impact on the global fit. In particular, the different isospin dependence of the various hadronic systems will help to disentangle CP-odd Higgs couplings of the first-generation quarks. The CP structure of the heavy-fermion Yukawas can be tested more directly at present and future colliders by studying observables that are designed specifically to test the CP-odd couplings and typically require a vast amount of (expected) future data (see, e.g., Refs. [198–204]).

Finally, as explained in Sec. 5.2 where we introduce the theoretical framework for flavour-diagonal CP-violation in Higgs Yukawas, we do in general expect new flavour-violating sources to accompany beyond-the-SM CP-violation. Therefore, allowing for flavour-changing contributions within SMEFT, and including the corresponding observables would be a further extension of the current analysis. While such contributions are generically expected in realistic UV models and are expected to lead to much stronger bounds, the question is whether, given the proliferation of parameters and observables, it is not better to study selected UV models directly.

Ref. [112] presents analyses with a similar scope as ours. We briefly comment on the differences between the two papers. In Ref. [112], the κ framework is employed to perform multi-parameter fits to LHC data. The interplay of LHC data and the electron EDM bound is discussed, but no combined fit to both LHC and EDM data is performed. By contrast, constraints that arise from considerations of electroweak baryogenesis are discussed in Ref. [112]. The expression for the electron EDM (Eq. (13) in Ref. [112]) is given in numerical form and thus hard to verify. However, it seems that the gauge-boson contribution must be incorrect (either gauge-dependent or containing an implicit logarithmic dependence on the UV cutoff that is not made explicit; the cited references contain contradictory results). See our discussion in Sec. 5.4.

Chapter 6

Conclusions

The Standard Model (SM) is one of the most profound achievements in theoretical physics. It has been expanded and refined over decades, culminating in the experimental discovery of the Higgs boson. In this thesis, in chapters 2 and 3, we laid the theoretical foundations and explored the specific setups, respectively, used for our studies on CP-violating light-quark Yukawa couplings in the κ-framework in chapter 4 and for our global analyses of CP-violating contributions to all SM-Yukawa couplings in Standard Model Effective Field Theory (SMEFT) in chapter 5. Theoretical concepts of quantum field theory, CP-violation and renormalisation were introduced, and the techniques, the matching of EFTs and the renormalisation group evolution (RGE) of effective operators were demonstrated. The connections of electric dipole moments (EDM) and collider observables to the Wilson coefficients (WCs) were highlighted.

In chapter 4 we employed the simple κ-framework to compute WCs of light-quark EDMs. In this framework we laid out in detail the method of calculating the leading-order Feynman diagrams. However, for the light fermions, diagrams involving couplings between the external photon and internal W-bosons introduced gauge-dependent contributions, rendering the κ-framework inapplicable in this case. This limitation motivated the exploration of SMEFT in chapter 5, where CP-violating interactions were introduced through non-vanishing six-dimensional operators of the form $(H^\dagger H)F_L f_R H$. They modify all SM-Yukawa couplings at tree-level relating to the κ-framework expressions. Notably, for the light fermions, the leading-order contributions obtained new gauge-invariant terms stemming from dimension-five couplings. However, these introduced an ultraviolet divergent term $\log(m_H^2/\Lambda^2)$, where Λ denotes the new physics scale at which the effective operators are matched. A full RGE from the electroweak to the hadronic scale was performed, including four-fermion operators and the Weinberg operator.

Constraints on the WCs were derived from the EDMs and the Higgs production and decay processes, implemented and analysed using the Global And Modular BSM Inference Tool (GAMBIT). It combined the ColliderBit module with HiggsSignals as the backend for calculating the likelihoods of collider observables and our self-developed LowEBit module EDM related likelihoods. The ScannerBit module executed the calculations and organised the resulting combined likelihoods. We displayed constraints on the CP-violating and CP-even WCs for individual fermions or combinations thereof, offering utility in constraining parameters of beyond the Standard Model theories.

The study of the smallest scales in nature can reveal profound insights into the universe's grandest phenomena. To understand baryogenesis, we turned to symmetry-breaking effects induced by interactions of the elementary particles potentially being measured on our planet. This illustrates the deep connections between elementary particle physics and cosmology. This journey underscores our search for place and meaning in a universe that is not only knowable but also awe-inspiring in its elegance and beauty.

Appendix A

The R_ξ-gauge Lagrangian

In Eq. (5.8), we presented the Yukawa Lagrangian that includes SMEFT modification from Yukawa operators in the mass-eigenstate basis and in unitarity gauge. In our computation, we work in generic R_ξ gauge. In what follows, we present the relevant part of the Lagrangian, $\mathscr{L}_{\text{Yukawa}}$, in R_ξ gauge after rotating to the mass-eigenstate basis for the fermions. We split the Lagrangian into

$$\mathscr{L}_{\text{Yukawa}} = \sum_{f=u,d,e} \left(\mathscr{L}_{\text{dim-4},f} + \mathscr{L}_{\text{dim-5},f} + \mathscr{L}_{\text{dim-6},f}\right), \tag{A.1}$$

where

$$\begin{aligned}\mathscr{L}_{\text{dim-4},u} =& - m_u \bar{u} u - \bar{u}\left(\frac{m_u}{v} - \frac{v^2}{\sqrt{2}\Lambda^2} C_{uH+}\right) u h \\ &+ \bar{u}\left(\frac{m_u}{v} G_0 + \frac{v^2}{\sqrt{2}\Lambda^2} C_{uH-} h\right) i\gamma_5 u + \sqrt{2}\left(G^- \bar{d}_L V^\dagger \frac{m_u}{v} u_R + \text{h.c.}\right),\end{aligned} \tag{A.2}$$

$$\begin{aligned}\mathscr{L}_{\text{dim-5},u} =& + \frac{v}{2\sqrt{2}\Lambda^2}\bar{u}\left(C_{uH+}(3h^2 + G_0^2 + 2G^+G^-) + 2C_{uH-}G_0 h\right) u \\ &+ \frac{v}{2\sqrt{2}\Lambda^2}\bar{u}\left(C_{uH-}(3h^2 + G_0^2 + 2G^+G^-) - 2C_{uH+} h G_0\right) i\gamma_5 u \\ &- \frac{v}{\Lambda^2}\left(\bar{d}_L V^\dagger (C_{uH+} + iC_{uH-}) u_R h G^- + \text{h.c.}\right),\end{aligned} \tag{A.3}$$

$$\begin{aligned}\mathscr{L}_{\text{dim-6},u} =& + \frac{1}{2\sqrt{2}\Lambda^2}(h^2 + G_0^2 + 2G^+G^-)\bar{u}\left(C_{uH+} h + C_{uH-} G_0\right) u \\ &+ \frac{1}{2\sqrt{2}\Lambda^2}(h^2 + G_0^2 + 2G^+G^-)\bar{u}\left(C_{uH-} h - C_{uH+} G_0\right) i\gamma_5 u \\ &- \frac{1}{2\Lambda^2}(h^2 + G_0^2 + 2G^+G^-)\left(\bar{d}_L V^\dagger (C_{uH+} + iC_{uH-}) u_R G^- + \text{h.c.}\right).\end{aligned} \tag{A.4}$$

Here, $u = (u, c, t)$, $d = (d, s, b)$, $m_u = (m_u, m_c, m_t)$, and the $C_{uH\pm}$ can also contain flavour off-diagonal pieces. The corresponding Lagrangian for down-type quarks is obtained by the obvious interchanges $u \leftrightarrow d$, $G^+ \leftrightarrow G^-$, $V^\dagger \leftrightarrow V$, and by a reversal of sign in all terms that are odd in the Goldstone fields. Analogously, the corresponding Lagrangian for leptons is obtained from the up-type Lagrangian above by the obvious interchanges $u \to e$, $d \to \nu$, $G^+ \leftrightarrow G^-$, $V^\dagger \to 1$, and again by reversing the sign in all terms that are odd in the Goldstone fields.

Appendix B

An alternative flavour basis: real and diagonal Yukawas

There is a certain freedom of choosing the flavour basis for the SMEFT Lagrangian to use for presenting the phenomenological constraints. This freedom stems from the fact that both the dimension-four Yukawas (Y_f) and the dimension-six SMEFT coefficients (C'_{fH}) contribute to the observed masses (and mixings) of fermions. As long as this is guaranteed, any basis is equivalent. However, since a UV extension of the SM matched to SMEFT would in general induce contributions both to Y_f and C'_{fH} there is no clear notion of a "better" or a more "physical" basis for Y_f. We have thus opted to present the bounds in the mass-eigenstate basis as discussed in Sec. 5.2 (see also Ref. [109]). The advantage of this basis is that it is the one required for computations and is also directly related to the κ-framework basis (see discussion around Eq. (5.9)). Another approach would be to attempt to provide the constraints in terms of basis-independent, i.e., Jarlskog-type, invariants (see recent Ref. [205]).

In this appendix, we discuss a different choice of basis that has been used in the literature [149]. We comment on the differences and point out a consistency condition on the Wilson coefficients in this basis that has been missed in the literature. As before, our starting point is the fermion mass term in Eq. (5.2):

$$\mathscr{L}_{\text{mass}} = -\sum_{f=u,d,\ell} \frac{v}{\sqrt{2}} \bar{f}_L \left(Y_f - \frac{v^2}{2\Lambda^2} C'_{fH} \right) f_R + \text{h.c.}\,, \tag{B.1}$$

with Y_f and C'_{fH} generic, complex 3×3 matrices. Now, instead of diagonalising the full matrix in parentheses, as we did, one may choose to rotate the fermion fields by a biunitary transformation that diagonalises only the dimension-four Yukawa matrices Y_f. In other words, we rotate with the transformation matrices

$$f_L \to \hat{U}_f f_L\,, \qquad f_R \to \hat{W}_f f_R\,, \tag{B.2}$$

for $f = u, d, \ell$, such that after the rotation

$$\mathscr{L}_{\text{mass}} = -\sum_{u,d,\ell} \frac{v}{\sqrt{2}} \bar{f}_L \left(\hat{Y}_f - \frac{v}{2\Lambda^2} \hat{C}_{fH} \right) f_R + \text{h.c.}\,, \tag{B.3}$$

where now the matrices $\hat{Y}_f \equiv \hat{U}_f^\dagger Y_f \hat{W}_f$ are diagonal and real with entries that, however, *do not* correspond to the observed fermion masses. The kinetic terms of quarks are also affected by the transformation in Eq. (B.2). At this stage this means that there is a matrix $\hat{V} \equiv U_u^\dagger U_d$ in the kinetic terms. Moreover, we have defined $\hat{C}_{fH} \equiv \hat{U}_f^\dagger C_{fH} \hat{W}_f$. In general, the matrices $\hat{C}_{fH}$ are not diagonal. However, similarly to the discussion of Sec. 5.2, one can make the UV assumption that they turn out to be complex but diagonal (or ignore off-diagonal entries). This is possible if the matrices U_f, W_f simultaneously diagonalise both Y_f and C_{fH}. Below we assume that this is the case. The analysis of Ref. [149] uses this basis, i.e., $\hat{C}_{fH\pm}$ or rescalings of them, to present the phenomenological constraints on the SMEFT parameter space.

Since in general, the elements of $\hat{C}_{fH}$ contain phases, we still have not rotated to the mass-eigenstate basis. To this end we perform an additional (flavour-diagonal) rotation on the right-handed fields as in Ref. [149]:

$$f_{R,i} \to e^{i\theta_{f,i}} f_{R,i}\,, \quad f = u, d, \ell\,. \tag{B.4}$$

Note that this chiral rotation leaves the kinetic term invariant. The phases $\theta_{f,i}$ are fixed such that they absorb any phase in the corresponding $\hat{C}_{fH}$. Therefore, after the rotation

$$\mathscr{L}_{\text{mass}} = -\sum_{u,d,\ell} \frac{v}{\sqrt{2}} \bar{f}_L y_f^{\text{SM}} f_R + \text{h.c.}\,. \tag{B.5}$$

Here, the y_f^{SM} are diagonal and real matrices with entries that correspond to the observed fermion masses, i.e., we have $m_f = \frac{v}{\sqrt{2}} y_f^{\text{SM}}$, obtained from

$$y_f^{\text{SM}} \equiv \left(\hat{Y}_f - \frac{v^2}{2\Lambda^2} \hat{C}_{fH} \right) e^{i\theta_f} = \hat{U}_f^\dagger \left(Y_f - \frac{v^2}{2\Lambda^2} C_{fH} \right) \hat{W}_f e^{i\theta_f}\,. \tag{B.6}$$

The phases θ_f are thus fixed and can be computed as functions of the physical masses and the $\hat{C}_{fH}$ entries via

$$\sin\theta_{f,i} = \frac{v}{2\sqrt{2} m_{f,i}} \frac{v^2}{\Lambda^2} \hat{C}_{fH-} = \frac{v}{2\sqrt{2} m_{f,i}} \frac{v^2}{\Lambda^2} \text{Im}[\hat{U}_f^\dagger C_{fH} \hat{W}_f]\,. \tag{B.7}$$

As we have the restriction $|\sin\theta_{f,i}| \leq 1$, this gives a consistency bound on $\hat{C}_{fH-}$ or equivalently on $\text{Im}[\hat{U}_f^\dagger C_{fH} \hat{W}_f]$.

Acknowledgements

First and foremost, I would like to express my deepest gratitude to my supervisor, Prof. Joachim Brod for his endless patience and his invaluable support throughout the years of the pursuit of my doctoral studies. The approachable, direct, and immediate work environment he cultivated was truly amazing and vital to the success of this project. His constant guidance on topics like effective field theories and developing the two-loop `FORM` routine cannot be overstated. Notably, we managed to keep up the working culture despite living on different continents and the challenges posed by the pandemic.

A special thanks to Prof. Heinrich Päs for welcoming me to his research group. The regular online meetings he organised were great to closely follow other research endeavours, and his kind words of encouragement helped me finalise this thesis.

The progress of the global Yukawa fit project during my 3-month stay in Cincinnati owes much to Dr. Jonathan Cornell, whose expertise and guidance were indispensable in the efficient implementation of the `GAMBIT` setup. Working closely together with him was truly enlightening.

I feel very fortunate that Prof. Emmanuel Stamou was appointed to the TU Dortmund during my doctoral period. His expertise in topics closely related to my thesis topics was a strong asset, and I am very grateful for the discussions we had.

Special thanks are due to Tim Brune, Dominik Hellmann, Sara Krieg, Dr. Tom Steudtner and Eva-Maria Teggers for taking their time to proofread this manuscript. For the time I spent in Cincinnati, I want to thank Dr. Michele Tammaro and Ahmed Youssef for the enjoyable time we had. A special thanks goes to my current superior at the Fraunhofer IME, Dr. Judith Klein, who gave me the freedom to complete this thesis. I want to thank Jan Adam, Dr. Joachim Beerwerth, Hannes Franke, Dr. Dominik Kahl, Jan Latarius, Florian Schulz and Julius Tilly for our friendship and the hilarious memories throughout the years. I want to express appreciation to Howard Shore and other artists, and Alex O'Connor and other content creators whose creations accompanied my entire work, shaping my way of thinking. A very special thanks goes to my parents and brothers for the emotional support and unconditional love throughout my life. Words cannot express my gratitude for having my best friend, Benjamin Schäfer, and my soulmate, Katharina Skodras in my life. Their unwavering support and belief in me fill me with humility. You are all truly amazing, and I could not have achieved this without you.

References

[1] ATLAS Collaboration, *Updated coupling measurements of the Higgs boson with the ATLAS detector using up to 25 fb^{-1} of proton-proton collision data*, .

[2] T. Aoyama, M. Hayakawa, T. Kinoshita, and M. Nio, *Tenth-Order Electron Anomalous Magnetic Moment — Contribution of Diagrams without Closed Lepton Loops*, arXiv:1412.8284.

[3] X. Fan, T. G. Myers, B. A. D. Sukra, and G. Gabrielse, *Measurement of the Electron Magnetic Moment*, Phys. Rev. Lett. **130** (2023), no. 7 071801, [arXiv:2209.13084].

[4] **Super-Kamiokande** Collaboration, Y. Ashie et al., *A Measurement of atmospheric neutrino oscillation parameters by SUPER-KAMIOKANDE I*, Phys. Rev. D **71** (2005) 112005, [hep-ex/0501064].

[5] B. Pontecorvo, *Neutrino Experiments and the Problem of Conservation of Leptonic Charge*, Zh. Eksp. Teor. Fiz. **53** (1967) 1717–1725.

[6] **Planck** Collaboration, P. A. R. Ade et al., *Planck 2013 results. I. Overview of products and scientific results*, Astron. Astrophys. **571** (2014) A1, [arXiv:1303.5062].

[7] **Planck** Collaboration, P. A. R. Ade et al., *Planck 2015 results. XIII. Cosmological parameters*, Astron. Astrophys. **594** (2016) A13, [arXiv:1502.01589].

[8] J. M. Cline, *Baryogenesis*, in Les Houches Summer School - Session 86: Particle Physics and Cosmology: The Fabric of Spacetime, 9, 2006. hep-ph/0609145.

[9] D. Bodeker and W. Buchmuller, *Baryogenesis from the weak scale to the grand unification scale*, Rev. Mod. Phys. **93** (2021), no. 3 035004, [arXiv:2009.07294].

[10] W. Buchmuller, R. D. Peccei, and T. Yanagida, *Leptogenesis as the origin of matter*, Ann. Rev. Nucl. Part. Sci. **55** (2005) 311–355, [hep-ph/0502169].

[11] M. Trodden, *Electroweak baryogenesis*, Rev. Mod. Phys. **71** (1999) 1463–1500, [hep-ph/9803479].

[12] D. E. Morrissey and M. J. Ramsey-Musolf, *Electroweak baryogenesis*, New J. Phys. **14** (2012) 125003, [arXiv:1206.2942].

[13] T. S. Roussy et al., *An improved bound on the electron's electric dipole moment*, Science **381** (2023), no. 6653 adg4084, [arXiv:2212.11841].

[14] J. Brod, U. Haisch, and J. Zupan, *Constraints on CP-violating Higgs couplings to the third generation*, JHEP **1311** (2013) 180, [arXiv:1310.1385].

[15] I. Brivio and M. Trott, *The Standard Model as an Effective Field Theory*, Phys. Rept. **793** (2019) 1–98, [arXiv:1706.08945].

[16] S. Weinberg, The Quantum theory of fields. Vol. 1: Foundations. Cambridge University Press, 6, 2005.

[17] S. Weinberg, The quantum theory of fields. Vol. 2: Modern applications. Cambridge University Press, 8, 2013.

[18] M. D. Schwartz, Quantum Field Theory and the Standard Model. Cambridge University Press, 3, 2014.

[19] H. Georgi, Weak Interactions and Modern Particle Theory. 1984.

[20] M. Srednicki, Quantum field theory. Cambridge University Press, 1, 2007.

[21] M. E. Peskin and D. V. Schroeder, An Introduction to quantum field theory. Addison-Wesley, Reading, USA, 1995.

[22] C. Itzykson and J. B. Zuber, Quantum Field Theory. International Series In Pure and Applied Physics. McGraw-Hill, New York, 1980.

[23] H. Lehmann, K. Symanzik, and W. Zimmermann, *Zur formulierung quantisierter feldtheorien*, Il Nuovo Cimento (1955-1965) **1** (1955) 205–225.

[24] R. P. Feynman, A. R. Hibbs, and G. H. Weiss, *Quantum mechanics and path integrals*, Physics Today **19** (06, 1966) 89–89, [https://pubs.aip.org/physicstoday/article-pdf/19/6/89/8265270/89_1_online.p

[25] J. Zinn-Justin, Quantum Field Theory and Critical Phenomena. Oxford University Press, 06, 2002.

[26] H. Georgi, Lie Algebras in Particle Physics. CRC Press, Boca Raton, 2018.

[27] M. Hamermesh, Group theory and its application to physical problems. Dover Books on Physics Series. Dover Publications, New York, 1989.

[28] W. Fulton and J. Harris, Representation Theory, vol. 129. Springer New York, New York, NY, 2004.

[29] M. S. Sozzi, Discrete symmetries and CP violation: From experiment to theory. 2008.

[30] I. I. Bigi and A. I. Sanda, CP violation, vol. 9. Cambridge University Press, 9, 2009.

[31] H. A. Kramers, *Théorie génerale de la rotation paramagnétique dans les cristaux*, Koninklijke Akademie van Wetenschappen (1930), no. 33 959–972.

[32] I. Schur, *Neue begründung der theorie der gruppencharaktere*, Sitzungsberichte der Königlich Preußischen Akademie der Wissenschaften zu Berlin (1905) 406–432.

[33] L. Faddeev and V. Popov, *Feynman diagrams for the yang-mills field*, Physics Letters B **25** (1967), no. 1 29–30.

[34] G. 't Hooft, *Symmetry Breaking Through Bell-Jackiw Anomalies*, Phys. Rev. Lett. **37** (1976) 8–11.

[35] R. Jackiw and C. Rebbi, *Vacuum Periodicity in a Yang-Mills Quantum Theory*, Phys. Rev. Lett. **37** (1976) 172–175.

[36] **nEDM** Collaboration, G. Pignol and P. Schmidt-Wellenburg, *The search for the neutron electric dipole moment at PSI*, SciPost Phys. Proc. **5** (2021) 027, [arXiv:2103.01898].

[37] R. D. Peccei and H. R. Quinn, *CP Conservation in the Presence of Instantons*, Phys. Rev. Lett. **38** (1977) 1440–1443.

[38] A. A. Anselm and A. A. Johansen, *Can electroweak theta term be observable?*, Nucl. Phys. B **412** (1994) 553–573, [hep-ph/9305271].

[39] A. J. Long, H. H. Patel, and M. Trodden, *Electroweak vacuum angle at finite temperature and implications for baryogenesis*, Phys. Rev. D **92** (2015), no. 4 043513, [arXiv:1507.00654].

[40] P. W. Higgs, *Broken Symmetries and the Masses of Gauge Bosons*, Phys. Rev. Lett. **13** (1964) 508–509.

[41] F. Englert and R. Brout, *Broken Symmetry and the Mass of Gauge Vector Mesons*, Phys. Rev. Lett. **13** (1964) 321–323.

[42] **KamLAND** Collaboration, T. Araki et al., *Measurement of neutrino oscillation with KamLAND: Evidence of spectral distortion*, Phys. Rev. Lett. **94** (2005) 081801, [hep-ex/0406035].

[43] M. C. Gonzalez-Garcia and Y. Nir, *Neutrino Masses and Mixing: Evidence and Implications*, Rev. Mod. Phys. **75** (2003) 345–402, [hep-ph/0202058].

[44] J. A. Formaggio, A. L. C. de Gouvêa, and R. G. H. Robertson, *Direct Measurements of Neutrino Mass*, Phys. Rept. **914** (2021) 1–54, [arXiv:2102.00594].

[45] P. W. Higgs, *Spontaneous Symmetry Breakdown without Massless Bosons*, Phys. Rev. **145** (1966) 1156–1163.

[46] S. Weinberg, *A Model of Leptons*, Phys. Rev. Lett. **19** (1967) 1264–1266.

[47] J. Goldstone, *Field Theories with Superconductor Solutions*, Nuovo Cim. **19** (1961) 154–164.

[48] M. Kobayashi and T. Maskawa, *Cp-violation in the renormalizable theory of weak interaction*, Progress of Theoretical Physics **49** (02, 1973) 652–657, [https://academic.oup.com/ptp/article-pdf/49/2/652/5257692/49-2-652.pdf].

[49] R. N. Mohapatra and R. E. Marshak, *Local B-L Symmetry of Electroweak Interactions, Majorana Neutrinos and Neutron Oscillations*, Phys. Rev. Lett. **44** (1980) 1316–1319. [Erratum: Phys.Rev.Lett. 44, 1643 (1980)].

[50] S. Weinberg, *Baryon and Lepton Nonconserving Processes*, Phys. Rev. Lett. **43** (1979) 1566–1570.

[51] B. Bajc, J. Hisano, T. Kuwahara, and Y. Omura, *Threshold corrections to dimension-six proton decay operators in non-minimal SUSY SU (5) GUTs*, Nucl. Phys. B **910** (2016) 1–22, [arXiv:1603.03568].

[52] A. J. Buras, M. Nagai, and P. Paradisi, *Footprints of SUSY GUTs in Flavour Physics*, JHEP **05** (2011) 005, [arXiv:1011.4853].

[53] J. Hisano, T. Kuwahara, and Y. Omura, *Threshold Corrections to Baryon Number Violating Operators in Supersymmetric $SU(5)$ GUTs*, Nucl. Phys. B **898** (2015) 1–29, [arXiv:1503.08561]. [Erratum: Nucl.Phys.B 907, 476–478 (2016)].

[54] H. Murayama, *Nucleon decay in GUT and nonGUT SUSY models*, in 28th International Conference on High-energy Physics, pp. 1377–1382, 7, 1996. hep-ph/9610419.

[55] C. G. Bollini and J. J. Giambiagi, *Dimensional Renormalization: The Number of Dimensions as a Regularizing Parameter*, Nuovo Cim. B **12** (1972) 20–26.

[56] G. 't Hooft and M. J. G. Veltman, *Regularization and Renormalization of Gauge Fields*, Nucl. Phys. **B44** (1972) 189–213.

[57] W. A. Bardeen, A. J. Buras, D. W. Duke, and T. Muta, *Deep-inelastic scattering beyond the leading order in asymptotically free gauge theories*, Phys. Rev. D **18** (Dec, 1978) 3998–4017.

[58] J. C. Collins, Renormalization, vol. 26 of Cambridge Monographs on Mathematical Physics. Cambridge University Press, Cambridge, 1986.

[59] W. A. Bardeen, *Regularization of gauge field theories*, eConf **C720906V2** (1972) 295–298.

[60] M. S. Chanowitz, M. Furman, and I. Hinchliffe, *The Axial Current in Dimensional Regularization*, Nucl. Phys. B **159** (1979) 225–243.

[61] P. Breitenlohner and D. Maison, *Dimensional Renormalization and the Action Principle*, Commun. Math. Phys. **52** (1977) 11–38.

[62] F. Jegerlehner, *Facts of life with gamma(5)*, Eur. Phys. J. C **18** (2001) 673–679, [hep-th/0005255].

[63] S. L. Adler, *Axial vector vertex in spinor electrodynamics*, Phys. Rev. **177** (1969) 2426–2438.

[64] M. Gell-Mann and F. E. Low, *Quantum electrodynamics at small distances*, Phys. Rev. **95** (1954) 1300–1312.

[65] C. G. Callan, Jr., *Broken scale invariance in scalar field theory*, Phys. Rev. D **2** (1970) 1541–1547.

[66] K. Symanzik, *Small distance behavior in field theory and power counting*, Commun. Math. Phys. **18** (1970) 227–246.

[67] A. V. Manohar, *Introduction to Effective Field Theories*, arXiv:1804.05863.

[68] S. Weinberg, *Phenomenological Lagrangians*, Physica A **96** (1979), no. 1-2 327–340.

[69] A. Manohar and H. Georgi, *Chiral Quarks and the Nonrelativistic Quark Model*, Nucl. Phys. B **234** (1984) 189–212.

[70] D. B. Kaplan, *Effective field theories*, in 7th Summer School in Nuclear Physics Symmetries, 6, 1995. nucl-th/9506035.

[71] K. G. Wilson, *The Renormalization Group: Critical Phenomena and the Kondo Problem*, Rev. Mod. Phys. **47** (1975) 773.

[72] Y. Liao and X.-D. Ma, *An explicit construction of the dimension-9 operator basis in the standard model effective field theory*, JHEP **11** (2020) 152, [arXiv:2007.08125].

[73] K. G. Wilson, *Renormalization group and critical phenomena. 1. Renormalization group and the Kadanoff scaling picture*, Phys. Rev. B **4** (1971) 3174–3183.

[74] A. J. Buras, *Weak Hamiltonian, CP violation and rare decays*, in Les Houches Summer School in Theoretical Physics, Session 68: Probing the Standard Model of Particle Interact pp. 281–539, 6, 1998. hep-ph/9806471.

[75] S. Herrlich and U. Nierste, *Evanescent operators, scheme dependences and double insertions*, Nucl. Phys. **B455** (1995) 39–58, [hep-ph/9412375].

[76] A. J. Buras and P. H. Weisz, *QCD Nonleading Corrections to Weak Decays in Dimensional Regularization and 't Hooft-Veltman Schemes*, Nucl. Phys. **B333** (1990) 66–99.

[77] W. Buchmuller and D. Wyler, *Effective Lagrangian Analysis of New Interactions and Flavor Conservation*, Nucl. Phys. B **268** (1986) 621–653.

[78] B. Grzadkowski, M. Iskrzynski, M. Misiak, and J. Rosiek, *Dimension-Six Terms in the Standard Model Lagrangian*, JHEP **10** (2010) 085, [arXiv:1008.4884].

[79] R. Alonso, E. E. Jenkins, A. V. Manohar, and M. Trott, *Renormalization Group Evolution of the Standard Model Dimension Six Operators III: Gauge Coupling Dependence and Phenomenology*, JHEP **04** (2014) 159, [arXiv:1312.2014].

[80] G. Panico, A. Pomarol, and M. Riembau, *EFT approach to the electron Electric Dipole Moment at the two-loop level*, JHEP **04** (2019) 090, [arXiv:1810.09413].

[81] M. Pospelov and A. Ritz, *Electric dipole moments as probes of new physics*, Annals Phys. **318** (2005) 119–169, [hep-ph/0504231].

[82] T. Chupp, P. Fierlinger, M. Ramsey-Musolf, and J. Singh, *Electric Dipole Moments of the Atoms, Molecules, Nuclei and Particles*, arXiv:1710.02504.

[83] J. Engel, M. J. Ramsey-Musolf, and U. van Kolck, *Electric Dipole Moments of Nucleons, Nuclei, and Atoms: The Standard Model and Beyond*, Prog.Part.Nucl.Phys. **71** (2013) 21–74, [arXiv:1303.2371].

[84] W. Greiner and J. Reinhardt, Quantum electrodynamics. 1992.

[85] L. I. Schiff, *Measurability of Nuclear Electric Dipole Moments*, Phys. Rev. **132** (1963) 2194–2200.

[86] V. A. Dzuba, V. V. Flambaum, J. S. M. Ginges, and M. G. Kozlov, *Electric dipole moments of Hg, Xe, Rn, Ra, Pu, and TlF induced by the nuclear Schiff moment and limits on time reversal violating interactions*, Phys. Rev. A **66** (2002) 012111, [hep-ph/0203202].

[87] M. Pospelov, *Best values for the CP odd meson nucleon couplings from supersymmetry*, Phys. Lett. B **530** (2002) 123–128, [hep-ph/0109044].

[88] V. G. J. Stoks, R. Timmermans, and J. J. de Swart, *On the pion - nucleon coupling constant*, Phys. Rev. C **47** (1993) 512–520, [nucl-th/9211007].

[89] U. van Kolck, J. L. Friar, and J. T. Goldman, *Phenomenological aspects of isospin violation in the nuclear force*, Phys. Lett. B **371** (1996) 169–174, [nucl-th/9601009].

[90] V. F. Dmitriev and R. A. Sen'kov, *Schiff moment of the mercury nucleus and the proton dipole moment*, Phys. Rev. Lett. **91** (2003) 212303, [nucl-th/0306050].

[91] J. S. M. Ginges and V. V. Flambaum, *Violations of fundamental symmetries in atoms and tests of unification theories of elementary particles*, Phys. Rept. **397** (2004) 63–154, [physics/0309054].

[92] U. Haisch and A. Hala, *Sum rules for CP-violating operators of Weinberg type*, JHEP **11** (2019) 154, [arXiv:1909.08955].

[93] R. Gupta, B. Yoon, T. Bhattacharya, V. Cirigliano, Y.-C. Jang, and H.-W. Lin, *Flavor diagonal tensor charges of the nucleon from 2+1+1 flavor lattice QCD*, arXiv:1808.07597.

[94] J. Alwall, R. Frederix, S. Frixione, V. Hirschi, F. Maltoni, et al., *The automated computation of tree-level and next-to-leading order differential cross sections, and their matching to parton shower simulations*, JHEP **1407** (2014) 079, [arXiv:1405.0301].

[95] P. Nason, *A New method for combining NLO QCD with shower Monte Carlo algorithms*, JHEP **11** (2004) 040, [hep-ph/0409146].

[96] **CDF** Collaboration, T. Aaltonen et al., *Search for Higgs Bosons Produced in Association with b-quarks*, Phys. Rev. D **85** (2012) 032005, [arXiv:1106.4782].

[97] J. F. Gunion, H. E. Haber, G. L. Kane, and S. Dawson, The Higgs Hunter's Guide, vol. 80. 2000.

[98] R. K. Ellis, W. J. Stirling, and B. R. Webber, QCD and collider physics, vol. 8. Cambridge University Press, 2, 2011.

[99] **NNPDF** Collaboration, R. D. Ball et al., *Parton distributions for the LHC Run II*, JHEP **04** (2015) 040, [arXiv:1410.8849].

[100] T. Sjostrand, S. Mrenna, and P. Z. Skands, *PYTHIA 6.4 Physics and Manual*, JHEP **05** (2006) 026, [hep-ph/0603175].

[101] M. Cacciari, G. P. Salam, and G. Soyez, *The anti-k_t jet clustering algorithm*, JHEP **04** (2008) 063, [arXiv:0802.1189].

[102] T. Gleisberg, S. Hoeche, F. Krauss, M. Schonherr, S. Schumann, F. Siegert, and J. Winter, *Event generation with SHERPA 1.1*, JHEP **02** (2009) 007, [arXiv:0811.4622].

[103] **GEANT4** Collaboration, S. Agostinelli et al., *GEANT4 - A Simulation Toolkit*, Nucl. Instrum. Meth. A **506** (2003) 250–303.

[104] A. D. Sakharov, *Violation of CP Invariance, C asymmetry, and baryon asymmetry of the universe*, Pisma Zh. Eksp. Teor. Fiz. **5** (1967) 32–35.

[105] F. R. Klinkhamer and N. S. Manton, *A Saddle Point Solution in the Weinberg-Salam Theory*, Phys. Rev. D **30** (1984) 2212.

[106] G. W. Anderson and L. J. Hall, *The Electroweak phase transition and baryogenesis*, Phys. Rev. D **45** (1992) 2685–2698.

[107] C. Jarlskog, *PHENOMENOLOGY OF CP VIOLATION*, in XVI International Meeting on Fundamental Physics: CP Non Conservation and B Physics, pp. 0040–73, 10, 1988.

[108] M. B. Gavela, P. Hernandez, J. Orloff, and O. Pene, *Standard model CP violation and baryon asymmetry*, Mod. Phys. Lett. A **9** (1994) 795–810, [hep-ph/9312215].

[109] J. Alonso-González, L. Merlo, and S. Pokorski, *A new bound on CP violation in the τ lepton Yukawa coupling and electroweak baryogenesis*, JHEP **06** (2021) 166, [arXiv:2103.16569].

[110] M. D. Astros, S. Fabian, and F. Goertz, *Minimal Inert Doublet benchmark for dark matter and the baryon asymmetry*, JCAP **02** (2024) 052, [arXiv:2307.01270].

[111] C. Balazs, G. White, and J. Yue, *Effective field theory, electric dipole moments and electroweak baryogenesis*, JHEP **03** (2017) 030, [arXiv:1612.01270].

[112] H. Bahl, E. Fuchs, S. Heinemeyer, J. Katzy, M. Menen, K. Peters, M. Saimpert, and G. Weiglein, *Constraining the CP structure of Higgs-fermion couplings with a global LHC fit, the electron EDM and baryogenesis*, arXiv:2202.11753.

[113] D. C. Howell, Chi-Square Test: Analysis of Contingency Tables, pp. 250–252. Springer Berlin Heidelberg, Berlin, Heidelberg, 2011.

[114] G. J. McLachlan, *On bootstrapping the likelihood ratio test statistic for the number of components in a normal mixture*, Journal of the Royal Statistical Society Series C: Applied Statistics **36** (12, 2018) 318–324, [https://academic.oup.com/jrsssc/article-pdf/36/3/318/48623050/jrsssc_36_3_3

[115] P. Scott, *Pippi — painless parsing, post-processing and plotting of posterior and likelihood samples*, The European Physical Journal Plus **127** (Nov, 2012).

[116] S. J. Huber, M. Pospelov, and A. Ritz, *Electric dipole moment constraints on minimal electroweak baryogenesis*, Phys. Rev. **D75** (2007) 036006, [hep-ph/0610003].

[117] W. Altmannshofer, J. Brod, and M. Schmaltz, *Experimental constraints on the coupling of the Higgs boson to electrons*, arXiv:1503.04830.

[118] J. Brod and E. Stamou, *Electric dipole moment constraints on CP-violating heavy-quark Yukawas at next-to-leading order*, arXiv:1810.12303.

[119] Y. T. Chien, V. Cirigliano, W. Dekens, J. de Vries, and E. Mereghetti, *Direct and indirect constraints on CP-violating Higgs-quark and Higgs-gluon interactions*, JHEP **02** (2016) 011, [arXiv:1510.00725]. [JHEP02,011(2016)].

[120] J. Brod and D. Skodras, *Electric dipole moment constraints on CP-violating light-quark Yukawas*, JHEP **01** (2019) 233, [arXiv:1811.05480].

[121] S. Weinberg, *Larger Higgs Exchange Terms in the Neutron Electric Dipole Moment*, Phys. Rev. Lett. **63** (1989) 2333.

[122] S. M. Barr and A. Zee, *Electric Dipole Moment of the Electron and of the Neutron*, Phys.Rev.Lett. **65** (1990) 21–24.

[123] T. Gribouk and A. Czarnecki, *Electroweak interactions and the muon g-2: Bosonic two-loop effects*, Phys.Rev. **D72** (2005) 053016, [hep-ph/0509205].

[124] K. G. Chetyrkin, M. Misiak, and M. Munz, *Beta functions and anomalous dimensions up to three loops*, Nucl. Phys. **B518** (1998) 473–494, [hep-ph/9711266].

[125] G. Passarino and M. J. G. Veltman, *One Loop Corrections for e+ e- Annihilation Into mu+ mu- in the Weinberg Model*, Nucl. Phys. B **160** (1979) 151–207.

[126] F. V. Tkachov, *A theorem on analytical calculability of 4-loop renormalization group functions*, Phys. Lett. B **100** (1981) 65–68.

[127] K. G. Chetyrkin and F. V. Tkachov, *Integration by parts: The algorithm to calculate β-functions in 4 loops*, Nucl. Phys. B **192** (1981) 159–204.

[128] J. A. M. Vermaseren, *New features of FORM*, math-ph/0010025.

[129] P. Nogueira, *Automatic Feynman graph generation*, J. Comput. Phys. **105** (1993) 279–289.

[130] T. Hahn, *Generating Feynman diagrams and amplitudes with FeynArts 3*, Comput. Phys. Commun. **140** (2001) 418–431, [hep-ph/0012260].

[131] A. Denner, G. Weiglein, and S. Dittmaier, *Application of the background field method to the electroweak standard model*, Nucl. Phys. **B440** (1995) 95–128, [hep-ph/9410338].

[132] A. I. Davydychev and J. Tausk, *Two loop selfenergy diagrams with different masses and the momentum expansion*, Nucl.Phys. **B397** (1993) 123–142.

[133] C. Bobeth, M. Misiak, and J. Urban, *Photonic penguins at two loops and m(t) dependence of BR*$[B \to X(s)\ell^+\ell^-]$, Nucl.Phys. **B574** (2000) 291–330, [hep-ph/9910220].

[134] F. Feruglio, *The Chiral approach to the electroweak interactions*, Int. J. Mod. Phys. A **8** (1993) 4937–4972, [hep-ph/9301281].

[135] G. Buchalla and O. Cata, *Effective Theory of a Dynamically Broken Electroweak Standard Model at NLO*, JHEP **07** (2012) 101, [arXiv:1203.6510].

[136] G. Buchalla, O. Catà, and C. Krause, *Complete Electroweak Chiral Lagrangian with a Light Higgs at NLO*, Nucl. Phys. B **880** (2014) 552–573, [arXiv:1307.5017]. [Erratum: Nucl.Phys.B 913, 475–478 (2016)].

[137] J. Brod, J. M. Cornell, D. Skodras, and E. Stamou, *Global constraints on Yukawa operators in the standard model effective theory*, JHEP **08** (2022) 294, [arXiv:2203.03736].

[138] D. A. Faroughy, J. F. Kamenik, N. Košnik, and A. Smolkovič, *Probing the CP nature of the top quark Yukawa at hadron colliders*, JHEP **02** (2020) 085, [arXiv:1909.00007].

[139] B. Bortolato, J. F. Kamenik, N. Košnik, and A. Smolkovič, *Optimized probes of CP -odd effects in the $t\bar{t}h$ process at hadron colliders*, Nucl. Phys. B **964** (2021) 115328, [arXiv:2006.13110].

[140] H. Bahl, P. Bechtle, S. Heinemeyer, J. Katzy, T. Klingl, K. Peters, M. Saimpert, T. Stefaniak, and G. Weiglein, *Indirect $\mathcal{CP}$ probes of the Higgs-top-quark interaction: current LHC constraints and future opportunities*, JHEP **11** (2020) 127, [arXiv:2007.08542].

[141] W. Altmannshofer, S. Gori, N. Hamer, and H. H. Patel, *Electron EDM in the complex two-Higgs doublet model*, Phys. Rev. D **102** (2020) 115042, [arXiv:2009.01258].

[142] V. Cirigliano, W. Dekens, J. de Vries, and E. Mereghetti, *Is there room for CP violation in the top-Higgs sector?*, Phys. Rev. **D94** (2016), no. 1 016002, [arXiv:1603.03049].

[143] V. Cirigliano, W. Dekens, J. de Vries, and E. Mereghetti, *Constraining the top-Higgs sector of the Standard Model Effective Field Theory*, Phys. Rev. **D94** (2016), no. 3 034031, [arXiv:1605.04311].

[144] J. Kley, T. Theil, E. Venturini, and A. Weiler, *Electric dipole moments at one-loop in the dimension-6 SMEFT*, arXiv:2109.15085.

[145] **GAMBIT** Collaboration, P. Athron et al., *GAMBIT: The Global and Modular Beyond-the-Standard-Model Inference Tool*, Eur. Phys. J. C **77** (2017), no. 11 784, [arXiv:1705.07908]. [Addendum: Eur.Phys.J.C 78, 98 (2018)].

[146] **GAMBIT** Collaboration, C. Balázs et al., *ColliderBit: a GAMBIT module for the calculation of high-energy collider observables and likelihoods*, Eur. Phys. J. C **77** (2017), no. 11 795, [arXiv:1705.07919].

[147] M. Jung and A. Pich, *Electric Dipole Moments in Two-Higgs-Doublet Models*, JHEP **04** (2014) 076, [arXiv:1308.6283].

[148] J. Brod, Z. Polonsky, and E. Stamou, *A precise electron EDM constraint on CP-odd heavy-quark Yukawas*, JHEP **06** (2024) 091, [arXiv:2306.12478].

[149] E. Fuchs, M. Losada, Y. Nir, and Y. Viernik, *CP violation from τ, t and b dimension-6 Yukawa couplings - interplay of baryogenesis, EDM and Higgs physics*, JHEP **05** (2020) 056, [arXiv:2003.00099].

[150] J. Alonso-Gonzalez, A. de Giorgi, L. Merlo, and S. Pokorski, *Searching for BSM physics in Yukawa couplings and flavour symmetries*, JHEP **05** (2022) 041, [arXiv:2109.07490].

[151] G. Degrassi, E. Franco, S. Marchetti, and L. Silvestrini, *QCD corrections to the electric dipole moment of the neutron in the MSSM*, JHEP **0511** (2005) 044, [hep-ph/0510137].

[152] J. Hisano, K. Tsumura, and M. J. S. Yang, *QCD Corrections to Neutron Electric Dipole Moment from Dimension-six Four-Quark Operators*, Phys. Lett. **B713** (2012) 473–480, [arXiv:1205.2212].

[153] G. W. Bennett, B. Bousquet, H. N. Brown, G. Bunce, R. M. Carey, P. Cushman, G. T. Danby, P. T. Debevec, M. Deile, H. Deng, and et al., *Improved limit on the muon electric dipole moment*, Physical Review D **80** (Sep, 2009).

[154] M. Bishof et al., *Improved limit on the ^{225}Ra electric dipole moment*, Phys. Rev. C **94** (2016), no. 2 025501, [arXiv:1606.04931].

[155] F. Allmendinger, I. Engin, W. Heil, S. Karpuk, H.-J. Krause, B. Niederländer, A. Offenhäusser, M. Repetto, U. Schmidt, and S. Zimmer, *Measurement of the permanent electric dipole moment of the $^{129}\mathrm{Xe}$ atom*, Phys. Rev. A **100** (Aug, 2019) 022505.

[156] V. Andreev, D. G. Ang, D. DeMille, J. Doyle, G. Gabrielse, J. Haefner, N. R. Hutzler, Z. Lasner, C. Meisenhelder, B. R. O'Leary, C. D. Panda, A. West, E. P. West, and X. Wu, *Improved limit on the electric dipole moment of the electron*, Nature **562** (10, 2018) 355–360.

[157] J. J. Hudson, D. M. Kara, I. J. Smallman, B. E. Sauer, M. R. Tarbutt, and E. A. Hinds, *Improved measurement of the shape of the electron*, Nature **473** (May, 2011) 493–496.

[158] B. Graner, Y. Chen, E. G. Lindahl, and B. R. Heckel, *Reduced Limit on the Permanent Electric Dipole Moment of Hg199*, Phys. Rev. Lett. **116** (2016), no. 16 161601, [arXiv:1601.04339]. [Erratum: Phys. Rev. Lett.119,no.11,119901(2017)].

[159] **CMS** Collaboration, A. Tumasyan et al., *Analysis of the CP structure of the Yukawa coupling between the Higgs boson and τ leptons in proton-proton collisions at $\sqrt{s}$ = 13 TeV*, arXiv:2110.04836.

[160] M. Galassi, J. Davies, J. Theiler, B. Gough, G. Jungman, M. Booth, and F. Rossi, GNU Scientific Library Reference Manual. GNU Project, 3rd ed., 2009. ISBN 0954612078.

[161] G. Guennebaud, B. Jacob, et al., Eigen: A C++ Template Library for Linear Algebra. Eigen, 2023. Version 3.4.0, retrieved January 2025.

[162] T. E. Gonzalo, *GAMBIT: The Global and Modular BSM Inference Tool*, PoS **TOOLS2020** (2021) 041, [arXiv:2105.03165].

[163] P. Bechtle, S. Heinemeyer, T. Klingl, T. Stefaniak, G. Weiglein, and J. Wittbrodt, *HiggsSignals-2: Probing new physics with precision Higgs measurements in the LHC 13 TeV era*, Eur. Phys. J. C **81** (2021), no. 2 145, [arXiv:2012.09197].

[164] P. Bechtle, D. Dercks, S. Heinemeyer, T. Klingl, T. Stefaniak, G. Weiglein, and J. Wittbrodt, *HiggsBounds-5: Testing Higgs Sectors in the LHC 13 TeV Era*, Eur. Phys. J. C **80** (2020), no. 12 1211, [arXiv:2006.06007].

[165] **ATLAS, CMS** Collaboration, G. Aad et al., *Measurements of the Higgs boson production and decay rates and constraints on its couplings from a combined ATLAS and CMS analysis of the LHC pp collision data at $\sqrt{s} = 7$ and 8 TeV*, JHEP **08** (2016) 045, [arXiv:1606.02266].

[166] **LHC Higgs Cross Section Working Group** Collaboration, D. de Florian et al., *Handbook of LHC Higgs Cross Sections: 4. Deciphering the Nature of the Higgs Sector*, arXiv:1610.07922.

[167] **ATLAS** Collaboration, G. Aad et al., *A search for the dimuon decay of the Standard Model Higgs boson with the ATLAS detector*, Phys. Lett. B **812** (2021) 135980, [arXiv:2007.07830].

[168] **CMS** Collaboration, A. M. Sirunyan et al., *Evidence for Higgs boson decay to a pair of muons*, JHEP **01** (2021) 148, [arXiv:2009.04363].

[169] **ATLAS** Collaboration, M. Aaboud et al., *Search for Higgs bosons produced via vector-boson fusion and decaying into bottom quark pairs in $\sqrt{s} = 13$ TeV pp collisions with the ATLAS detector*, Phys. Rev. D **98** (2018), no. 5 052003, [arXiv:1807.08639].

[170] **ATLAS** Collaboration, M. Aaboud et al., *Search for the standard model Higgs boson produced in association with top quarks and decaying into a $b\bar{b}$ pair in pp collisions at $\sqrt{s}$ = 13 TeV with the ATLAS detector*, Phys. Rev. D **97** (2018), no. 7 072016, [arXiv:1712.08895].

[171] **ATLAS** Collaboration, M. Aaboud et al., *Measurements of gluon-gluon fusion and vector-boson fusion Higgs boson production cross-sections in the $H \to WW^* \to e\nu\mu\nu$ decay channel in pp collisions at $\sqrt{s} = 13$ TeV with the ATLAS detector*, Phys. Lett. B **789** (2019) 508–529, [arXiv:1808.09054].

[172] **ATLAS** Collaboration, M. Aaboud et al., *Cross-section measurements of the Higgs boson decaying into a pair of τ-leptons in proton-proton collisions at $\sqrt{s} = 13$ TeV with the ATLAS detector*, Phys. Rev. D **99** (2019) 072001, [arXiv:1811.08856].

[173] **ATLAS Collaboration** Collaboration, *Analysis of $t\bar{t}H$ and $t\bar{t}W$ production in multilepton final states with the ATLAS detector*, tech. rep., CERN, Geneva, Oct, 2019. All figures including auxiliary figures are available at https://atlas.web.cern.ch/Atlas/GROUPS/PHYSICS/CONFNOTES/ATLAS-CONF-2019-045.

[174] **CMS** Collaboration, A. M. Sirunyan et al., *Evidence for the Higgs boson decay to a bottom quark–antiquark pair*, Phys. Lett. B **780** (2018) 501–532, [arXiv:1709.07497].

[175] **CMS** Collaboration, A. M. Sirunyan et al., *Inclusive search for a highly boosted Higgs boson decaying to a bottom quark-antiquark pair*, Phys. Rev. Lett. **120** (2018), no. 7 071802, [arXiv:1709.05543].

[176] **CMS** Collaboration, A. M. Sirunyan et al., *Search for $\mathrm{t\bar{t}H}$ production in the $\mathrm{H} \to \mathrm{b\bar{b}}$ decay channel with leptonic $\mathrm{t\bar{t}}$ decays in proton-proton collisions at $\sqrt{s} = 13$ TeV*, JHEP **03** (2019) 026, [arXiv:1804.03682].

[177] **ATLAS** Collaboration, G. Aad et al., *Measurement of the production cross section for a Higgs boson in association with a vector boson in the $H \to WW^* \to \ell\nu\ell\nu$ channel in pp collisions at $\sqrt{s}$ = 13 TeV with the ATLAS detector*, Phys. Lett. B **798** (2019) 134949, [arXiv:1903.10052].

[178] **ATLAS** Collaboration, G. Aad et al., *Measurements of WH and ZH production in the $H \to b\bar{b}$ decay channel in pp collisions at 13 TeV with the ATLAS detector*, Eur. Phys. J. C **81** (2021), no. 2 178, [arXiv:2007.02873].

[179] **CMS** Collaboration, A. M. Sirunyan et al., *Search for the Higgs boson decaying to two muons in proton-proton collisions at $\sqrt{s} =$ 13 TeV*, Phys. Rev. Lett. **122** (2019), no. 2 021801, [arXiv:1807.06325].

[180] **CMS** Collaboration, A. M. Sirunyan et al., *Evidence for associated production of a Higgs boson with a top quark pair in final states with electrons, muons, and hadronically decaying τ leptons at $\sqrt{s} =$ 13 TeV*, JHEP **08** (2018) 066, [arXiv:1803.05485].

[181] **CMS Collaboration** Collaboration, *Measurement of* $\mathrm{t\bar{t}H}$ *production in the* $\mathrm{H} \to \mathrm{b\bar{b}}$ *decay channel in* $41.5\,\mathrm{fb}^{-1}$ *of proton-proton collision data at* $\sqrt{s} = 13\,\mathrm{TeV}$, tech. rep., CERN, Geneva, 2019.

[182] **CMS Collaboration** Collaboration, *Measurement of the associated production of a Higgs boson with a top quark pair in final states with electrons, muons and hadronically decaying τ leptons in data recorded in 2017 at* $\sqrt{s} = 13$ TeV, tech. rep., CERN, Geneva, 2018.

[183] **CMS Collaboration** Collaboration, *Measurements of properties of the Higgs boson in the four-lepton final state in proton-proton collisions at* $\sqrt{s} = 13$ TeV, tech. rep., CERN, Geneva, 2019.

[184] **CMS Collaboration** Collaboration, *Measurements of Higgs boson production via gluon fusion and vector boson fusion in the diphoton decay channel at* $\sqrt{s} = 13$ *TeV*, tech. rep., CERN, Geneva, 2019.

[185] **CMS Collaboration** Collaboration, *Measurement of Higgs boson production and decay to the $\tau\tau$ final state*, tech. rep., CERN, Geneva, 2019.

[186] **ATLAS Collaboration** Collaboration, *Measurements and interpretations of Higgs-boson fiducial cross sections in the diphoton decay channel using 139 fb^{-1} of pp collision data at $\sqrt{s}$ = 13 TeV with the ATLAS detector*, tech. rep., CERN, Geneva, Jul, 2019. All figures including auxiliary figures are available at https://atlas.web.cern.ch/Atlas/GROUPS/PHYSICS/CONFNOTES/ATLAS-CONF-2019-029.

[187] **ATLAS** Collaboration, G. Aad et al., *Higgs boson production cross-section measurements and their EFT interpretation in the 4ℓ decay channel at $\sqrt{s}$ =13 TeV with the ATLAS detector*, Eur. Phys. J. C **80** (2020), no. 10 957, [arXiv:2004.03447]. [Erratum: Eur.Phys.J.C 81, 29 (2021), Erratum: Eur.Phys.J.C 81, 398 (2021)].

[188] **CMS** Collaboration, A. M. Sirunyan et al., *Measurement of the inclusive and differential Higgs boson production cross sections in the leptonic WW decay mode at $\sqrt{s} = 13$ TeV*, JHEP **03** (2021) 003, [arXiv:2007.01984].

[189] **GAMBIT** Collaboration, G. D. Martinez, J. McKay, B. Farmer, P. Scott, E. Roebber, A. Putze, and J. Conrad, *Comparison of statistical sampling methods with ScannerBit, the GAMBIT scanning module*, Eur. Phys. J. C **77** (2017), no. 11 761, [arXiv:1705.07959].

[190] MPI Forum, MPI: The Message Passing Interface Standard. MPI Forum, version 4.0 ed., 2021. A standard for parallel programming and multiprocessing.

[191] The HDF Group, HDF5: Hierarchical Data Format, Version 1.12.2. The HDF Group, 2023. A versatile data model for managing and storing data.

[192] **Particle Data Group** Collaboration, P. Zyla et al., *Review of Particle Physics*, PTEP **2020** (2020), no. 8 083C01.

[193] E. Fuchs, M. Losada, Y. Nir, and Y. Viernik, *Implications of the Upper Bound on $h \to \mu^+\mu^-$ on the Baryon Asymmetry of the Universe*, Phys. Rev. Lett. **124** (2020), no. 18 181801, [arXiv:1911.08495].

[194] Y. Soreq, H. X. Zhu, and J. Zupan, *Light quark Yukawa couplings from Higgs kinematics*, JHEP **12** (2016) 045, [arXiv:1606.09621].

[195] T. Bhattacharya, V. Cirigliano, R. Gupta, E. Mereghetti, and B. Yoon, *Dimension-5 CP-odd operators: QCD mixing and renormalization*, Phys. Rev. **D92** (2015), no. 11 114026, [arXiv:1502.07325].

[196] T. Bhattacharya, V. Cirigliano, R. Gupta, and B. Yoon, *Quark Chromoelectric Dipole Moment Contribution to the Neutron Electric Dipole Moment*, PoS **LATTICE2016** (2016) 225, [arXiv:1612.08438].

[197] B. Yoon, T. Bhattacharya, V. Cirigliano, and R. Gupta, *Neutron Electric Dipole Moments with Clover Fermions*, PoS **LATTICE2019** (2020) 243, [arXiv:2003.05390].

[198] R. Harnik, A. Martin, T. Okui, R. Primulando, and F. Yu, *Measuring CP violation in $h \to \tau^+\tau^-$ at colliders*, Phys. Rev. **D88** (2013), no. 7 076009, [arXiv:1308.1094].

[199] F. Demartin, F. Maltoni, K. Mawatari, B. Page, and M. Zaro, *Higgs characterisation at NLO in QCD: CP properties of the top-quark Yukawa interaction*, Eur. Phys. J. C **74** (2014), no. 9 3065, [arXiv:1407.5089].

[200] M. R. Buckley and D. Goncalves, *Boosting the Direct CP Measurement of the Higgs-Top Coupling*, Phys. Rev. Lett. **116** (2016), no. 9 091801, [arXiv:1507.07926].

[201] A. V. Gritsan, R. Röntsch, M. Schulze, and M. Xiao, *Constraining anomalous Higgs boson couplings to the heavy flavor fermions using matrix element techniques*, Phys. Rev. D **94** (2016), no. 5 055023, [arXiv:1606.03107].

[202] D. Azevedo, A. Onofre, F. Filthaut, and R. Gonçalo, *CP tests of Higgs couplings in $t\bar{t}h$ semileptonic events at the LHC*, Phys. Rev. D **98** (2018), no. 3 033004, [arXiv:1711.05292].

[203] C. Grojean, A. Paul, and Z. Qian, *Resurrecting $b\bar{b}h$ with kinematic shapes*, JHEP **04** (2021) 139, [arXiv:2011.13945].

[204] T. Martini, R.-Q. Pan, M. Schulze, and M. Xiao, *Probing the CP structure of the top quark Yukawa coupling: Loop sensitivity versus on-shell sensitivity*, Phys. Rev. D **104** (2021), no. 5 055045, [arXiv:2104.04277].

[205] Q. Bonnefoy, E. Gendy, C. Grojean, and J. T. Ruderman, *Beyond Jarlskog: 699 invariants for CP violation in SMEFT*, arXiv:2112.03889.